Ivano Giuntoni

Tunable integrated module for the optical dispersion compensation based on Bragg gratings in silicon

Technische Universität Berlin

Ivano Giuntoni

Tunable integrated module for the optical dispersion compensation based on Bragg gratings in silicon

Ivano Giuntoni

Tunable integrated module for the optical dispersion compensation based on Bragg gratings in silicon

Universitätsverlag der TU Berlin

Bibliografische Information der Deutschen Nationalbibliothek
Die Deutsche Nationalbibliothek verzeichnet diese Publikation in der Deutschen Nationalbibliografie; detaillierte bibliografische Daten sind im Internet über http://dnb.dnb.de/ abrufbar.

Universitätsverlag der TU Berlin 2013
http://www.univerlag.tu-berlin.de
Fasanenstr. 88 (im VOLKSWAGEN-Haus), 10623 Berlin
Tel.: +49 (0)30 314 76131 / Fax: -76133
E-Mail: publikationen@ub.tu-berlin.de

Zugl.: Berlin, Technische Universität, Diss., 2013
1. Gutachter: Prof. Dr. Klaus Petermann
2. Gutachter: Prof. Dr. Ernst Brinkmeyer
Die Arbeit wurde am 26. April 2013 an der Fakultät IV unter Vorsitz von Prof. Dr. Bernd Tillack erfolgreich verteidigt.

Das Manuskript ist urheberrechtlich geschützt.
Druck: endformat GmbH, Berlin
Satz/Layout: Ivano Giuntoni

Zugleich online veröffentlicht auf dem Digitalen Repositorium der Technischen Universität Berlin:
URL http://opus4.kobv.de/opus4-tuberlin/frontdoor/index/index/docId/3823
URN urn:nbn:de:kobv:83-opus4-38237
[http://nbn-resolving.de/urn:nbn:de:kobv:83-opus4-38237]

ISBN 978-3-7983-2576-0 (print)
ISBN 978-3-7983-2577-7 (online)

Acknowledgments

Here I would like to thank and acknowledge all the people, who contributed to this work.

First of all I have to thank Prof. Klaus Petermann for giving me the opportunity to accomplish my PhD in his research group in the institute "Hochfrequenztechnik/Photonics" at the Technische Universität Berlin. His continuous support and technical advices have been very precious.

Dr. Jürgen Bruns deserves as well my gratitude for his constant project supervision and coordination of the technology department of the institute.

I would like to thank also Prof. Ernst Brinkmeyer, not only for accepting to be a referee for this thesis, but also and mostly for the direction of the DFG research group "Active and tunable micro-optic systems based on Silicon-on-Insulator". The opportunity to take part to a project within this frame allowed me to interact with a high numbers of scientist working in the same field and broaden my knowledge spectrum enormously. In particular I would like to thank Dr. Hagen Renner and Dr. Michael Krause from the Technische Universität Hamburg-Harburg for their fundamental help in the theoretical understanding of the principles of Bragg gratings and their numerical analysis.

I would also like to acknowledge Prof. Bernd Tillack and Dr. Lars Zimmermann from IHP Microelectronics GmbH for the organization of the Joint Lab together with the Technische Universität Berlin, which permitted the realization of the designed devices. In particular my gratitude goes to David Stolarek, who took care of the development of the required fabrication processes.

The precious work of Dr. Ralf Steingrüber from the Fraunhofer Institute for Telecommunications – Heinrich-Hertz-Institut has been irreplaceable for the realization of grating structures with electron-beam lithography. The members of the technology department, Evelin Brose, Beatrice Kranzusch, Michael Gruse and Marlies Mahnkopf, deserve a special thank, since they permitted the fabrication and post-processing of the designed components and contributed with their deep experience and cooperativeness to the positive results presented in this thesis.

Here I would like also to thank Dimitar Kroushkov for his precious work in the system emulations of the integrated dispersion compensator.

A special acknowledgment is addressed to my project colleague Andrzej Gajda, who worked with me within the DFG research group at the Technische Universität Berlin and has contributed with many ideas and suggestions. His work for the implementation of a measurement setup for the characterization of integrated optical components has been extremely

precious, as well as the many discussions we had the opportunity to have, not always about technical topics.

I would like to thank also all other colleagues of the institute for their helpfulness, for the friendly work atmosphere and the pleasant time we spent together.

Last but of course not least, I would like to sincerely thank my family and all my friends who supported me during these years, encouraging me to pursue my goals.

Berlin, July 2013

Contents

Introduction **1**

1 Dispersion compensation in optical transmission systems **5**
1.1 Chromatic dispersion in optical transmission systems 5
1.2 Residual dispersion 6
1.3 Residual dispersion compensation 10
1.3.1 Chirped fiber Bragg gratings 11
1.3.2 Serial optical filters 12
1.3.3 Parallel optical filters 15
1.3.4 Serial-parallel optical filters 18
1.3.5 Comparison 19

2 Uniform Bragg gratings on SOI rib waveguides **21**
2.1 Modelling of Bragg gratings 21
2.1.1 Coupled mode theory (CMT) 21
2.1.2 Numerical analysis of Bragg Gratings 27
2.2 Design of Bragg gratings on SOI rib waveguides 39
2.2.1 Simulation procedure 39
2.2.2 Waveguide design 42
2.2.3 Grating design 46
2.3 Fabrication 48
2.4 Characterization 53
2.4.1 Measurement setup 53
2.4.2 Experimental results 55

3 Integrated dispersion compensator **61**
3.1 Chirped gratings for dispersion compensation 61
3.2 Integrated drop-filter for dispersion compensation 62
3.3 Grating design 65
3.3.1 Chirp implementation 65
3.3.2 Taper design 68
3.4 Reduction of the group delay ripple 70
3.4.1 Group delay ripple 70
3.4.2 Grating apodization 76
3.5 Drop filter design 80
3.5.1 MMI couplers 80
3.5.2 Waveguide coupling 81
3.6 Characterization 83
3.6.1 Dispersion measurement 83
3.6.2 Experimental results 83

3.7 System emulation 86

4 Dispersion tuning **91**
4.1 Thermal tuning of Bragg grating 91
4.2 Thermal tuning of the dispersion 92
4.3 Heater design 96
4.4 Characterization 102

5 Conclusion **113**

Bibliography **117**

List of figures **129**

List of Publications **137**

Introduction

The requested data amount to be carried in optical communication networks has been increasing exponentially in the last decade, mostly due to the demand and growth of new services on the Internet and the general extension of broadband wireless and wire line access network. A growing number of users and data brought to an upgrade in DWDM networks from a transmission of 10 Gb/s per channel to more spectrally-efficient 40 Gb/s or 100 Gb/s per channel. Furthermore 400 Gb/s and 1 Tb/s Ethernet should be standardized in the near future [1]. To support beyond 400 Gb/s serial transmission, a better modulation format would be needed to get closer to the channel capacity [2, 3].

However fiber impairments challenge the achievement of these aims, like non-linearities and dispersion. This last one, interacting with the non-linearities, constitutes a strong limitation for the high speed transmission on long distances and several efforts have been spent to mitigate its effect. In absence of a dispersion compensation, the transmitted pulses broaden in time because of different propagation velocities of different wavelengths in fibers. The consequence is the impossibility to properly detect the pulse sequence at the receiver and reconstruct the transmitted information.

Different approaches have been proposed to compensate the fiber dispersion, either optically or electronically [4, 5]. In the former case dispersion compensating fibers or optical filters are used, in the latter one digital circuits for signal processing implementing algorithms able to reconstruct the signal. Optical dispersion compensation systems have the advantage not to require a signal conversion and can be implemented in-line. However they are intrinsically analog and can be affected by non-linearities. Electronic compensators on the other hand require a conversion of the signal, with a consequent speed limitation. They permit however a high flexibility, since they can be easily programmed. While optical statical compensation devices are used in line within the transmission span, electronic systems are typically implemented at the receiver stations to compensate an eventual residual dispersion.

One of the main drawbacks of electronic dispersion compensation, together with the optical-to-electrical signal conversion, is the high power consumption. This can reach values between 14 W and 44 W according to the used algorithm to compensate a 100 GbE channel at 28 Gbaud [6]. Considering that nowadays the energy consumed by optical telecommunication networks is already 1% of the total consumed power worldwide [7,8], it is evident that the future growing data traffic will make this problematic more and more critical. The realization of all-optical signal processing devices for dispersion compensation with low power consumption would

permit to achieve a faster operation without the need of signal conversion, reducing the limitations for the growing networks.

Different optical devices for dispersion compensation have been proposed in the past, however they have the disadvantage of being constituted of discrete components. The realization of integrated devices for the dispersion compensation is mandatory for the realization of compact receiver units. Silicon photonics offers an almost perfect basis for this purpose [9, 10]. The achievement of integrated optical devices on silicon can be considered nowadays state of the art, with a large number of proven examples of integrated devices. Silicon is an ideal material for optical purposes in the range of wavelengths used for optical communications, since it is almost transparent, exhibits low absorption [11] and a high refractive index ($\sim$3.5). This permits to realize low loss waveguides with dimensions in the range of the wavelength itself. Furthermore silicon is available in large quantities at low prices, and is the basis material in microelectronics. It means that the established fabrication know-how and facilities from the electronics can be applied for the realization of optical devices as well, with a consequent cost reduction. In the next future the sharing of the same basis material should permit also a combination of electronic and optical devices together for the implementation of more complex systems [12, 13].

Different optical components have been demonstrated on silicon, like arrayed waveguide gratings (AWGs), couplers, modulators [14], wavelength converters [15]. The hybrid integration of active devices like laser sources or detectors made of direct semiconductors on a silicon chip are deeply investigated, as well as the possibility to achieve light sources directly with silicon exploiting non-linear effects [16, 17].

The realization of an integrated tunable compensator for the residual dispersion and its combination with demodulators and detectors would permit to obtain compact and low cost receiver modules on a silicon chip. Within this work the design and the fabrication of a dispersion compensating device based on Bragg gratings on silicon waveguides is demonstrated.

In the first chapter the definition of residual dispersion is given, and different approaches for its compensation with bulky and integrated devices are described. The second chapter is dedicated to the analysis of uniform Bragg gratings in rib waveguides, their dimensioning and implementation on silicon. The numerical model for the simulations is deeply discussed, and the fabrication processes are presented. Based on the results from the characterization of uniform gratings, the evolution to chirped gratings for dispersion compensation is the topic of the third chapter. Here

not only a design of the chirp is carried on, but also an optimization of the grating shape for a better performance. Furthermore the combination in a more complex structure for in-line compensation is demonstrated. In the last chapter the tuning of the grating dispersion with temperature is shown. The tuning principle and the practical implementation are described, and the final characterization of the tuned dispersion compensator is presented.

1

Dispersion compensation in optical transmission systems

1.1 Chromatic dispersion in optical transmission systems

The interaction of an electromagnetic wave with an optical medium is in general wavelength dependent, since the refractive index is not constant for every optical frequency. The material exhibits characteristic resonance frequencies at which electromagnetic radiation is absorbed through electronic and lattice/ionic oscillations. Far from the material resonances, the refractive index n is approximated by the Sellmeier equation [18]:

$$n^2(\omega) = 1 + \sum_{j=1}^{m} \frac{B_j \omega_j^2}{\omega_j^2 - \omega^2} \tag{1.1}$$

where ω_j is the resonance frequency and B_j is the resonance strength. This wavelength dependence of the refractive index is critical for the transmission of optical pulses in waveguides, since different spectral components propagate with different velocities, resulting in a pulse width distortion. This phenomenon is denoted as *chromatic dispersion* and is one of the most critical limitations for long distance optical communication systems. At a certain dispersion magnitude, the pulses of the transmitted data stream broaden in such a way until they overlap with each other and cannot be detected without error, leading to intersymbol interference (ISI).

It is possible to evaluate more precisely the effect of the dispersion expanding the mode propagation constant β in a Taylor series about the frequency ω_0, the center frequency of the optical pulse:

$$\beta(\omega) = n(\omega)\frac{\omega}{c} = \beta_0 + \beta_1(\omega - \omega_0) + \frac{1}{2}\beta_2(\omega - \omega_0)^2 + ..., \tag{1.2}$$

where

$$\beta_m = \left.\frac{\partial^m \beta}{\partial \omega^m}\right|_{\omega=\omega_0} \qquad m = 0, 1, 2... \tag{1.3}$$

If the terms $\beta_m \neq 0$ a frequency dependence of the propagation constant occurs.

The inverse of the first oder derivative of β is the group velocity and indicates how fast the spectral components propagate from each other:

$$v_g = \frac{1}{\beta_1} = \frac{c}{n_g} = \frac{c}{n + \omega \frac{\partial n}{\partial \omega}} \tag{1.4}$$

where c is the vacuum speed of light and

$$n_g = n + \omega \frac{dn}{d\omega} \tag{1.5}$$

is the material group index. From the expression of the group velocity the group delay is obtained:

$$\tau = \frac{L}{v_g} = L\beta_1 = \frac{\partial(L\beta)}{\partial \omega} = \frac{\partial \phi}{\partial \omega}. \tag{1.6}$$

It is useful to express the group delay as function of the wavelength:

$$\tau = \frac{\partial \phi}{\partial \omega} = \frac{\partial \phi}{\partial \lambda} \cdot \frac{\partial \lambda}{\partial \omega} = -\frac{\lambda_0^2}{2\pi c} \cdot \frac{\partial \phi}{\partial \lambda} \tag{1.7}$$

The derivative of the group delay over the wavelength is defined chromatic dispersion:

$$D = \frac{\partial \tau}{\partial \lambda} = -\frac{\lambda_0^2}{2\pi c} \cdot \frac{\partial^2 \phi}{\partial \lambda^2}. \tag{1.8}$$

This quantity is expressed in [ps/nm] and describes how large is the relative delay between spectral components per unit wavelength due to the frequency dependence of the refractive index. The dispersion coefficient $D' = D/L$ is also used to describe the dispersion properties of fibers, and is expressed in [ps/nm·km].

1.2 Residual dispersion

On Fig. 1.1(a) the refractive index and the group index of pure silica as function of the wavelength are represented. It can be observed that the the material refractive index is monotonically decreasing for larger wavelengths; in particular it has a value of about 1.46 in the visible region and

decreases by 1% in the wavelength region near 1550 nm. On the other hand the group index exhibits a minimum which leads to a zero dispersion at $\lambda = 1273$ nm (blue dashed curve on Fig. 1.1(b)).

So far only the effect of the pure material has been considered. In a fiber the light guiding itself contribute to the chromatic dispersion. Each guided mode is identified by its propagation constant β_m. From it, the effective refractive index

$$n_{eff} = \beta / k_0 \tag{1.9}$$

is defined, where $k_0 = 2\pi/\lambda$ is the free-space wave number. It has the physical meaning that each mode experiences a different refractive index, whose value lies in the range $n_{cladding} < n_{eff} < n_{core}$ [18]. At larger wavelengths the fundamental mode field of the fiber LP_{01} becomes larger and propagates more into the cladding, experiencing a lower effective refractive index. This effect is defined as *waveguide dispersion* and is indicated on Fig. 1.1(b) with the red dotted line. In a SMF-28 step fiber the chromatic dispersion is the sum of two terms:

$$D_{tot}(\lambda) = D_M(\lambda) + D_{wg}(\lambda) \tag{1.10}$$

where D_M is the material dispersion discussed in the previous section. At a wavelength of $\lambda = 1312$ nm the overall dispersion appears to be zero, hence a data transmission at this wavelength is affected by a minimal dispersion induced intersymbol interference.

In an optical transmission system the signal has to be regenerated after a certain propagation distance to overcome the accumulation of optical noise, linear and nonlinear distortions [19]. This is achieved employing erbium-doped fiber amplifiers (EDFAs) [20, 21], which permit to have a regenerator spacing of several thousands of kilometers, reducing network costs and avoiding a digital electronic regeneration. The disadvantage is given by the fact that the system must operate in the gain window of the amplifiers, approximately 1553–1556 nm. At this wavelengths the dispersion coefficient of a standard single mode fiber is not zero, but has a value in the range of 15–18 ps/nm·km, making the employment of dispersion compensating systems necessary.

The compensating system has to be chosen and designed in order to exhibit a chromatic dispersion D_{comp} corresponding to the dispersion of a transmission span of length L:

$$L \cdot D'_{tr}(\lambda) + D_{comp}(\lambda) = D_{\text{res}} = 0 \tag{1.11}$$

where D'_{tr} is the dispersion coefficient of the transmission span. The difference between the accumulated dispersion in the transmission system and

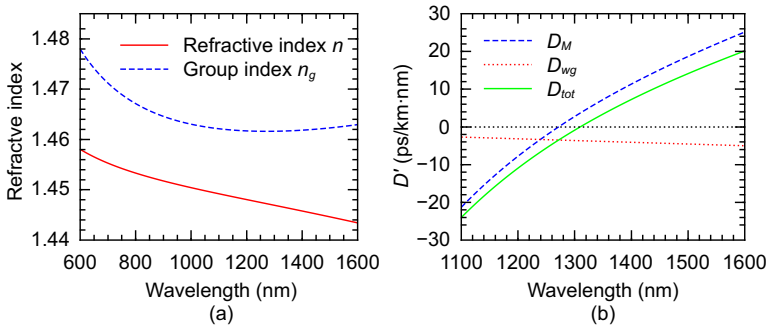

Figure 1.1: (a) Refractive index and group index as function of the wavelength for fused silica. (b) Chromatic dispersion coefficients of a SMF-28 step fiber.

the dispersion of the compensating module is referred as *residual dispersion* and should be ideally zero.

Different attempts have been done to reduce the effect of chromatic dispersion in optical fibers. As it can be observed on Fig. 1.1(b) the effect of the waveguide dispersion is to shift the zero dispersion point to longer wavelengths. It is intuitive that increasing the waveguide dispersion, this zero dispersion point can be shifted until λ = 1550 nm, obtaining a dispersion free fiber. This can be achieved modifying the waveguide structure with smaller core radii, obtaining *dispersion-shifted fibers* (DSF). However in a dispersion free transmission system the phase matching condition of four wave mixing (FWM) is ensured along the fiber, and results in the generation of new wavelengths which cause nonlinear channel crosstalk in WDM systems [22, 23]. To overcome this issue, a compromise has been found with the non-zero dispersion-shifted fibers (NZ-DSF), where the zero dispersion point is placed at slightly shorter wavelengths than the used ones. The chromatic dispersion within the transmission band is therefore strongly reduced to values about 4-8 ps/nm·km at λ = 1550 nm, reducing the requirements for the compensating system. Such fibers are employed nowadays in new transmission systems for high data rates larger than 40 Gbit/s per channel [24].

The actual compensation is mostly carried out employing *dispersion compensating fibers* (DCF), which are designed to exhibit a negative dispersion with values about -45 – -300 ps/nm·km [25, 26], but also larger attenuation about 0.3–1 dB/km compared to standard fibers and larger

bending losses. Properly choosing the length of these fibers it is ideally possible to compensate the dispersion of a given transmission link.

The dispersion compensation achieved with the employment of DCFs is only theoretically perfect, since it is based on the assumption that the dispersion of the transmission link is fixed. From this value, the DCF length is determined. However the chromatic dispersion in a fiber is not a constant value, but changes in time under the influence of several factors, primarily the temperature. It has been demonstrated that the coefficients of the Sellmeier equation (1.1) are temperature dependent [27]. Consequently, the fiber dispersion varies according to the environment temperature about -2.5×10^{-3} ps/nm·km·K for NZ-DSF and -3.8×10^{-3} ps/nm·km·K for large core fibers [28, 29].

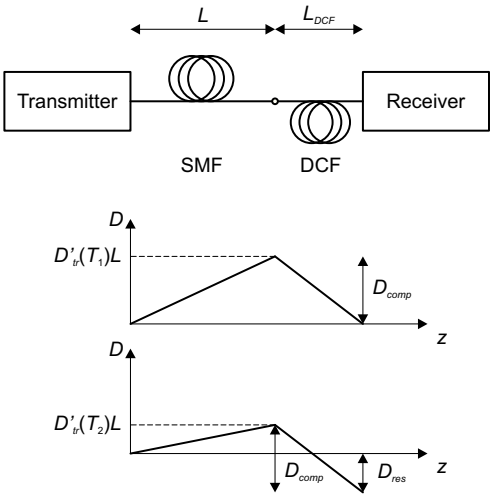

Figure 1.2: Scheme of a transmission link with a standard fiber with length L and a dispersion compensating fiber with length L_{DCF}. The dispersion profile is considered for two different temperatures T_1 and T_2.

Measurements showed that the soil temperature at a depth of 60 – 120 cm where long haul fibers cables are buried exhibits seasonal variations in the order of 20 K over a year [30]. This temperature variation causes a dispersion deviation of 375 ps/nm for NZ-DSF and 570 ps/nm for large core fibers in a 7500 km long terrestrial haul route. Since the compensation with DCFs is designed for a certain dispersion value, over the

Format	Dispersion limit (ps/nm)
non-return-to-zero (NRZ)	65
return-to-zero (RZ)	50
carrier-suppressed RZ	48
differential phase shift keying (DPSK)	56
RZ-DPSK	45
phase-shaped binary transmission (PSBT)	160

Table 1.1: Dispersion limit for different modulation formats to achieve a penalty of 1 dB at a data rate of 43 Gbit/s [31].

year the residual dispersion varies, degrading the signal quality. In Fig. 1.2 a transmission link with a standard fiber and a DCF is depicted. The system is designed for an operation at a temperature T_1. In this situation the dispersion of the DCF equals the dispersion accumulated along the transmission fiber and the regenerated signal can be properly detected at the receiver:

$$D'_{tr}(T_1)L - D'_{DCF}L_{DCF} = 0. \tag{1.12}$$

At a different temperature T_2, however, the dispersion coefficient of the transmission fiber exhibits a different value, with a consequent different accumulated dispersion after a propagation length L. Since the length of the DCF remains unchanged, a residual dispersion different than zero occurs at the receiver.

Only a certain level of residual dispersion is tolerated at the receiver for an error free detection. According to the used modulation format, a specific value of residual dispersion limit has been determined where the penalty variation remains within 1 dB from the optimum at a data rate of 43 Gbit/s. The values of the dispersion limits are indicated on Table 1.1 [31]. It can be observed that for every considered modulation format the maximal tolerated dispersion is much lower than the actual variations due to temperature changes. A further adaptive dispersion compensation has to be employed at the receiver side to improve the signal quality and permit a good error-free detection.

1.3 Residual dispersion compensation

Different solutions have been analyzed in the recent past for the realization of systems able to compensate the residual dispersion. Different approaches have been proposed, either based on bulky components or integrated. The latter ones give the opportunity of a direct combination with receiver modules. In general a device for the dispersion compensation is a

filter which should ideally exhibit a frequency response with a flat amplitude and a quadratic phase over the frequency range of interest. The filter response can be periodic and hence allow a multichannel compensation of the residual dispersion. In this section different concepts for the realization of such compensators are described, according to their basic principle.

1.3.1 Chirped fiber Bragg gratings

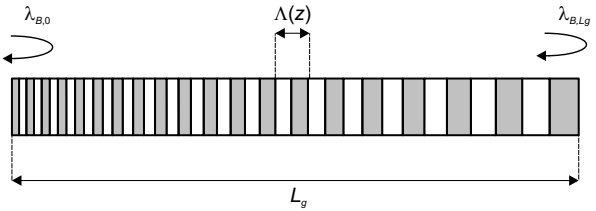

Figure 1.3: Scheme of a chirped Bragg grating of length L, with a linearly varying period $\Lambda(z)$.

Dispersion compensators based on fiber Bragg gratings have been proposed and demonstrated since the late 80s [32]. The principle of Bragg gratings will not be discussed in detail in this section, since it is topic of the next chapters, but only a basic explanation will be provided. In a Bragg grating the periodic modulation of the core refractive index produces a selective reflection over a narrow bandwidth centered at the Bragg wavelength, proportional to the modulation period Λ. Chirping the grating, the period can be varied along the grating length in order to reflect different wavelengths at different positions (see Fig. 1.3); in this way the different spectral components of the input signal experience a different propagation path length, with a consequent delay. The maximum achievable group delay depends hence on the grating length L_g:

$$\Delta\tau_{max} = \frac{2n_g L_g}{c} \tag{1.13}$$

where n_g is the group index of the fiber core. If $\lambda_{B,0}$ and λ_{B,L_g} are the wavelengths reflected at the beginning and at the end of the grating respectively, the maximum dispersion is, according to Eq. 1.8:

$$D_{max} = \frac{2n_g L_g}{c\left(\lambda_{B,L_g} - \lambda_{B,0}\right)}. \tag{1.14}$$

The realization of chirped fiber Bragg gratings using phase masks have been demonstrated [33–35], showing that a dispersion of 6000 ps/nm with a 10 cm long grating can be achieved. Furthermore different tuning principles have been proposed, which have the aim to modify the chirp function $\Lambda(z)$ and hence the bandwidth. This has been demonstrated bending the grating with strain [36] or thermally, depositing thin film heaters on the fiber and exploiting the thermo-optical effect [37,38].

1.3.2 Serial optical filters

Finite impulse response (FIR) and infinite impulse response (IIR) filters have been employed for the realization of integrated dispersion compensators. Properly defining the transfer function of the filter, the desired chromatic dispersion can be compensated.

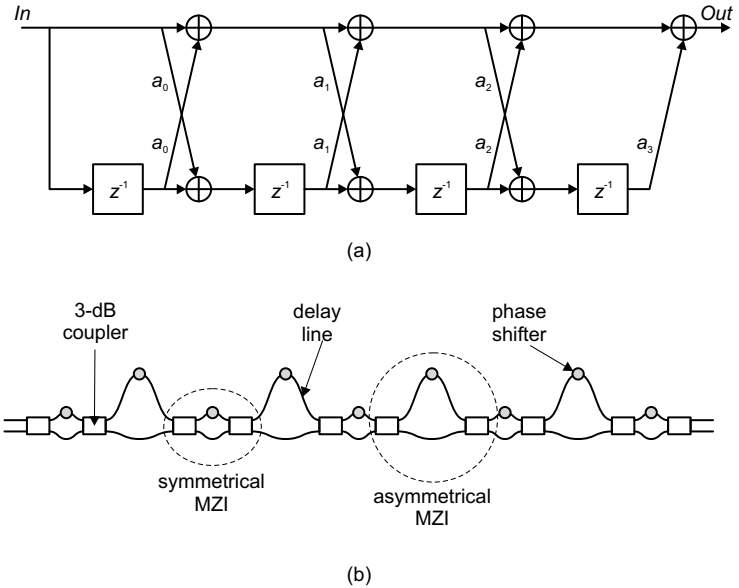

Figure 1.4: (a) Principle of a FIR lattice filter. (b) Implementation of the FIR lattice filter cascading symmetrical and asymmetrical Mach-Zehnder interferometers [39].

In a FIR lattice filter the output signal is given from the superposition

of the present input signal with past values of it weighted with specific coefficients a_i, as shown on Fig. 1.4(a). This principle can be implemented cascading N asymmetrical and $N + 1$ symmetrical Mach-Zehnder interferometers as indicated on Fig. 1.4(b). The symmetrical MZI exhibits arms with equal length and acts as a variable coupler, since the phase shifters on one interferometer arm permit to adjust the coupling ratio at the output, defining the coefficients a_i. The asymmetrical MZI have arms of different length and are fixed delay and variable phase-shift elements. The filter order is N. Optical FIR filters exhibit complex coefficients [39], which give more degrees of freedom in tailoring the filter response. Furthermore this response is periodic in frequency, with a free spectral range (FSR) which is related to the delay of the MZI:

$$\Delta\lambda_{FSR} = \frac{\lambda_0^2}{c}\frac{1}{\Delta\tau_{MZI}} \tag{1.15}$$

where λ_0 is the central wavelength and $\Delta\tau_{MZI}$ is the delay of an asymmetrical MZI and is given by the length difference of the two interferometer arms:

$$\Delta\tau_{MZI} = \frac{\Delta L_{MZI}}{v_g}. \tag{1.16}$$

Considering N cascaded asymmetrical MZIs, the maximal group delay difference between two spectral components of the incoming signal is hence:

$$\Delta\tau_{max} = N \cdot \Delta\tau_{MZI} \tag{1.17}$$

Assuming that the filter can be tuned in a way to achieve a linear trend for $\Delta\tau(\lambda)$ over a FSR, the maximal dispersion which can be reached is:

$$D_{max} = \frac{\Delta\tau_{max}}{\Delta\lambda_{3\text{dB}}} \tag{1.18}$$

where $\Delta\lambda_{3\text{dB}}$ is the 3-dB bandwidth within a FSR.

Such filter structures have been demonstrated on silica waveguides [40] showing dispersion values between -681 and +786 ps/nm over a bandwidth of 0.13 nm and on SiON waveguides [41] with dispersion values of $\pm$100 ps/nm over a bandwidth of 0.5 nm.

Serial IIR lattice filters based on ring resonators have been demonstrated for this purpose as well [42, 43], and the corresponding principle is shown on Fig. 1.5. It is based on a repetition of a unit cell, constituted by a ring resonator coupled to a bus waveguide with a variable coupler and a phase shifter on the ring. At the coupling wavelength an increase of the group delay is achieved, function of the coupling strength κ and phase

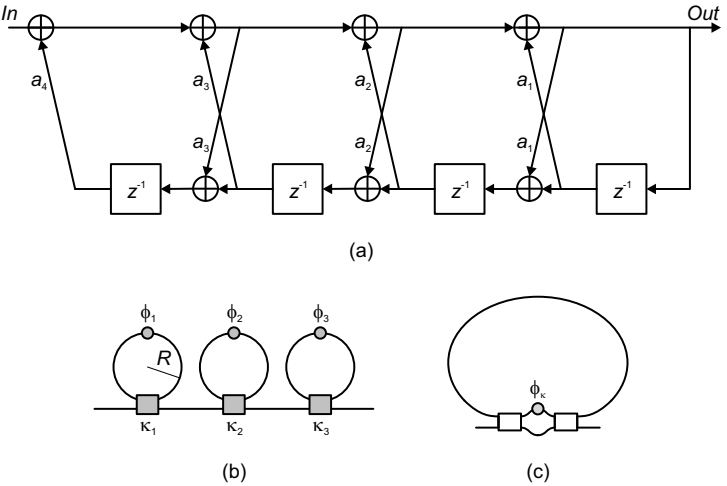

Figure 1.5: (a) Principle of a IIR lattice filter. (b) Implementation of the IIR lattice filter cascading ring resonators with radius R and phase shifters ϕ_n along a bus with tunable couplers κ_n. (c) Implementation of the tunable coupler with a symmetrical MZI and a phase shifter ϕ_κ [42].

ϕ. Cascading several unit cells and tuning them separately it is possible to tailor the overall filter response and achieve the desired group delay profile. The variable coupler is implemented again with a symmetrical MZI with a phase shifter (see Fig. 1.5(c)). While in the case of the FIR filter the FSR is determined by the difference of the optical path between the arms, in IIR filters it depends on the absolute optical length of the ring, hence the ring radius R:

$$\Delta\lambda_{FSR} = \frac{\lambda_0^2}{2\pi n_g R}. \tag{1.19}$$

The FSR has to be adapted to the channel spacing of the input signal, hence for dense systems, small ring radii are required, with consequently higher radiation losses and stronger technological requirements. Dispersion values about 1800 ps/nm with an FSR of 25 GHz and a passband of 14 GHz have been reported using a four-stages filter [42].

1.3.3 Parallel optical filters

VIPA

A dispersion compensator based on virtually imaged phased array (VIPA) [44] has been presented [45] and is schematically depicted on Fig. 1.6(a). The idea of the device is to spatially separate the spectral components of the input signal and let them propagate along different paths, in order to add a specific dispersion.

The input signal coming from a fiber is collimated and then line-focused on a tilted glass plate with a semi-cylindrical lens. The input side of the plate has 100% reflection coating except in the light incident window area, which is antireflection (AR) coated. The output side of the plate has a high-reflection coating which has 98% reflectivity. A small portion of the light entering the plate (2% in power) passes through the high-reflection coating and diverges after the beam waist, as shown in Fig. 1.6(b). The rest of the light is reflected twice in the plate and another small portion of the reflected light passes through the high-reflection coating. In a similar way, the input light is split into many light paths which have a constant displacement. Each light path has a beam that seems to be diverging from the beam waist created in a virtual image. The virtual images of the beam waist are self-aligned along the normal of the plate so that the image-to-image spacing is constant at twice the plate thickness. This virtually creates a phased array of light beams. They all interfere with each other after exiting the glass plate and form collimated light, where the light propagates in a particular direction which is determined by the condition of diffraction and is a function of the wavelength. This light is then focused on a mirror which reflects the beam back through the system to the fiber.

The angular dispersion occurring at the output of the glass plate is used to separate the spectral components of the input signal. Different wavelengths exit the glass plate with different angles, reaching the mirror at different positions.

For simplicity, the case depicted in Fig. 1.6 is considered, where only three wavelengths $\lambda_1 < \lambda_2 < \lambda_3$ are taken into account. They exit the glass plate with different angles. Assuming that the wavelength λ_2 reaches the center point on the mirror, the shorter wavelength λ_1 travels slightly upward at the output of the glass plate and is focused at a higher point on the mirror. According to the same principles the longer wavelength λ_3 is focused at a lower point on the mirror. Varying the curvature of the mirror surface, it is possible to modify the phase of the three spectral components and achieve the desired chromatic dispersion.

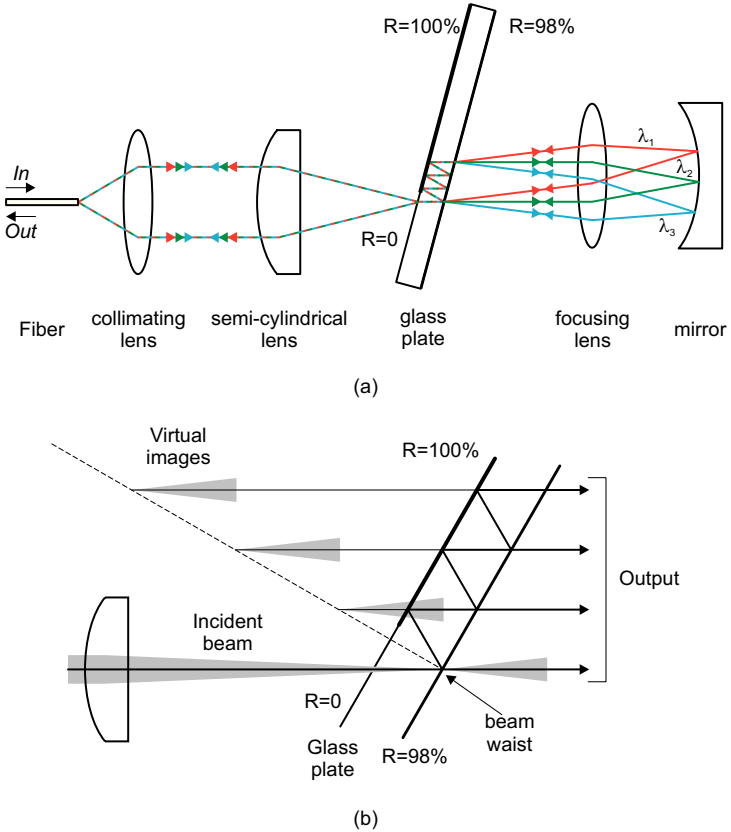

Figure 1.6: Schematic structure of a dispersion compensating system based on VIPA.

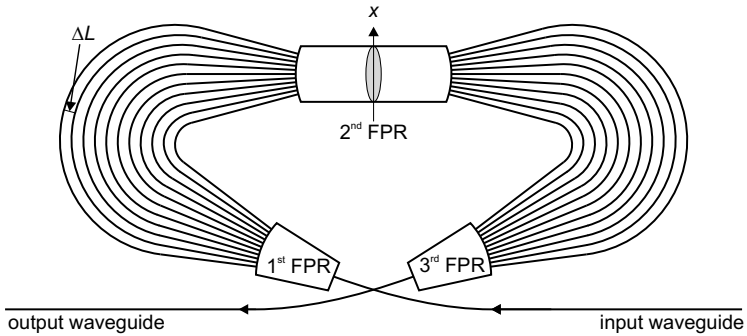

Figure 1.7: Principle of a dispersion compensator based on two AWGs connected by a free propagation region (FPR) [47].

Experiments showed that a dispersion of 1800 ps/nm can be achieved over a bandwidth of 0.4 nm for 60 channels over a 50 nm wavelength range [45]. This dispersion can also be tuned varying the tilt angle of the glass plate and the shape of the mirror, adapting the optical path of the different wavelengths to the required dispersion shape. The disadvantage of the device is the insertion loss of 10 dB and the mechanical stability of the system, based on discrete optical elements. A device based on a similar principle realized with a diffraction grating and MEMS mirrors has been also demonstrated [46]. With this procedure a tunable and compact device has been achieved, able to compensate a dispersion between 4.6 and 16.7 ps/nm over a bandwidth of 2.5 nm, with an insertion loss of 10 dB.

Arrayed waveguide gratings (AWG)

A particular integrated implementation of the VIPA concept has been proposed [47–50]. Here the separation of the spectral components occurs using arrayed waveguide gratings (AWG), which acts like the tilted glass plate shown on Fig. 1.6.

The structure consists of two cascaded identical AWGs with one common free propagation region (FPR). The light propagates through the component beginning with the input waveguide, through the first FPR, couples into the first AWG, where it is then divided into its spectral components. For different wavelengths, the input waveguide mode field is imaged at different positions on the middle focal plane of the second FPR indicated with x. In this focal plane, a lens is provided, which permits

to control the phase of the different wavelengths. The light propagates through the lens to the end of the second FPR, through the second AWG, and through the third FPR, where its spectral components are recombined, to the output waveguide.

The difference in propagation length ΔL between adjacent waveguides in the array corresponds to a group delay difference $\Delta\tau_{AWG}$ which determines the free spectral range of the device $FSR = 1/\Delta\tau_{AWG}$. This *FSR* hast to be adapted to the channel spacing of the system which has to be compensated.

For the implementation of the tunable lens on the plane x a thermal lens has been proposed [48], showing dispersion values of ± 200 ps/nm over a bandwidth of 0.3 nm, however with a power consumption up to 7.3 W. An alternative solution with higher dispersion up to ± 500 ps/nm over a bandwidth of 0.56 nm with lower power consumption has been also demonstrated replacing the lens and the second AWG with a deformable mirror and operating the device in reflection [49, 50].

1.3.4 Serial-parallel optical filters

A drawback which occurs with the concept based on AWGs is that the shorter- and longer-wavelength spectral portions experience increased loss, because they focus at a nonzero angle on the output waveguides. This rounds the transmissivity passband, narrowing the signal bandwidth [51]. On the other hand serial approaches based on 2×2 couplers and delay lines are easy to design and require less power for the driving elements compared to the parallel approaches. However a large number of stages are required, since each of them brings an individual contribution to the overall dispersion.

A compromised filter architecture has been proposed, which can mitigate the limitations of both serial and parallel approaches, cascading N AWGs with M arms [51]. It permits to increase the achievable dispersion and the transmissivity passband. If M reduces to 2, the structure becomes the serial lattice filter dispersion compensator shown in Sec. 1.3.2. The overall dispersion is proportional to the product $M \cdot N$, hence a device with $M = 4$ and $N = 2$ would have the same performance of the case $M = 2$ and $N = 4$, but with a more compact layout.

The serial lattice filter can be therefore parallelized using $M \times M$ MMI couplers, as sketched on Fig. 1.8. The delay length $\Delta\tau_{dl}$ determines the FSR, while the overall delay of a filter stage is $(M-1)\Delta\tau_{dl}$. After N stages, an overall delay of $N(M-1)\Delta\tau_{dl}$ is obtained. The phase shifters on the delay arms permit to tune the transfer function and vary the output disper-

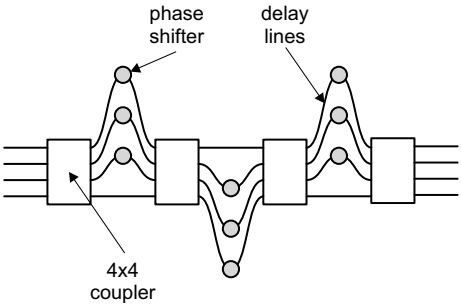

Figure 1.8: General structure of a serial-parallel filter for dispersion compensation.

sion. In [52] an implementation of this serial-parallel approach on silicon rib waveguides with 4×4 MMI couplers has been demonstrated, showing that a dispersion of ± 176 ps/nm over a bandwidth of 0.35 nm can be compensated using a two stage filter.

1.3.5 Comparison

In Table 1.2 a comparison of different concepts for the compensation of the residual dispersion is presented. In each case the basic principle and the material system for the realization are indicated, as well as the achieved performances in terms of maximal dispersion and bandwidth. For a direct comparison the figure the dispersion-bandwidth product as a figure of merit [53] has been considered:

$$FOM = D_{max} \cdot \Delta\lambda_{3\mathrm{dB}}^2. \tag{1.20}$$

It is possible to observe that the bulky solutions exhibit higher values of dispersion, mostly due to the absence of strict limitations in the device dimensions like in integrated structures. On the other side, they are designed to compensate a single channel, as in the case of fiber Bragg gratings. Their reflection bandwidth can be chosen to fully cover the desired channel, without adding additional distortion or losses.

Integrated dispersion compensators exhibit a periodic filter response which permits to simultaneously compensate the dispersion for several channels. This periodicity however limits the bandwidth of each channel, which is always narrower than the free spectral range. This means that part of the signal spectrum are suppressed, with a consequent slight

Compensator type	Material	D_{max} (ps/nm)	$\Delta\lambda$ (nm)	*FOM* (ps·nm)
FBG [35]	Fiber	6000	0.15	135
FBG [36]	Fiber	1500	0.5	375
Serial FIR [41]	SiON	$\pm$100	0.5	25
Serial FIR [40]	Silica	-681 – 786	0.13	13.3
Serial IIR [42]	Silica	$\pm$860	0.13	14.5
VIPA [44]	bulky	$\pm$1800	0.4	288
VIPA with MEMS [46]	bulky	16.7	2.5	104.3
AWG with th. lens [48]	Silica	$\pm$200	0.32	20.5
AWG with def. mirror [49]	Silica	$\pm$500	0.56	156.8
Serial-parallel [51]	Silica	-229 – 224	0.57	71.8
Serial-parallel [52]	SOI	$\pm$176	0.35	21.6

Table 1.2: Performance comparison of different devices for the compensation of the residual dispersion.

distortion. The performances of the presented integrated devices exhibit dispersion values of some hundreds of ps/nm and and bandwidths which cover at most 70% of the 100 GHz channel bandwidth (0.8 nm).

2

Uniform Bragg gratings on SOI rib waveguides

The principle of Bragg gratings, already anticipated in Sec. 1.3.1, has to be described in order to be able to correctly implement the device for the purpose of dispersion compensation. Several efforts have been spent from the early Seventies to develop a model to analyse and design Bragg gratings, since wavelength selective devices are essential for a large number of optical applications. First of all the so-called *coupled mode theory* [54–56] is considered, which permits to achieve a clear understanding of the physical principles. Its applicability is however limited by tight assumptions and can be used only for first approximations.

2.1 Modelling of Bragg gratings

2.1.1 Coupled mode theory (CMT)

On Fig. 2.1 the scheme of a generic planar Bragg grating is shown. A waveguide core of thickness t and refractive index n_2, surrounded by two different cladding materials with index n_1 and n_3 is considered. In the waveguide core a periodic index modulation with period Λ is defined over a length L_g. The propagation direction is set to z.

Assuming that only the fundamental mode propagates in the waveguide, the E_y field can be expressed as the superposition of a forward and a backward travelling wave:

$$E_y = \frac{1}{2}\left(b(z)e_y(x) + a(z)e_y(x)\right) \tag{2.1}$$

where $b(z)$ and $a(z)$ are the normalized mode amplitude of the forward and backward travelling waves respectively, $e_y(x)$ is the transverse electric

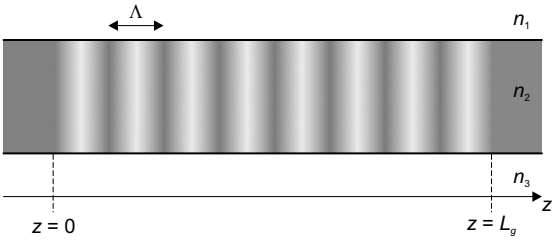

Figure 2.1: Scheme of Bragg grating produced with a periodic index modulation in the waveguide core of thickness t. The overall grating length is L_g. The refractive indices of the cladding, core and substrate are n_1, n_2 and n_3 respectively.

field distribution of the eigenmode. In the regions where the waveguide is uniform, the forward and backward travelling modes are decoupled and propagate independently, according to the equations:

$$\begin{aligned} \frac{db(z)}{dz} &= -j\beta b(z) \\ \frac{da(z)}{dz} &= j\beta a(z). \end{aligned} \tag{2.2}$$

In the grating region a periodic index modulation with amplitude Δn is produced. For simplicity, this modulation is considered sinusoidal, with period Λ:

$$n(z) = n_1 + \Delta n \cdot \sin\left(\frac{2\pi}{\Lambda} z\right). \tag{2.3}$$

This modulation produces a perturbation polarization wave

$$P_y = \Delta n^2 \varepsilon_0 E_y \tag{2.4}$$

which drives an energy coupling between the forward and the backward travelling waves. This energy coupling is described by an additional term in Eq. 2.2 [55]:

$$\begin{aligned} \frac{db(z)}{dz} &= -j\beta b(z) + \kappa a(z) \exp\left(j\frac{\pi}{\Lambda} z\right) \\ \frac{da(z)}{dz} &= j\beta a(z) + \kappa^* b(z) \exp\left(-j\frac{\pi}{\Lambda} z\right). \end{aligned} \tag{2.5}$$

where β is the propagating constant of the unperturbed waveguide. The coupling coefficient κ is given by

$$\kappa = \frac{1}{\lambda n_{eff}} \int_{-\infty}^{+\infty} \Delta n^2(x) \left[e_y(x)\right]^2 dx \tag{2.6}$$

and describes how strong the mode field of the smooth waveguide interacts with the index modulation.

In solving the coupled mode equations it is more convenient to separate the rapid oscillations from $a(z)$ and $b(z)$ to obtain coupled-mode equations for the slowly-varying envelope functions [57]. The rapid oscillations are removed by making the following change of variables:

$$\begin{aligned} A(z) &= a(z) \exp\left(-j\frac{\pi}{\Lambda}z\right) \\ B(z) &= b(z) \exp\left(j\frac{\pi}{\Lambda}z\right). \end{aligned} \tag{2.7}$$

$A(z)$ and $B(z)$ represent the slowly varying mode envelope functions, after the rapid optical oscillations have been factored out. With this substitution, the coupled mode equations become

$$\begin{aligned} \frac{dB(z)}{dz} &= -j\delta B(z) + \kappa A(z) \\ \frac{dA(z)}{dz} &= j\delta A(z) + \kappa^* B(z) \end{aligned} \tag{2.8}$$

where the phase δ indicates the mismatch between the propagation constant of the mode and the fundamental spatial frequency of the grating:

$$\delta = \beta - \frac{\pi}{\Lambda}. \tag{2.9}$$

The coupled mode equations can be rewritten as a linear system of coupled differential equations in matrix form:

$$\frac{d}{dz}\begin{pmatrix} B \\ A \end{pmatrix} = \begin{pmatrix} -j\delta & \kappa \\ \kappa^* & j\delta \end{pmatrix}\begin{pmatrix} B \\ A \end{pmatrix} \tag{2.10}$$

which can be solved via eigenvectors decomposition [58]:

$$\begin{pmatrix} B(z) \\ A(z) \end{pmatrix} = \begin{pmatrix} \mathbf{v}_1 & \mathbf{v}_2 \end{pmatrix}\begin{pmatrix} \exp(\zeta_1 z) & 0 \\ 0 & \exp(\zeta_2 z) \end{pmatrix}\begin{pmatrix} \mathbf{v}_1 & \mathbf{v}_2 \end{pmatrix}^{-1}\begin{pmatrix} B(0) \\ A(0) \end{pmatrix}. \tag{2.11}$$

The eigenvalues $\zeta_{1,2}$ are

$$\zeta_1 = S \qquad \zeta_2 = -S \tag{2.12}$$

where

$$S = \sqrt{|\kappa|^2 - \delta^2}. \tag{2.13}$$

and the eigenvectors $\mathbf{v}_{1,2}$

$$\mathbf{v}_1 = \begin{pmatrix} S - j\delta \\ \kappa^* \end{pmatrix} \qquad \mathbf{v}_2 = \begin{pmatrix} -\kappa \\ S - j\delta \end{pmatrix}. \tag{2.14}$$

Substituting, the mode amplitudes at the position z as function of $A(0)$ and $B(0)$ are obtained:

$$\begin{pmatrix} B(z) \\ A(z) \end{pmatrix} = \begin{pmatrix} \cosh(Sz) - j\frac{\delta}{S}\sinh(Sz) & \frac{\kappa}{S}\sinh(Sz) \\ \frac{\kappa^*}{S}\sinh(Sz) & \cosh(Sz) + j\frac{\delta}{S}\sinh(Sz) \end{pmatrix} \begin{pmatrix} B(0) \\ A(0) \end{pmatrix} \tag{2.15}$$

However, only the amplitude of B at the position $z = 0$ is known, while $A(0)$ is the desired value to be calculated. The backward travelling mode $A(z)$ is generated by the grating, hence its amplitude for $z \geq L_g$ has to be zero. With these boundary conditions, the desired solutions of 2.8 are [55]:

$$A(z) = B(0)\frac{j\kappa\exp(-j\delta z)}{-\delta\sinh(SL_g) + jS\cosh(SL_g)}\sinh[S(z - L_g)]$$

$$B(z) = B(0)\frac{\delta\sinh(Sz - SL_g) + jS\cosh(Sz - SL_g)}{-\delta\sinh(SL_g) + jS\cosh(SL_g)}\exp(j\delta z) \tag{2.16}$$

From these expressions it is possible to determine the reflection and the transmission factors of the grating:

$$r = \frac{A(0)}{B(0)} = \frac{\frac{\kappa}{S}\tanh(SL_g)}{1 + j\frac{\delta}{S}\tanh(SL_g)} \tag{2.17}$$

$$t = \frac{B(L_g)}{B(0)} = \frac{\operatorname{sech}(SL_g)}{1 + j\frac{\delta}{S}\tanh(SL_g)} \tag{2.18}$$

The energy coupling between the forward and backward propagating mode due to the periodic index modulation occurs only at specific frequencies. Therefore it is necessary to consider the frequency dependence of Eq. 2.17-2.18. It is contained in the parameters δ and κ. The propagation constant β can be expanded in Taylor series about a frequency ω_B:

$$\beta(\omega) = \beta(\omega_B) + \left.\frac{d\beta}{d\omega}\right|_{\omega=\omega_B}(\omega - \omega_B) = \beta(\omega_B) + \frac{1}{v_g}(\omega - \omega_B) \tag{2.19}$$

where v_g is the group velocity of the unperturbed waveguide (see Eq. 1.4). If ω_B is chosen to be the frequency where $\beta(\omega_B)$ equals the spatial frequency of the grating (see Eq. 2.9), the Taylor expansion of δ about ω_B becomes:

$$\delta(\omega_B) = \beta(\omega_B) - \frac{\pi}{\Lambda} + \left.\frac{d\beta}{d\omega}\right|_{\omega=\omega_B} (\omega - \omega_B) = \frac{(\omega - \omega_B)}{v_g}. \tag{2.20}$$

The frequency ω_B is defined as the Bragg frequency and is given by

$$\omega_B = \frac{c}{n_{eff}} \frac{\pi}{\Lambda}. \tag{2.21}$$

where n_{eff} is the effective index of the guided mode of the unperturbed waveguide. It is useful to express it also in wavelength:

$$\lambda_B = \frac{2\pi c}{\omega_B} = 2n_{eff}\Lambda. \tag{2.22}$$

The frequency dependence of κ is obtained considering the variation of the mode profile $e_y(\omega)$ in Eq. 2.6. Assuming however that the frequency variation is small, the mode profile does not change significantly and can be considered constant. Eq. 2.17-2.18 can be therefore considered as a function of δ only.

If the eigenvectors $\zeta_{1,2}$ are real, the mode power $|A|^2$ and $|B|^2$ exhibit an exponential spatial decay, as depicted on Fig. 2.2. This is due to the backward Bragg scattering, which couples energy from B to A and occurs when

$$\delta \leq \kappa. \tag{2.23}$$

This defines in frequency a stop-band about the Bragg wavelength

$$\Delta\omega_{SB} = 2\kappa v_g \tag{2.24}$$

over which the eigenvalues are real and coupling occurs. Outside this stop-band, the eigenvalues are purely imaginary and the fields can propagate through the grating.

The peak reflectivity is reached at the Bragg frequency for $\delta = 0$:

$$R_{max} = |r(\delta = 0)|^2 = \frac{\kappa^*}{|\kappa|} \tanh^2(\kappa L_g). \tag{2.25}$$

This expression shows how the reflection of the grating is the result of a cumulative process. The coupling constant κ indicates the strength of the

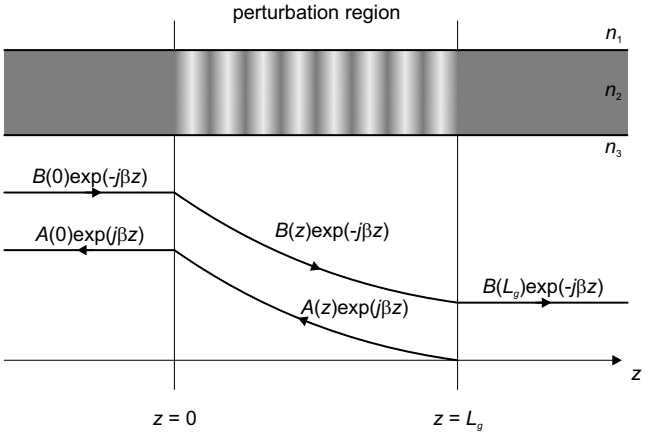

Figure 2.2: Spatial evolution of the mode amplitude of the forward and backward travelling modes in the grating.

reflection at a single grating interface, which is summed over the length L_g.

For $\kappa L_g < 1$ the grating is considered a *weak Bragg grating* and the expression of the spectral response can be simplified expanding Eq. 2.17 about κ/δ. Neglecting the higher order terms, the reflectivity becomes [58]:

$$r(\delta) \approx -\frac{\kappa}{\delta}\sin(\delta L_g)\exp(j\delta L_g) \tag{2.26}$$

The reflectivity spectrum can be hence approximated with a "sinc" function, whose bandwidth is inversely proportional to the grating length L_g and a linear phase term. This result can be better understood solving directly the coupled mode equations 2.8 for $A(z)$ [59]:

$$A(z) = \exp(j\delta z)\left(\int_{-\infty}^{+\infty} B(z')\kappa(z')\exp(-j\delta z')dz'\right). \tag{2.27}$$

Since $B(z)$ is also an unknown, an assumption has to be performed to simplify the solution. Considering the grating weak, the energy subtracted from the forward travelling wave is small and $B(z)$ can be considered con-

stant and equal to $B(0)$. With this assumption, the reflected wave becomes:

$$A(z) = \exp(j\delta z)B(0)\left(\int_{-\infty}^{+\infty}\kappa(z')\exp(-j\delta z')dz'\right). \tag{2.28}$$

This expression shows that in the case of a weak grating, the reflected signal is spectrally the Fourier transformation of $\kappa(z)$. Considering the grating uniform, the coupling constant profile is a rectangular function with basis L_g. Its spectrum is described hence by a "sinc" function with a main lobe width inversely proportional to L_g.

On Fig. 2.3 reflection spectra for different values of κL_g are shown. Increasing the value of this factor the peak reflectivity increases until the maximum of 1. Two different ways of changing the factor are considered: either the coupling factor κ or the grating length L_g is increased, keeping the other parameter constant. Increasing the grating depth and hence the coupling factor, the interaction between the mode field and the index modulation is larger, leading to a broadening of the reflection bandwidth. For large values (strong grating) a flat reflection curve over a large bandwidth is observed. Keeping the grating depth fixed and increasing the grating length a different effect is noticed. The reflectivity increases, but the bandwidth becomes narrower. This can be explained considering the Fourier approximation of the reflectivity spectrum; increasing the length, the width of the main lobe of the "sinc" function reduces, ideally becoming a delta function for L_g tending to infinity.

2.1.2 Numerical analysis of Bragg Gratings

The description of Bragg gratings provided by the coupled mode theory is simple and permits to have an idea about the behavior of Bragg gratings and the influence of the geometrical parameters. However it is based on the assumption that only one forward and one backward mode propagate into the waveguide and that the grating index modulation produces a perturbation on the mode field of the smooth waveguide. This assumption can be accepted in the case where the grating is obtained modulating the refractive index of the waveguide core, keeping the geometry unchanged, like in fiber Bragg gratings. In silicon waveguides this in not possible, and the index modulation is achieved with different techniques.

Different techniques have been proposed for the implementation of Bragg gratings on rib waveguides. A modulation of the core refractive index achieved with ion implantation [60, 61] or ion beam milling [62] has been demonstrated. However there techniques are relatively invasive and

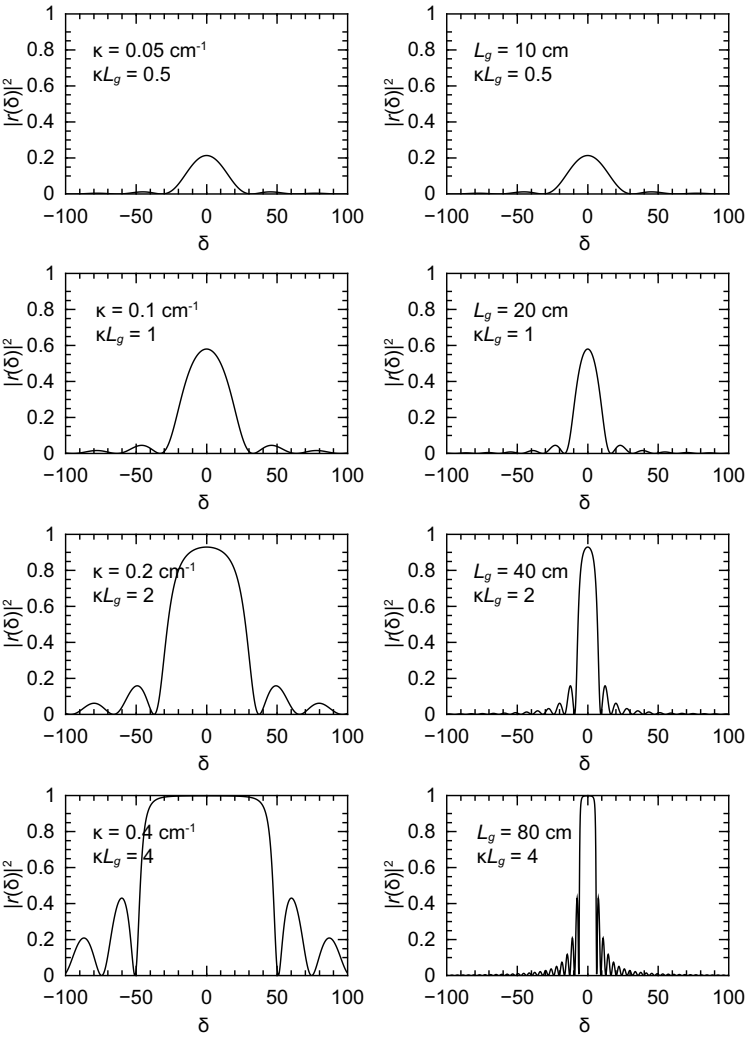

Figure 2.3: Reflectivity spectra of a Bragg grating with variation of the parameter κL_g. Left column: variation of κ and grating length L_g = 10 cm. Right column: variation of L_g with coupling factor constant κ = 0.05 cm^{-1}.

increase noticeably the waveguide losses. The realization of grating with surface corrugation instead permits to keep the material properties unchanged, limiting the amount of added losses.

In this case the grating consists of a periodic concatenation of waveguides with different heights, where modes with different shapes propagate. It is therefore not possible to arbitrarily assume that the perturbation produces a coupling between the forward and backward propagating fundamental modes of the smooth waveguide. If the grating exhibits deeper trenches the mode shape of the light guided in the lower waveguide section differs noticeably from the one of the smooth waveguide. And beyond a certain trench depth the light is even no longer guided. This means that the coupled mode theory can be considered reliable to model a grating with a shallow corrugation, where the mode profile can be considered almost unchanged and the other waveguide modes are left unexcited. In the case of deeper trenches a more rigorous method should be applied, which considers the different mode profiles within the grating sections and different modes. Two different numerical methods for the modelling of Bragg gratings are considered in this section: the Finite-Difference Time-Domain (FDTD) method and the Bidirectional Eigenmode Propagation (BEP) technique.

Finite-Difference Time-Domain method (FDTD)

The Finite-Difference Time-Domain (FDTD) technique represents a widely used propagation solution technique in integrated optics. It can solve complicated problems and can provide almost exact solutions for a large variety of situations, but it is generally computationally expensive. Solutions may require a large amount of memory and computation time.

The algorithm was proposed by Yee [63] and is based on direct integration in the time domain of the Maxwell curl equations in discretized form via central differences in time and space. For example the z component of the curl **H** equation

$$\left[\frac{\partial H_y}{\partial x} - \frac{\partial H_x}{\partial H_y}\right] = \varepsilon \frac{\partial E_z}{\partial t} \tag{2.29}$$

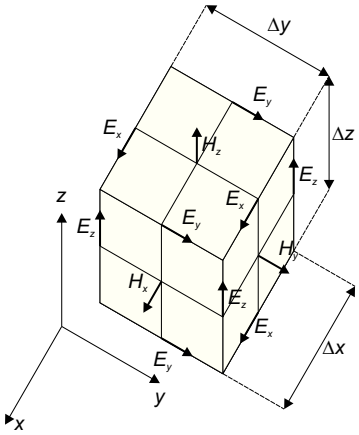

Figure 2.4: Scheme of a Yee-cell of dimension Δx, Δy and Δz. The H field is computed at points shifted one half grid spacing from the E field grid points.

becomes [64]

$$\left[\frac{H_y^{t+\frac{\Delta t}{2}}(x+\frac{\Delta x}{2},y,z)-H_y^{t+\frac{\Delta t}{2}}(x-\frac{\Delta x}{2},y,z)}{\Delta x}\right]+$$
$$-\left[\frac{H_x^{t+\frac{\Delta t}{2}}(x,y+\frac{\Delta y}{2},z)-H_x^{t+\frac{\Delta t}{2}}(x,y-\frac{\Delta y}{2},z)}{\Delta y}\right]=$$
$$=\varepsilon\left[\frac{E_z^{t+\Delta t}(x,y,z)-E_z^{t}(x,y,z)}{\Delta t}\right] \tag{2.30}$$

where $E_z^t(x,y,z)$ indicates the z component of the electric field evaluated at the time t. The grid is staggered in time and space (the so-called Yee mesh [63], see Fig. 2.4), and the equations for the other field components follow this form.

Solving the equations for the future term, i.e. for the electric fields at the time step $t+\Delta t$, the so-called update equation is obtained. It is a generic equation which can be applied at any electric-field node and shows that the future value of E_z depends on only its previous value and the neighboring magnetic fields. At the now computed electric field nodes the discretized curl **E** equation is applied, producing update equations for the

magnetic field at the subsequent half time step. This means that for every time step the update equations for the electric field and for the magnetic field at every grid point have to be computed. It is easy to understand that the computation complexity can dramatically increase for large structures. Furthermore the method is numerically stable only if the following condition is satisfied [65]:

$$c\Delta t \leq \frac{1}{\sqrt{\frac{1}{\Delta x^2} + \frac{1}{\Delta y^2} + \frac{1}{\Delta z^2}}}. \tag{2.31}$$

This limit further increases the number of computations in the case of small structures, which require a small grid size to be resolved.

A successful computation of Bragg gratings with the FDTD technique has been demonstrated [66]. To resolve the structure a grid size of $\Lambda/10$ in the x direction, $\Lambda/18$ in the y direction and $\Lambda/20$ in the z direction was necessary, and the simulations were run for 2^{19} time steps (propagation length of about 1 cm) to ensure a fine spectral resolution. This was achieved using a Gaussian pulse as launched source with a transverse profile matching the waveguide fundamental mode and computing the fast Fourier transform of the reflected and transmitted fields. This permits not to repeat the calculation at every wavelength of interest.

Bidirectional eigenmode propagation method (BEP)

The bidirectional eigenmode propagation algorithm (BEP) is widely used for modelling high-contrast waveguide structures with non-negligible or even strong back-reflections like transitions between dissimilar waveguides, waveguide Bragg gratings, and photonic crystal structures thanks to its precision and simplicity. The application of the BEP method to optical waveguide structures was consistently described for the first time by Sztefka *et al.* [67] and was further developed [68, 69].

In Fig. 2.5 the longitudinal section of the considered waveguide structure is sketched. For simplicity we consider here only the 2D case with one transversal coordinate x and the longitudinal coordinate z. This limitation allows to consider fields of TE and TM polarization separately. It consists of a concatenation of several longitudinally uniform waveguide sections (labeled by $s = 1, ..., S$). Each waveguide section is considered as a multilayer waveguide, composed of layers $l = 1^{(s)}, ..., L^{(s)}$ with permittivities $\varepsilon_l^{(s)}$. In order to discretize its spectrum of eigenmodes, the whole waveguide structure is laterally bounded by two perfectly reflecting electric or magnetic walls. If needed, the unwanted parasitic reflections from the walls can be suppressed by perfectly matched layers.

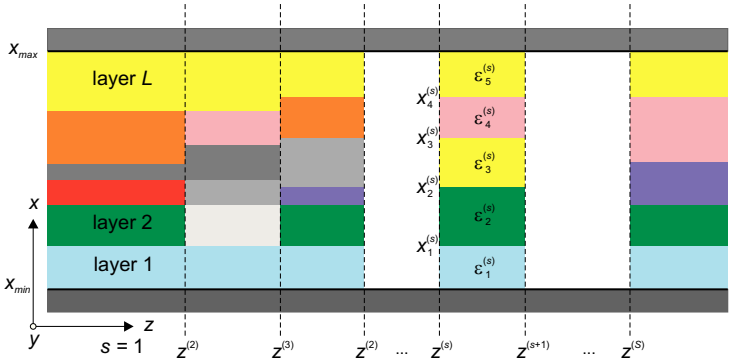

Figure 2.5: Schematic drawing of a generic waveguide with several discontinuities at the positions $z^{(s)}$.

In each section s, a set of eigenmodes $f_m^{(s)}(x)$ and the corresponding propagation constants

$$\beta_m^{(s)} = (2\pi/\lambda) n_{eff,m}^{(s)}, \quad m = 1, ..., M \tag{2.32}$$

is to be calculated. Here $f_m^{(s)}(x)$ stands for E_y and H_y for TE or TM polarization respectively and $n_{eff,m}^{(s)}$ are the effective refractive indexes of the corresponding modes. The field distribution in section s can be expressed as a superposition of eigenmodes:

$$E_y^{(s)}(x,z) = \sum_{m=1}^{M} p_m^{(s)}(z) f_m^{(s)}(x), \quad H_x^{(s)} = \sum_{m=1}^{M} n_{eff,m}^{(s)} q_m^{(s)}(z) f_m^{(s)}(x), \tag{2.33}$$

for the TE mode and

$$H_y^{(s)}(x,z) = \sum_{m=1}^{M} p_m^{(s)}(z) f_m^{(s)}(x), \quad E_x^{(s)} = \sum_{m=1}^{M} \frac{n_{eff,m}^{(s)}}{\varepsilon^{(s)}(x)} q_m^{(s)}(z) f_m^{(s)}(x), \tag{2.34}$$

for the TM mode, where $p_m^{(s)}(z)$ and $q_m^{(s)}(z)$ are the complex amplitudes of the modes fields.

It follows from Maxwell equations that the vectors of the complex amplitudes $\mathbf{p}^{(s)}(z)$ and $\mathbf{q}^{(s)}(z)$ (with components $p_m^{(s)}(z)$ and $q_m^{(s)}(z)$, respectively) can be expressed as a superposition of amplitudes of forward and

backward propagating modes

$$\mathbf{p}^{(s)}(z) = \mathbf{a}^{(s)}(z) + \mathbf{b}^{(s)}(z), \quad \mathbf{q}^{(s)}(z) = \mathbf{a}^{(s)}(z) - \mathbf{b}^{(s)}(z). \tag{2.35}$$

Defining $\mathbf{N}^{(s)}$ a diagonal matrix of the effective indexes of the modes of section s, the forward and backward propagating modes can be expressed as:

$$\begin{aligned} \mathbf{a}^{(s)}(z + \Delta z) &= \exp(j\mathbf{N}^{(s)}\Delta z) \cdot \mathbf{a}^{(s)}(z), \\ \mathbf{b}^{(s)}(z + \Delta z) &= \exp(-j\mathbf{N}^{(s)}\Delta z) \cdot \mathbf{b}^{(s)}(z). \end{aligned} \tag{2.36}$$

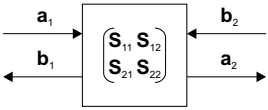

Figure 2.6: Scattering matrix of a generic two-port component.

In linear devices, the amplitudes of outgoing modes propagating in the port waveguides are linearly related to the amplitudes of ingoing modes by the scattering matrix (see Fig. 2.6):

$$\begin{pmatrix} \mathbf{b}_1 \\ \mathbf{a}_2 \end{pmatrix} = \begin{pmatrix} \mathbf{S}_{11} & \mathbf{S}_{12} \\ \mathbf{S}_{21} & \mathbf{S}_{22} \end{pmatrix} \cdot \begin{pmatrix} \mathbf{a}_1 \\ \mathbf{b}_2 \end{pmatrix}. \tag{2.37}$$

The scattering matrix $\mathbf{S}$ has a size of $2M \times 2M$ and can be split in four submatrices of size $M \times M$. From Eq. 2.36 the scattering matrix of a uniform waveguide section s of the length Δz is derived:

$$\mathbf{S}^{(s)} = \begin{pmatrix} \mathbf{0} & \exp(j\mathbf{N}^{(s)}\Delta z) \\ \exp(j\mathbf{N}^{(s)}\Delta z) & \mathbf{0} \end{pmatrix}. \tag{2.38}$$

Since no gain is present, the amplitude of all the matrix elements does not exceed the unity.

At the interfaces between two sections s and t, the continuity of tangential field intensity components leads to the following relations between the amplitudes of forward and backward waves at both sides of the interface [68]:

$$\begin{pmatrix} \mathbf{b}^{(s)} \\ \mathbf{a}^{(t)} \end{pmatrix} = \begin{pmatrix} -\left(\mathbf{U}^{(ts)}\right)^{-1} \cdot \mathbf{V}^{(ts)} & \left(\mathbf{U}^{(ts)}\right)^{-1} \\ \mathbf{U}^{(ts)} - \mathbf{V}^{(ts)} \cdot \left(\mathbf{U}^{(ts)}\right)^{-1} \cdot \mathbf{V}^{(ts)} & \mathbf{V}^{(ts)} \cdot \left(\mathbf{U}^{(ts)}\right)^{-1} \end{pmatrix} \cdot \begin{pmatrix} \mathbf{a}^{(s)} \\ \mathbf{b}^{(t)} \end{pmatrix} \tag{2.39}$$

where the matrices $\mathbf{U}^{(ts)}$ and $\mathbf{V}^{(ts)}$ are defined in terms of the transition matrices:

$$\mathbf{U}^{(ts)} = \frac{1}{2}(\mathbf{P}^{(ts)} + \mathbf{Q}^{(ts)}),$$
$$\mathbf{V}^{(ts)} = \frac{1}{2}(\mathbf{P}^{(ts)} - \mathbf{Q}^{(ts)}). \tag{2.40}$$

The elements of the transition matrices $\mathbf{P}^{(ts)}$ and $\mathbf{Q}^{(ts)}$ are given by overlap integrals over eigenmodes at the opposite sides of the interface. For the TE polarization:

$$P_{mn}^{(ts)} = \int_{x_{min}}^{x_{max}} f_n^{(s)}(x) f_m^{(t)}(x) dx, \quad Q_{mn}^{(ts)} = \frac{n_{eff,n}(t)}{n_{eff,m}(s)} \int_{x_{min}}^{x_{max}} f_m^{(s)}(x) f_n^{(t)}(x) dx, \tag{2.41}$$

and for the TM polarization:

$$P_{mn}^{(ts)} = \int_{x_{min}}^{x_{max}} \frac{f_n^{(s)}(x) f_m^{(t)}(x)}{\varepsilon^{(s)}(x)} dx, \quad Q_{mn}^{(ts)} = \frac{n_{eff,n}(t)}{n_{eff,m}(s)} \int_{x_{min}}^{x_{max}} \frac{f_m^{(s)(x)} f_n^{(t)}(x)}{\varepsilon^{(t)}(x)} dx. \tag{2.42}$$

Once the scattering matrix for each waveguide section (Eq. 2.38) and for each waveguide transition (Eq. 2.39) is defined, it is possible to obtain the scattering matrix of the concatenation of waveguides and transitions. Considering two matrices $\mathbf{S}^{(1)}$ and $\mathbf{S}^{(2)}$, the four submatrices of the new scattering matrix are given by [68]:

$$\begin{aligned}
\mathbf{S}_{11} &= \mathbf{S}_{12}^{(1)} \cdot \left(\mathbf{I} - \mathbf{S}_{11}^{(2)} \cdot \mathbf{S}_{22}^{(1)}\right)^{-1} \cdot \mathbf{S}_{11}^{(2)} \cdot \mathbf{S}_{21}^{(1)} + \mathbf{S}_{11}^{(1)} \\
\mathbf{S}_{12} &= \mathbf{S}_{12}^{(1)} \cdot \left(\mathbf{I} - \mathbf{S}_{11}^{(2)} \cdot \mathbf{S}_{22}^{(1)}\right)^{-1} \cdot \mathbf{S}_{12}^{(2)} \\
\mathbf{S}_{21} &= \mathbf{S}_{21}^{(2)} \cdot \left(\mathbf{I} - \mathbf{S}_{22}^{(1)} \cdot \mathbf{S}_{11}^{(2)}\right)^{-1} \cdot \mathbf{S}_{21}^{(1)} \\
\mathbf{S}_{22} &= \mathbf{S}_{21}^{(2)} \cdot \left(\mathbf{I} - \mathbf{S}_{22}^{(1)} \cdot \mathbf{S}_{11}^{(2)}\right)^{-1} \cdot \mathbf{S}_{22}^{(1)} \cdot \mathbf{S}_{12}^{(2)} + \mathbf{S}_{22}^{(2)}
\end{aligned} \tag{2.43}$$

where $\mathbf{I}$ is the identity matrix. Iterating the process the scattering matrix $\mathbf{S}_{sys}$ of the entire system is obtained.

From the definition of the scattering matrix the modal reflectance of the fundamental mode of the input section of the whole waveguide structure is given by the first matrix element of the submatrix $\mathbf{S}_{sys,11}$ of the scattering matrix of the whole structure; the transmittance from the fundamental

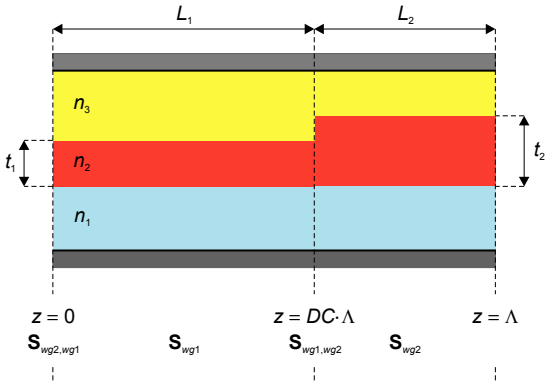

Figure 2.7: Scheme of the simulation model for the computation of the scattering matrix of a grating period.

mode of the input section to the fundamental mode of the output section is similarly given by the first matrix element of the submatrix $\mathbf{S}_{sys,21}$.

The simulation of a Bragg grating with the bidirectional eigenmode propagation is straightforward. The grating is considered as a periodic repetition of two waveguides wg_1 and wg_2 with different heights t_1 and t_2 and with lengths $L_1 = DC \cdot \Lambda$ and $L_2 = (1 - DC) \cdot \Lambda$ respectively. Here DC is the grating duty cycle (see Fig. 2.7). Each period can be described with a scattering matrix, which is the product of the scattering matrix for the first waveguide discontinuity $\mathbf{S}_{wg_2,wg_1}$, the propagation matrix $\mathbf{S}_{wg1}$ in wg_1 for a length L_1, the discontinuity matrix $\mathbf{S}_{wg_1,wg_2}$ and the propagation matrix $\mathbf{S}_{wg2}$ in wg_2 for a length L_2. Once this matrix is given, the overall matrix of the Bragg grating is obtained iterating Eq. 2.43 N_Λ times, where N_Λ is the number of grating periods.

Benchmark structure

In order to evaluate the modelling performance of waveguide Bragg gratings of the presented methods, the simulation of a benchmark structure has been performed. This grating structure has already been proposed for this target in [70]; it consists on a waveguide formed by a Si_3N_4 layer of thickness t = 500 nm deposited onto a SiO_2 substrate, with air as top cladding. On this waveguide a grating of 20 periods is defined, the grating

period is fixed to Λ = 430 nm with a duty cycle DC = 0.5. To evaluate the ability of the simulation tool to model also deeper gratings, three different grating depths d of 125 nm, 375 nm and 625 nm have been considered. Trench depths larger than 500 nm mean that the trench is etched through the guiding layer into the substrate (see Fig. 2.8).

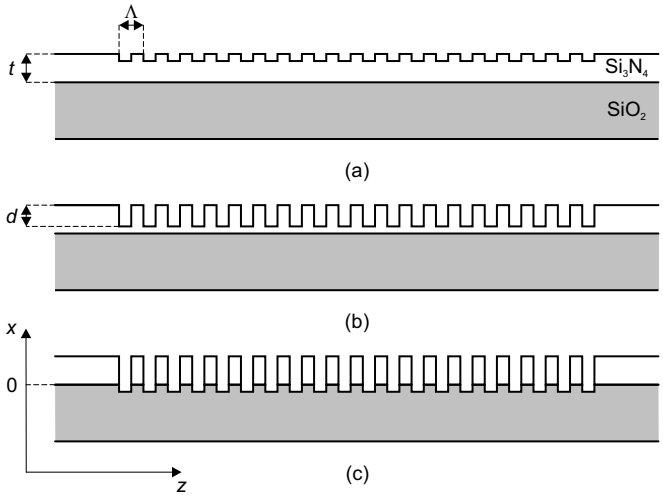

Figure 2.8: Scheme of the considered grating benchmark structure: corrugated Si_3N_4 waveguide of thickness t =500 nm on SiO_2 substrate with periodic trenches with period Λ = 430 nm and different etching depths d: (a) 125 nm, (b) 375 nm and (c) 625 nm.

As implementation of the coupled mode theory the commercial GratingMOD tool from RSoft has been used, for the FDTD the FullWave tool from the same company and for the BEP a Matlab implementation provided by the Technische Universität Hamburg-Harburg (M. Krause, personal communication, 2007–2008). In all three cases the coordinate system indicated in Fig. 2.8(c) has been used. A simulation window of -4 μm $< x <$ 3 μm has been implemented, in order to be able to take into account also the evanescent part of the optical field in air and substrate. The simulations have been run for values of z between 0 and $L_g = 20 \cdot \Lambda$ = 8.6 μm. For the FDTD a grid spacing of $d_{min}/10$ = 12.5 nm in the x direction and $\Lambda/10$ = 43 nm in the z direction has been considered, in order to resolve

the amplitude and the periodicity of the surface corrugation; d_{min} is the grating depth in the shallower case of Fig. 2.8(a). The simulation has been run for 2^{16} time steps using a Gaussian pulse as input field and the spectral response has been calculated via fast Fourier transformation of the transmitted and reflected fields. In the case of the BEP an expansion with 60 modes has been implemented, and the calculation has been repeated for 500 wavelengths in the range of interest between 800 nm and 1800 nm.

The reflection and transmission spectra for the three different grating depths computed with the three different methods are shown on Fig. 2.9. In the case of the shallow etched gratings (d = 125 nm) all three methods produce similar results across the Bragg wavelength, which occurs at λ_B = 1500 nm. At shorter wavelengths a decrease of the grating transmissivity is shown only by the FDTD and BEP calculations, even if with slight differences in the shape, mostly due to the different boundary conditions (PML for the FDTD and metallic walls for the BEP). This drop of the transmissivity has to be attributed to an energy coupling between the forward propagating fundamental mode and leaky modes. At these wavelengths the Bragg gratings acts as a grating coupler which couples light into the substrate and air [70]. This coupling cannot be described by the coupled mode theory, which takes into account only the forward and backward propagating fundamental mode.

Increasing the grating depth, the difference between the results provided by the coupled mode theory and the other two methods becomes more evident. This confirms the assumption that the coupled mode theory is inadequate for the modelling of deep Bragg gratings. Correct results can be obtained with the FDTD method or with the BEP, which show a good agreement with each other. The latter one however exhibits several advantages concerning computation time and memory requirement.

The FDTD requires a finite difference grid to sample the structure and the optical field is resolved at these grid points. The BEP in contrast does not need a grid on the structure if it can be treated analytically. The equivalent of the optical grid in the FDTD is the number of modes in the BEP basis set; the more modes, the higher the spatial resolution that the basis set can resolve [71]. For a straight waveguide the BEP is particularly efficient, since the structure is described with one single scattering matrix, independently on the propagation distance. In contrast the FDTD must discretize even uniform structures. For a periodic structure the FDTD must propagate through each period one after the other, and the grid size should be small enough to resolve the structure periodicity. The BEP on the other side permits to define the scattering matrix of a single period, and from

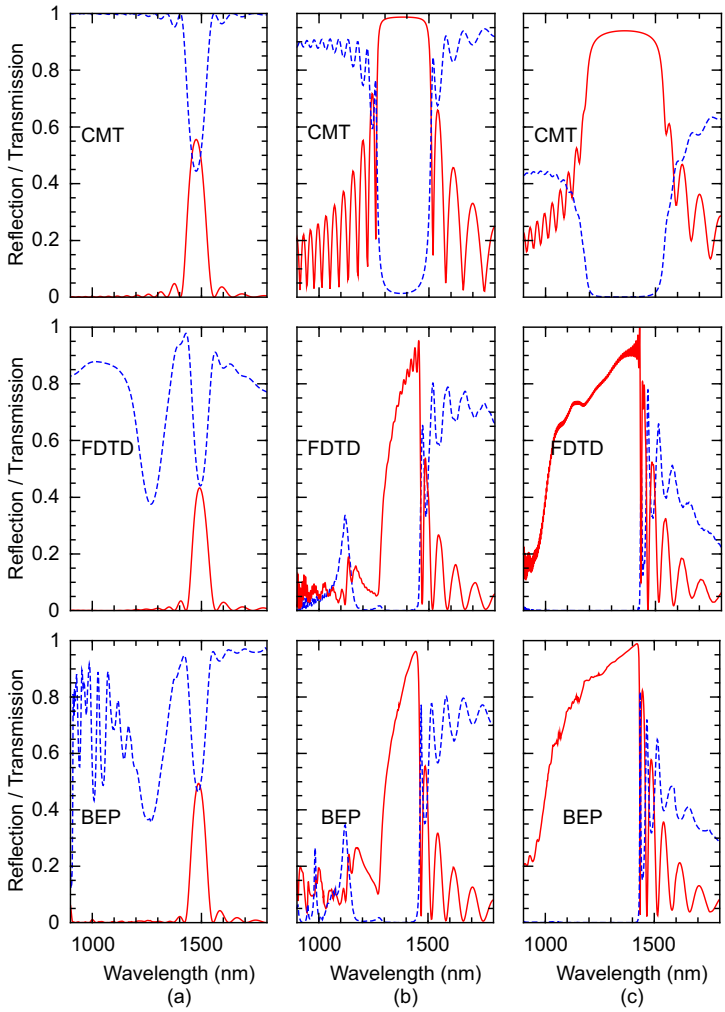

Figure 2.9: Computed reflection (continuous red lines) and transmission (dashed blue lines) spectra for the benchmark grating structure for three different etching depths: (a) 125 nm, (b) 375 nm and (c) 625 nm.

it calculate directly the scattering matrix of the whole structure. Furthermore the FDTD is very intensive memory technique, since it needs to store the field profiles at every grid point for each time step. On the other hand the BEP does not need to store any field profile, since all the needed informations are contained in the scattering matrices.

In the considered case the FDTD required the calculation and the storage of the optical fields for $480 \times 200 = 96000$ points for 2^{16} time steps. This means the computation of fields for about 6.3×10^9 points. The BEP on the other hand required the calculation of 120 modes (60 for each of both waveguide sections of the period) and the 120×120 large scattering matrices. Only the latter ones however had to be stored in memory to be multiplied subsequently for the generation of the grating scattering matrix. This computation had to be repeated for the 500 considered wavelengths, i.e. the computation of 7.2×10^6 scattering coefficients. It can be observed that the memory requirement of the BEP has been definitely lower than the one of the FDTD. All these arguments suggest that the BEP can be considered a preferred method for the grating modelling.

2.2 Design of Bragg gratings on SOI rib waveguides

Applying the introduced bidirectional eigenmode propagation method, a design of Bragg gratings on silicon integrated waveguides has been performed. The design purpose is to achieve gratings which can be practically used for the compensation of the chromatic dispersion. This means that a Bragg grating with a high selectivity should be obtained, able to select a portion of a WDM 100 GHz channel. A bandwidth smaller than 1 nm is hence required, with a reflectivity close to 1 and the lowest loss possible outside the reflection bandwidth, in order not to affect the other channels, which should be transmitted unchanged.

Numerical simulations have been performed to observe how the geometrical parameters of the grating (Fig. 2.10) influence the fulfillment of the cited conditions. After defining the proper waveguide height t, a grating design has been obtained tuning the trench depth d of the grating, the overall length L_g and the duty cycle $DC = u/\Lambda$, defined as the ratio between the length of the grating trenches u and the period Λ, see Fig. 2.10.

2.2.1 Simulation procedure

The simulation of Bragg gratings on a rib waveguide would require a 3D modelling tool, because of the light confinement in both x and y direc-

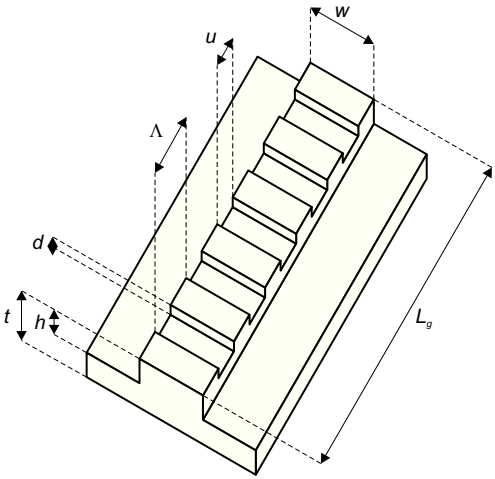

Figure 2.10: Geometrical parameters of a silicon-on-insulator rib waveguide Bragg grating: L_g overall length, d grating depth, u grating trench, Λ grating period, w waveguide width, t rib height.

tions. However the computation of the modes of such a structure cannot be performed analytically like in planar waveguides.

In order to obtain a principal overview of the potential of Bragg gratings on rib waveguides, it is intuitive to represent the three-dimensional structure by a two-dimensional slab waveguide grating extending ideally the rib width w to infinity. In the three dimensional case it is possible to have a single mode rib waveguide properly choosing the rib width and the rib height [72]. If w is extended to infinity, the corresponding slab waveguide will be however multimode. This means that in a Bragg grating on a rib waveguide the energy coupling occurs only to the only one backward guided mode and to radiating ones. In the Bragg gratings on the slab waveguide the coupling occurs also to guided higher order backward travelling modes. Associating the fundamental mode of the slab waveguide with the guided mode of the rib waveguide, all the energy which is coupled (reflected or transmitted) into other modes in the slab grating will then be considered as loss in the three dimensional structure. Because of the reduction of the model to a two-dimensional slab model, a discrimina-

tion between the two orthogonal polarizations does not give meaningful insight; the analysis has been therefore restricted to the TE polarization.

It is straightforward that the effective index of the fundamental mode of the slab waveguide is slightly different from the effective index of the guided mode of the associated rib waveguide. This has influence on the position of the Bragg wavelength and means that a correction of the grating period has to be performed when translating the calculated grating parameters in two dimensions to the three dimensional case.

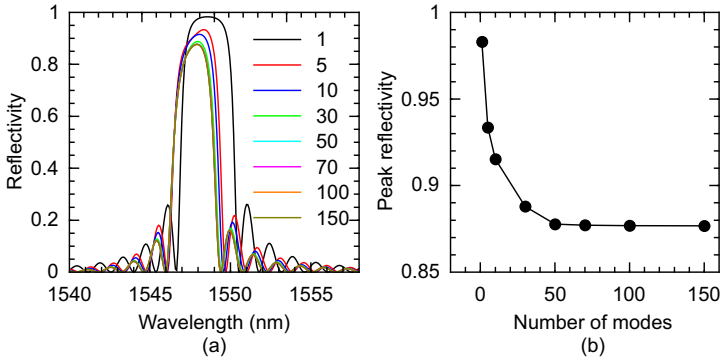

Figure 2.11: (a) Calculated reflectivity spectra of a SOI planar Bragg grating for different numbers of modes in the BEP expansion. (b) Calculated peak reflectivity as function of the number of modes of the expansion.

The basic requirement to achieve reliable results with the BEP is that enough modes are taken into account in the expansion. It is also evident that the larger the number of modes, the higher is the computation complexity. Therefore, as a first step, the lowest acceptable number of modes for reliable results has been calculated. A planar SOI Bragg grating was considered with a grating depth d = 150 nm, duty cycle DC = 0.5, waveguide thickness t =1.5 μm and period Λ = 225 nm. Different simulations with a variation of the number of expansion modes have been performed and the obtained reflectivity spectra are shown on Fig. 2.11. It can be observed that increasing the number of considered modes the reflectivity peaks decreases, since the coupling to higher order modes is taken into account with more precision. For computations with more than 50 modes the reflectivity spectra overlap perfectly and the value of the peak reflec-

tivity remains constant. This number of modes has been then considered as a limit for the reliability of the BEP and has been used for the subsequent calculations.

2.2.2 Waveguide design

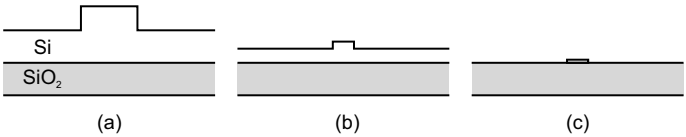

Figure 2.12: Examples of integrated waveguides. (a) Rib waveguides with a guiding layer of $t = 4$ μm, (b) rib waveguide with a guiding layer of 1.5 μm and (c) photonic wire with a guiding layer of 220 nm.

Several waveguide geometries are available and have been demonstrated in silicon-on-insulator. Large rib waveguides with a guiding layer of 4 μm (Fig. 2.12(a)) exhibit low propagation loss in the order of 0.2 dB/cm and an efficient light coupling with single-mode optical fibers. However, due to their size, only bending radii larger than 5 mm are allowed to avoid further losses. On the other side photonic wires (Fig. 2.12(c)) permit a higher integration level thanks their compactness (guiding layer height of 220 nm), but require extra structures for the fiber coupling and exhibit higher propagation losses of about 2 dB/cm. Such higher losses can become a critical issue for the realization of gratings for dispersion compensation, where grating lengths of several millimeters are required. A good compromise is offered from rib waveguides with a guiding layer of 1.5 μm (Fig. 2.12(b)). Their propagation loss is comparable to the one of the larger rib waveguides, but can tolerate tighter bends with radii of 1 mm.

It is important to consider also the strength of the light confinement in the different waveguide geometries. In Fig. 2.13 the normalized amplitudes of the fundamental modes of the three waveguide geometries of Fig. 2.12 are shown. It can be observed that reducing the dimensions of the waveguide, the intensity of the field outside the waveguide core increases. This effect can constitute a challenge for the realization of weak Bragg gratings, since the less the mode is confined in the core, the shallower the surface corrugation has to be to keep the coupling coefficient small. It is proportional to the overlap integral between the mode field and the grating index modulation (see Eq. 2.6). A direct corrugation of

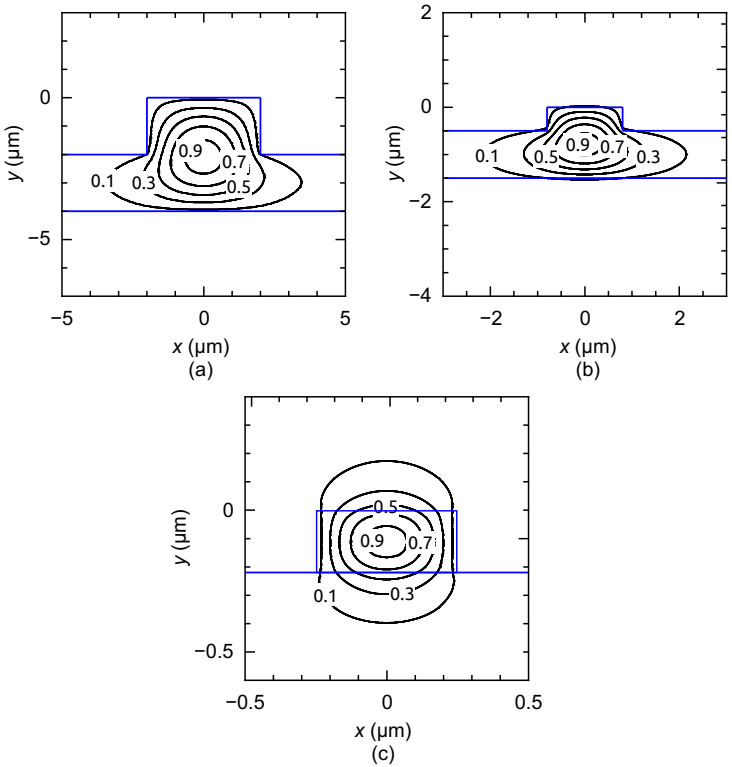

Figure 2.13: Mode profiles of the fundamental TE mode for (a) rib waveguides with a guiding layer of 4 µm, rib width 4 µm and rib height 2 µm, (b) rib waveguide with a guiding layer of 1.5 µm, rib width 1.6 µm and rib height 0.5 µm, (c) photonic wire with a guiding layer of 220 nm and width 400 nm.

photonic wires would interact directly with the core of the mode field (see Fig. 2.13(a)), leading to a strong coupling coefficient κ. The realization of a grating with this waveguide geometry would require more complex approaches, which are not discussed in this work. On the other side larger rib waveguides exhibit a good confinement of the optical field in the silicon layer and a surface corrugation, e.g. on the rib top, interacts only with a low intensity fraction of mode.

In Fig. 2.9 the presence of a drop in the transmission spectra at wavelengths shorter than the Bragg one has been observed. This has to be attributed to the coupling to higher order modes, which cannot be guided in a rib waveguide and constitute a loss. At these wavelengths the condition indicated in Eq. 2.9 is satisfied between the fundamental forward propagating mode and an higher order backward propagating mode, i.e. $(\beta_0^+ - \beta_m^-) = \pi/\Lambda$, with $m > 1$. It is important that such a coupling occurs as far as possible from the Bragg wavelength, in order not to affect the neighboring channels. The mode propagation constant β and its wavelength dependence differs for different waveguide geometries, so that Bragg gratings on different waveguides produce mode coupling at different wavelengths. To analyse this issue, the propagation constant β for the first five forward and backward guided modes as function of the wavelength for three slab waveguides associated to the geometries of Fig. 2.12 have been calculated. On Fig. 2.14 the dependence of β on the wavelength is shown. The dashed lines have a length of π/Λ and show at which wavelengths the forward propagating fundamental mode can couple to backward propagating modes. For the three geometries, the value of Λ has been properly chosen to fulfill the Bragg condition at λ_B = 1550 nm. At this wavelength the coupling occurs to the backward travelling fundamental mode, as desired. For longer wavelengths no coupling is possible, since $(\beta_0^+ - \beta_0^-) < \pi/\Lambda$. For shorter wavelengths the coupling can occur only to higher order modes, since they exhibit a propagation constant lower in amplitude to the one of the fundamental mode.

This coupling has been verified calculating the transmission and reflection spectra of Bragg gratings for the three geometries. In the case of the 4 μm waveguides a period of Λ = 223.3 nm and a grating depth d = 140 nm has been considered. These values have been set to Λ = 225 nm and d = 50 nm for the 1.5 μm waveguides and Λ = 274 nm and d = 1 nm for the 220 nm waveguides. The period has been determined with the Bragg condition considering the effective index of the fundamental mode at λ = 1550 nm and the depth to have a reflection bandwidth of about 1 nm.

The computed spectra show that a drop of the grating transmission occurs at every wavelength where the coupling condition is fulfilled (dashed lines). Only the coupling to the backward travelling fundamental mode leads to a reflection.

Reducing the dimensions of the waveguide, the difference between the propagation constants of the modes increase, leading to a shift towards shorter values of the wavelengths where the undesired couplings occur. The distance between the transmission drop at the Bragg wavelength and

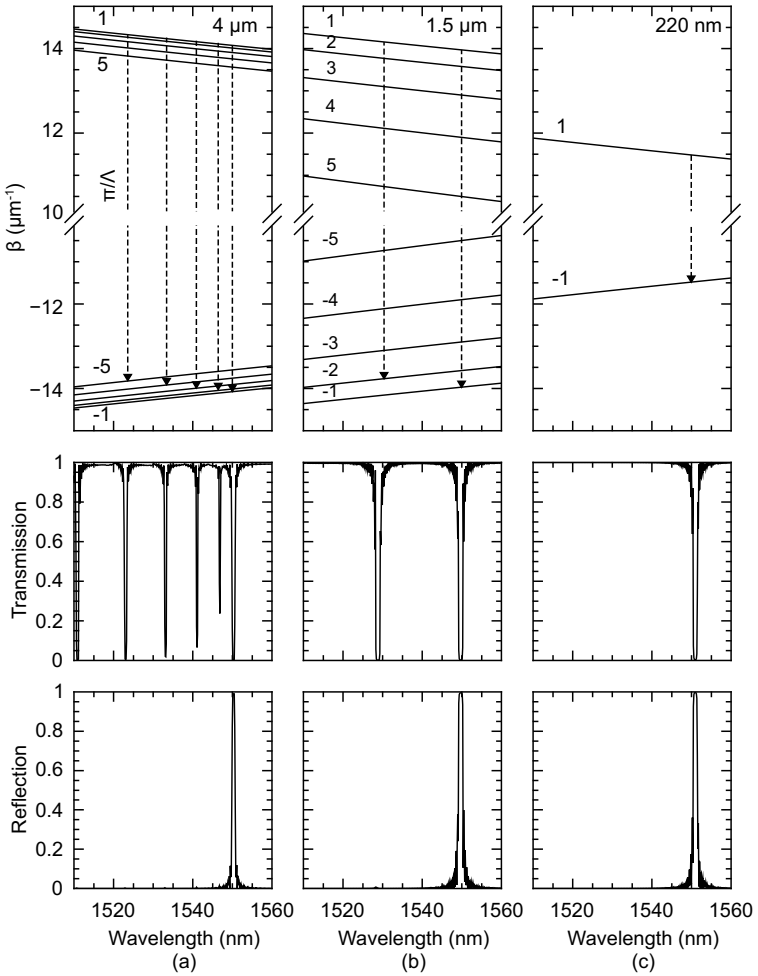

Figure 2.14: Coupling between the forward propagating fundamental mode and the higher order backward propagating modes for the three waveguide geometries. In each case the grating period is adapted to fulfill the Bragg condition for the fundamental mode at $\lambda = 1550$ nm.

the drop due to the coupling of the next order mode is 3.58 nm for the 4 μm waveguide, 19.6 nm for the 1.5 μm waveguide and rises up to several tens of nanometers for the smaller 220 nm waveguide. Together with the previous considerations about the propagation loss and the confinement of the mode field, one can conclude that the rib waveguides with a rib height of 1.5 μm better fit to the aim of this work and are further considered. The distance of 19.6 nm is still smaller than the width of the C-Band of 35 nm. However, considering the scenario of cascaded gratings to separate and compensate several channels, it is sufficient to first drop the channels at short wavelengths, in order to reduce the destructive effect of the coupling to the higher order modes.

2.2.3 Grating design

To evaluate the effect of the geometrical parameters, the peak reflectivity R_{max}, the inserted loss L_{ob} and the reflection bandwidth $\Delta\lambda$ have been computed for different grating depths, duty cycles and grating lengths. First the length of the device has been kept constant to a value of 800 μm. This length is limited by the maximal writing field size of the electron beam lithography which allows writing a reliable grating pattern. The grating depth and the duty cycle have been varied between 0 and 500 nm and between 0 and 1 respectively. In Fig. 2.15(a) the peak reflectivity for the fundamental mode is shown. It can be seen that a high reflectivity is achieved for small duty cycles and large grating depths.

Another effect which has to be taken into account is the shift of the reflectivity peak towards shorter wavelengths with increasing grating depth and duty cycle (see Fig. 2.15(b)). Deeper and larger trenches increase the amount of air in the period, with a consequent reduction of the average effective index.

However the increase of the depth leads also to higher losses in the out-of-band wavelength range where the device should be as transparent as possible, see Fig. 2.15(c). The losses are calculated as the mean value of $L_{ob} = 1 - (R + T)$ for wavelengths larger than $\lambda_B + 2\Delta\lambda$ over a wavelength range of 10 nm. These average losses indicate how much power is out-coupled from the fundamental mode due to the grating perturbation. Fig. 2.15(c) shows that they can be kept below 0.05 dB in the case of shallow gratings (d <50 nm) but can reach values of 5 dB for deeply etched gratings. Furthermore, the losses are scarcely influenced by duty cycles $DC > 0.1$. Fig. 2.15(d) shows how duty cycle and grating depth affect the wavelength selectivity of the grating. Here the bandwidth, defined as the FWHM of the reflectivity peak of the fundamental mode, is repre-

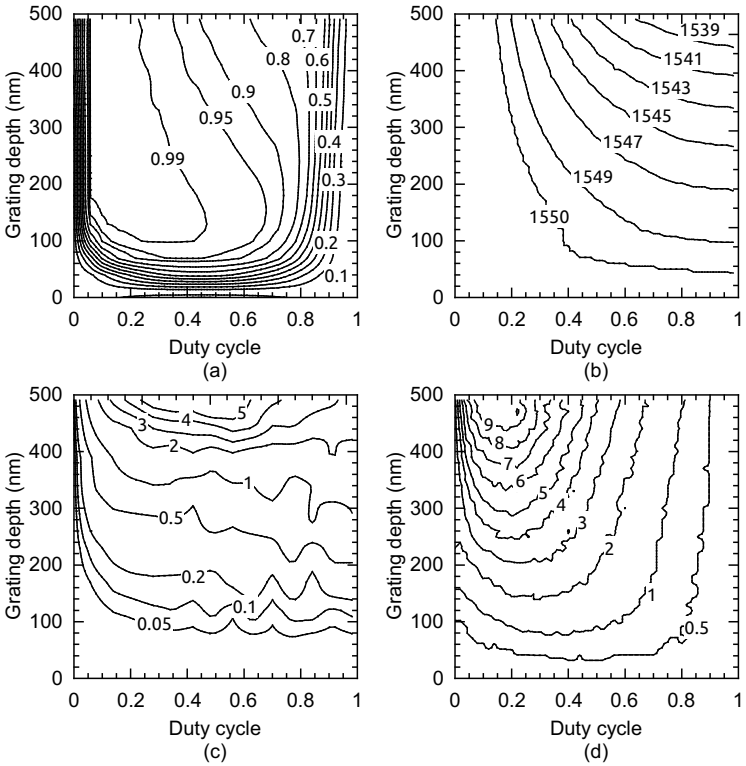

Figure 2.15: (a) Peak reflectivity, (b) reflected wavelength in nm, (c) loss in dB and (d) bandwidth in nm of a Bragg grating with period Λ = 225 nm and length L_g = 800 μm as functions of the grating depth d and the duty cycle DC.

sented. The increase of the trench depth produces a stronger coupling in the neighborhood of the peak wavelength.

From this analysis it is possible to state that the three basic requirements for the Bragg reflectors posed at the beginning of Sec. 2.2 can be satisfied by precisely tuning the grating depth and the duty cycle. In this case a good compromise can be found with a depth of 50 nm and a duty cycle around 0.4; the achieved reflectivity approaches 80%, the out-of-band losses are kept under 0.25 dB and the reflection bandwidth is smaller than 1 nm. Furthermore no direct compensation effect between the two parameters has been found. Thus, an error in defining the duty cycle cannot be corrected by changing the depth of the perturbation. Even if at the end the same peak wavelength could be achieved, it would no longer be possible to fulfill at the same time the three requirements, thus coming up with a broader bandwidth and higher losses.

Since the duty cycle does not appear as critical as the depth d, it has been subsequently kept constant to a value of $DC = 0.4$ and the effect of the grating length has been analyzed. Fig. 2.16 shows how the peak reflectivity, out-of-band losses and the bandwidth react on a variation of d and L. Fig. 2.16(a) shows that the peak reflectivity can be increased either by increasing the etch depth or by making the grating longer; therefore it is possible to etch the grating shallower increasing at the same time its overall length. In this way the peak reflectivity is kept constant, but there is an evident advantage regarding the losses and the bandwidth, which can both be reduced with longer devices (see Fig. 2.16(b-c)). It should be noted that for very large etching depths, the losses limit the achievable peak reflectivities.

2.3 Fabrication

The grating design has been performed considering a two-dimensional approximation, as described in Sec. 2.2.1. In that case the waveguide is considered infinite in the lateral direction and the grating is produced with a surface corrugation. Transferring this idea to rib waveguides, three different implementation are possible, as depicted on Fig. 2.17. It would be possible to apply the periodic corrugation on the slab region close to the rib, on the top of the rib itself or both rib and slab. The first geometry permits to achieve a very weak interaction between the grating modulation and the optical field, and has to be preferred in the case of waveguides in submicron scale with a large evanescent field (see Fig. 2.13(c)). In this case a corrugation on the top of the waveguide would strongly interact with

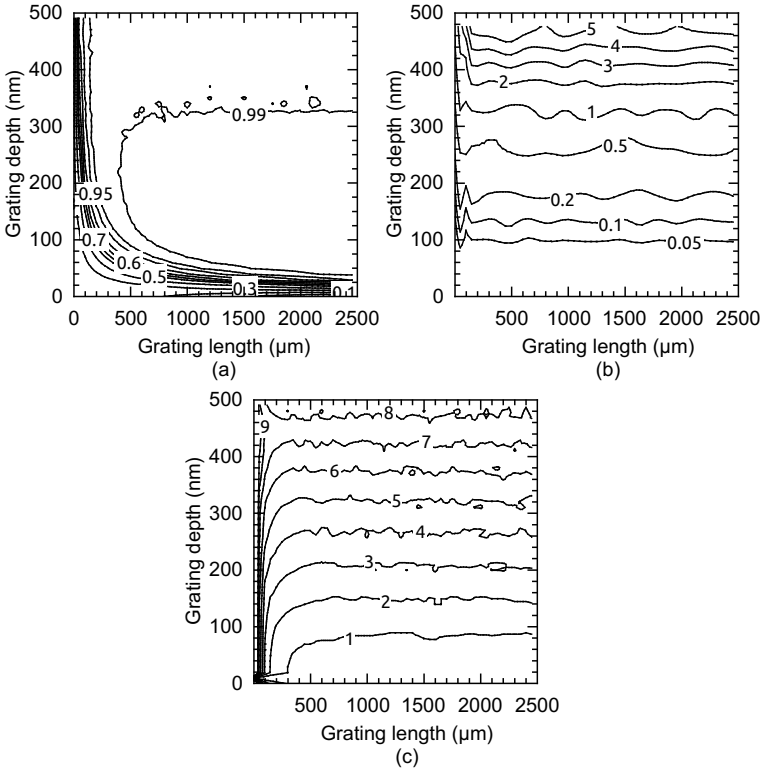

Figure 2.16: (a) Peak reflectivity, (b) loss in dB and (c) bandwidth in nm of a Bragg grating with period Λ = 225 nm and duty cycle DC = 0.3 as functions of the grating depth d and length L_g.

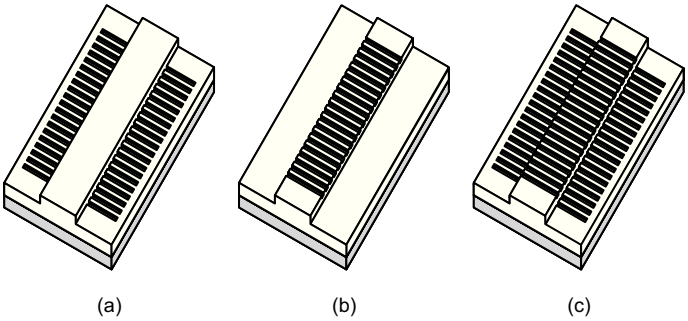

Figure 2.17: Schematic description of the fabrication steps with a double lithographic process. (a) Grating patterning on the plane substrate, (b) grating etching, (c) patterning of the waveguide rib and (d) rib etching.

the mode field, leading to a broad bandwidth. This solution requires to pattern and etch the grating after the waveguide fabrication, with the issue of performing a high precision lithography on a non planar substrate, and has not been considered within this work.

In the case of larger waveguides, like the considered rib waveguides with a guiding layer of 1.5 μm, the mode field is much more confined in the rib core and the corrugation on the top of the rib permits a good control of the strength. Such corrugation can be realized in a simpler way, producing the grating first on the planar substrate and subsequently etching the rib. According to the alignment tolerances of the used lithography, the grating can be realized with the same width of the rib (see Fig. 2.17(b)) or broader (see Fig. 2.17(c)). In the latter case the grating exhibits a stronger coupling coefficient, since the overlap between corrugation and mode field is larger (see Eq. 2.6).

Since the corrugation depth is shallower than the rib height, a double lithographic process with two different etching steps is required. Different variations of this method were demonstrated, either patterning first the grating and subsequently the rib [73–75], or first the waveguide and afterwards the grating using metal protection layers for the selective masking during the etching steps [57,76,77], achieving very promising results. In each case electron-beam lithography (EB) has been used for the grating patterning. EB lithography can achieve very high resolution, but only within a limited writing field (usually less than 1 mm^2). Writing fields can

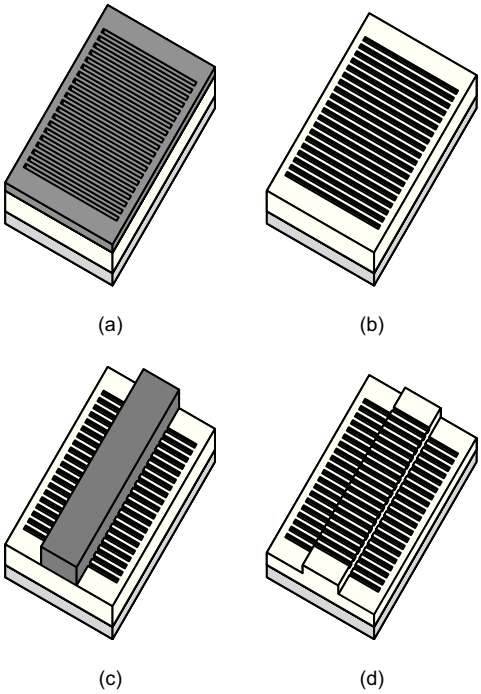

Figure 2.18: Schematic representation of three different possible implementations of Bragg gratings on rib waveguides: (a) corrugation of the side slab, (b) corrugation on the top of the rib and (c) corrugation on both rib top and side slab.

be stitched together to achieve bigger structures, but only at the price of additional stitching errors. The speed of high precision e-beam writing also makes the technique incompatible with wafer level processing.

For this reason an alternative fabrication approach has been investigated within this work, using Deep-UV 248 nm lithography (DUV). DUV lithography is a planar technology and is of widespread use in modern microelectronics fabrication. Therefore, this approach warrants the possibility for high throughput and thus low-cost fabrication of silicon waveguide Bragg gratings. Two different processes have been performed, one with EB lithography in cooperation with the Heinrich-Hertz-Institut (HHI) in Berlin as a state-of-the-art reference and one with DUV lithography at IHP

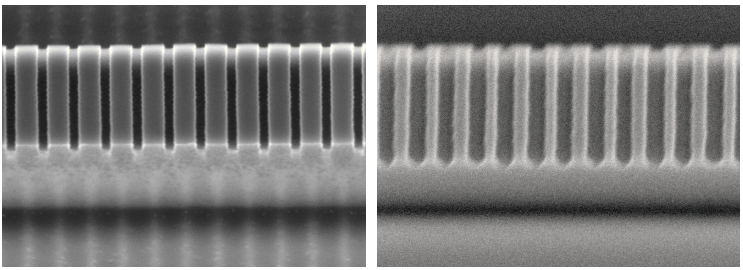

Figure 2.19: SEM micrograph of a Bragg grating patterned with (a) EB lithography and (b) DUV lithography.

Microelectronics in Frakfurt/Oder. In both cases the gratings have been patterned first on the plane substrate as shown on Fig. 2.18(a), since the lithography quality is strongly dependent on the surface morphology.

In the case of EB lithography a directly patterned 200 nm thick PMMA layer has been used as mask for the subsequent grating etching with an inductively coupled plasma (ICP) system and a continuous fluorine-based process (Fig. 2.18(b)). After removing the PMMA mask, patterned photoresist has been directly used as mask for the etching of the rib waveguide with a reactive ion etching system (RIE), avoiding the deposition of further protection materials (Fig. 2.18(c)). The obtained result is sketched on Fig. 2.18(d); to overcome the tolerances of the photolithographic tool, the grating has been patterned broader than the rib, with a consequent slight modulation of the slab at the side of the waveguide. This slab modulation is however smoothened by the rib etching step, as it can be observed on Fig. 2.19(a).

The fabrication based on DUV lithography follows the same step sequence of Fig. 2.18, however in both steps (a) and (c) a projection lithography has been used, which permits to reduce the structure roughness by a factor 4. After dry-etching the grating, the waveguide ribs have been formed by a second etch step. In both dry etch steps a poly-Si decoupled plasma source (DPS) etch chamber (Applied Materials) has been used, which warrants an etch depth variation lower than 10% on a 200 mm substrate. For the Bragg grating etch a simple one-step process using CF_4/Ar chemistry guarantees a uniform hard mask opening and a subsequent

etching into the underlying silicon to realize 50 nm deep grating trenches. In view of future integration aspects with other optical and electronic devices the final etch process for waveguide definition has been based on a well proven dry etch recipe used for shallow trench etching in 0.13 μm technology. The multi-step process starts with the etching of the antireflective coating layer, followed by the opening of the hard mask, consisting of a stack of different oxide and nitride layers. After in-situ ashing, the waveguide etching is carried out in chlorine-based plasma. Thanks to the overlay accuracy of 10 nm of the DUV exposer tool (NIKON NSR207D) it was not necessary to pattern broader gratings, whose width could be precisely matched to the rib width (see Fig. 2.19(b)) or even smaller. This property had a crucial importance for the device improvement described in Chapter 3.

After the processing and wafer dicing, the optical facets of the obtained chips have been polished and covered with a 208 nm thick Si_3N_4 antireflection coating to permit an easier coupling of the light into the waveguides. All fabricated waveguides exhibit an overall height of t = 1.5 μm, an etching depth of h = 0.5 μm and widths w varying between 1.0 and 1.8 μm. Different sorts of Bragg gratings have been fabricated, all with a depth d = 50 nm, period Λ varying between 224 nm and 227 nm, length L_g fixed at 800 μm for the EB patterned gratings (maximum size of the EB writing field) and varied between 100 and 1350 μm in the DUV case. In the case of the EB lithography it has been possible to achieve the optimal duty cycle DC = 0.4 adjusting the exposure doses, but in the case of the DUV lithography, where the grating dimensions are close to the resolution limit, only a duty cycle of DC = 0.5 could be achieved.

2.4 Characterization

2.4.1 Measurement setup

The measurement setup used for the characterization of the fabricated Bragg reflectors is shown on Fig. 2.20 and consists basically of a transmission measurement setup, where the single pass transmission through the silicon waveguide is measured. An efficient in- and out-coupling has been achieved using lensed fibers, which also allowed to avoid any direct contact with the waveguide facets. The analysis of the spectral behavior of the fabricated reflectors has been performed with a tunable laser source between 1500 and 1600 nm. A polarization controller allowed to set the polarization of the propagating light, while a 3-dB fiber coupler has been

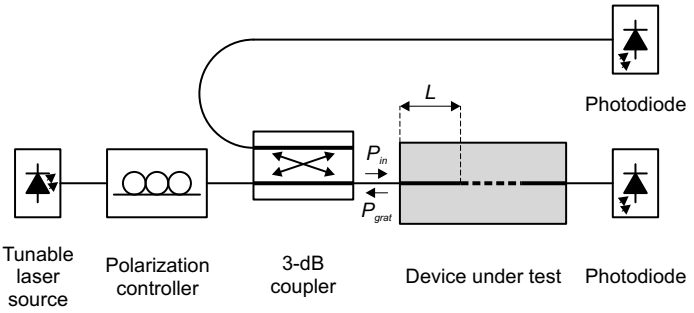

Figure 2.20: Scheme of the measurement setup used for the characterization of the fabricated Bragg gratings.

inserted before the in-coupling lensed fiber to separate the signal reflected from the Bragg reflector.

The grating transmissivity has been calculated as the ratio between the power transmitted by a waveguide with grating and the one transmitted by a common waveguide. MeasurementSetup For the calculation of the reflectivity R, as indicated in Eq. 2.44, the ratio between the power reflected by the grating and the input power, estimated by the transmission between the two lensed fibers without any waveguide has been considered. Furthermore the effect of the 3-dB coupler, as well as the coupling efficiency and the propagation loss have been taken into account. It follows:

$$R = \frac{P_{grat} - P_{wg}}{P_{in} K \eta^2 \exp(-2\alpha L)} \tag{2.44}$$

where P_{grat} is the reflected power measured from a waveguide with grating, P_{wg} the reflected power from a waveguide without grating, P_{in} the estimated input power, $K = 0.5$ the coupling ratio of the external 3-dB fiber coupler, η the coupling efficiency into the waveguide (0.47 estimated with a virtual cut-back measurement of straight waveguides exhibiting different lengths), α the linear propagation loss coefficient of the waveguide (0.2 dB/cm measured on a parallel straight waveguide) and L the distance between the in-coupling facet and the Bragg grating (see Fig. 2.20). The power P_{grat} and P_{wg} exhibit comparable values, while P_{in} is one order of magnitude larger. In Eq. 2.44 the effect of the resonator created between the reflector and the facet is neglected, because of the propagation loss in the rib waveguide and the presence of the antireflection coating.

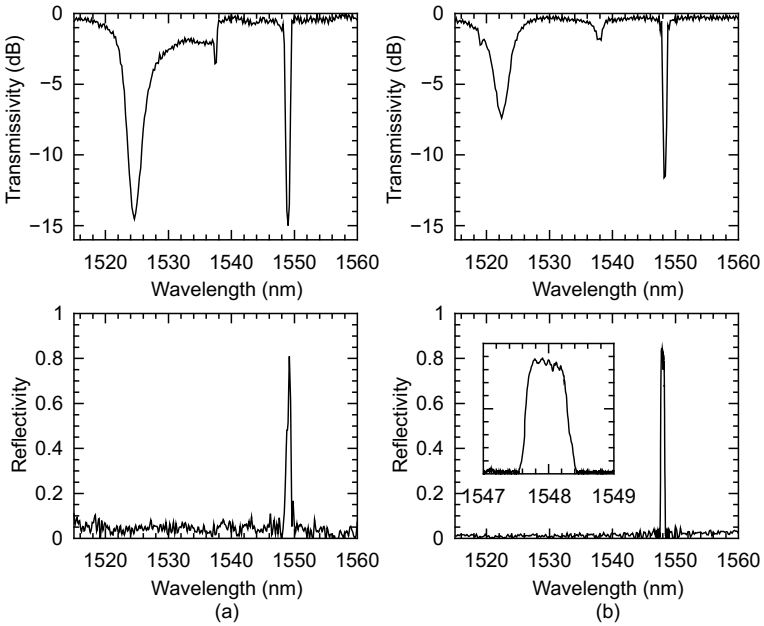

Figure 2.21: Measured reflectivity and transmissivity spectra for Bragg gratings patterned with (a) EB and (b) DUV lithography. TE polarization is considered. In the inset plot the reflection peak of the DUV patterned grating is shown.

2.4.2 Experimental results

In Fig. 2.21 the measured spectra for Bragg gratings fabricated with the two described processes are shown. It can be observed that in both cases a low loss is introduced, in the order of 0.5 dB. At the Bragg wavelength a reflectivity of 0.8 is achieved over a narrow bandwidth of 0.8 nm, corresponding to an extinction ratio in the transmission of 15 dB for the EB gratings and 12 dB for the DUV ones. At shorter wavelengths, around 1525 nm and 1540 nm, broad drops in the transmission spectrum are present, corresponding to a coupling to backward higher order modes, as already observed in the simulations (see Fig. 2.14). Since they cannot be guided in a single-mode rib waveguide, they are not back reflected and leak out. This

is confirmed by the absence of any reflected signal at these wavelengths. The slightly more pronounced extinction ratio and especially the short-wavelength drop in the case of the EB patterned gratings can be ascribed to the slab modulation discussed in Sec. 2.3, which increases the coupling to the backward travelling guided mode and to slab modes. It can be anyway observed that the DUV patterned Brag gratings exhibit a performance which is fully comparable to the ones of the state-of-the-art EB patterned gratings.

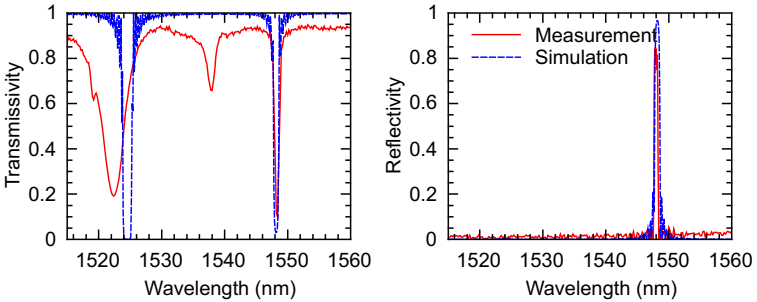

Figure 2.22: Comparison between computed and experimentally measured (a) transmission and (b) reflection spectra. The experimental data refer to a grating patterned with DUV lithography, with a period of Λ = 226 nm, a grating depth of d = 50 nm, a duty cycle DC = 0.5 and an overall length of L_g = 800 μm. The parameters of the simulated gratings are Λ = 225 nm, d = 50 nm, DC = 0.5 and L_g = 800 μm. TE polarization is considered. All spectra are in linear scale.

The comparison between the numerically computed and the measured spectra of the DUV patterned grating are shown in Fig. 2.22. It can be observed that around the Bragg wavelength at λ_B = 1549 nm the curves are in good agreement with each other, even if the reflection peak is slightly overestimated in the simulation. At shorter wavelengths the difference in the curve shape for the transmission spectrum is related to the nature of the modes involved: in the two dimensional waveguide considered in the simulation the grating couples energy between the forward propagating fundamental mode and a guided higher-order mode, while in the three-dimensional single-mode waveguide this coupling can occur only to leaky and radiating modes. The slightly higher overall loss in the measured transmission spectrum can be related to a possible sidewall roughness of the waveguide, not considered in a two-dimensional calculation. Another

difference between the calculated and measured structure is related to the grating period, which is Λ = 225 nm and Λ = 226 nm respectively. The rib waveguide exhibits a lower effective index compared to the two dimensional slab waveguide of the simulation, and in order to achieve a reflection at the same wavelength, a larger period is required.

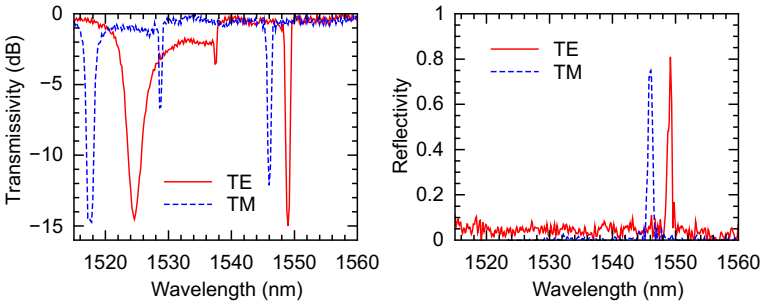

Figure 2.23: Reflectivity and transmissivity spectra for the TE (red continuous line) and the TM (dashed blue line) polarization. A grating patterned with EB lithography is considered, comparable results were measured on the DUV patterned ones.

The measured spectra for the TE and for the TM polarization are compared on Fig. 2.23. The reflected wavelength for the TM mode is shifted by 3 nm towards shorter wavelengths in respect to the TE reflection peak, indicating a waveguide birefringence of 7×10^{-3}. This value has been determined calculating the difference between the effective indices $\Delta n = |n_{eff,TE} - n_{eff,TM}|$, extracted from the measured curves considering the Bragg condition. Furthermore the extinction ratio and the peak reflectivity for the TM polarization are slightly lower than in the TE case, suggesting that the interaction between the TM optical field and the grating etched on the top of the waveguide rib is relatively weak compared to the TE polarization.

The influence of the grating length on the grating performances has been also investigated. As shown in Fig. 2.24, longer devices exhibit a larger reflectivity, which saturates around 0.9 for gratings longer than 1 mm. The introduced loss also increases, remaining however below 0.5 dB, but contradicting the theoretical expectation of constant loss for different grating lengths (see Fig. 2.16(b)). This could mean that the surface corrugation of the grating acts as roughness for the wavelengths outside the reflection bandwidth with consequent scattering.

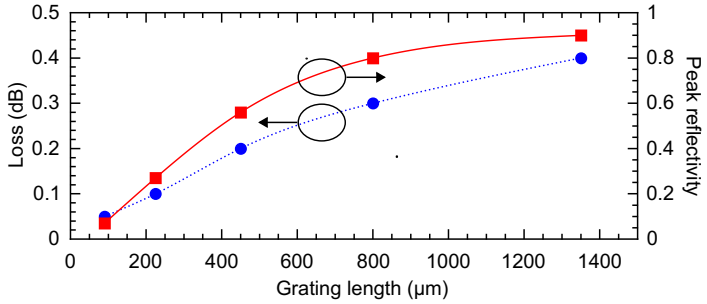

Figure 2.24: Dependence of the introduced loss and of the reflectivity peak on the grating length L_g. A grating patterned with DUV lithography is considered. TE polarization.

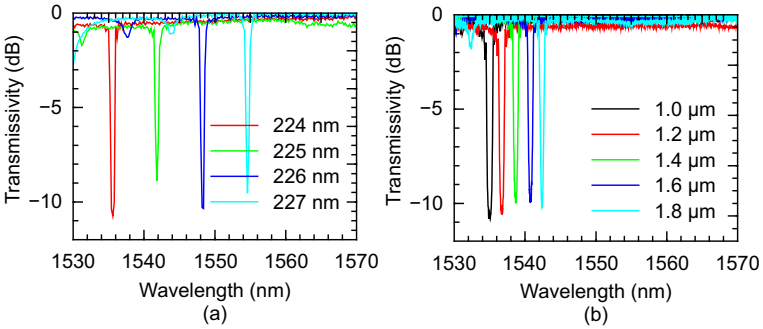

Figure 2.25: Measured transmission spectra of gratings with variation of (a) grating period and (b) waveguide width. A grating patterned with DUV lithography is considered. TE polarization.

Fig. 2.25 shows the sensitivity of the reflected wavelength to the factors which appear in the Bragg condition, i.e. the grating period and the waveguide effective index. Transmission spectra of gratings with different periods and patterned on waveguides with different rib widths have been measured. A shift of 6.3 nm was measured for a period difference of 1 nm. On the other hand a shift of 0.92 nm was observed for a increase of the

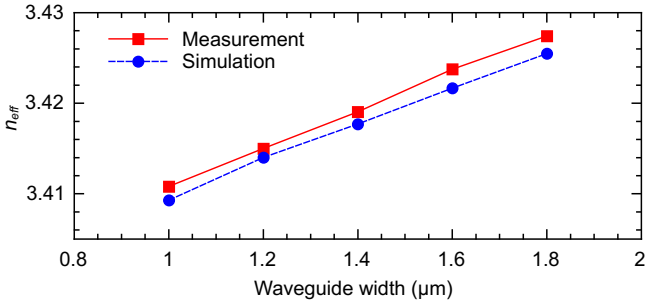

Figure 2.26: Comparison between the experimental and simulated dependence of the effective index on the waveguide width. A rib heigth of t *=1.5 μm and an etching depth* h *= 0.5 μm have been considered.*

rib width of 100 nm. This is due to a variation of the waveguide effective index, proportional to the waveguide width.

The effective indexes for the considered waveguide widths have been be experimentally extracted from the measured curves considering the Bragg condition and are plotted on Fig. 2.26. The experimental data are compared with values calculated with a finite difference mode solver [78]. It is possible to observe a good agreement between the experimental data and the theoretical expectations, besides a slight offset. In both cases a comparable proportionality factor γ can be determined:

$$\gamma = \frac{\Delta n_{eff}}{\Delta w} = 1.5 \times 10^{-5}\ \mathrm{nm}^{-1} \tag{2.45}$$

where Δn_{eff} is the variation of the effective index and Δw is the variation of the rib width.

The Bragg wavelength is therefore more sensitive to a variation of the grating period, whose definition requires hence a high precision.

3
Integrated dispersion compensator

3.1 Chirped gratings for dispersion compensation

In the previous chapter the principle of Bragg gratings and its implementation on integrated silicon rib waveguides has been introduced. The considered grating structures are defined as *uniform gratings* since all the grating parameters have been kept constant within the structure. However it is possible to modify some properties of the grating to achieve some specific effects. This is for example the case of chirped gratings, which have been anticipated in Sec. 1.3.1 and are treated within this chapter.

The general idea of a chirped grating is to vary the Bragg condition along the grating length in order to reflect different wavelengths at different positions along the z coordinate. These different wavelengths experience different propagating path lengths, with a consequent delay and hence dispersion. With a proper grating design, the chirp of an incoming signal can be arbitrarily manipulated. If the aim is the compensation of the first order dispersion, a linear chirp is required [32]. As a first approximation this means that the reflected wavelength increases linearly along the grating length L_g:

$$\lambda_B(z) = \lambda_{B,0} + F \cdot z \tag{3.1}$$

where $\lambda_{B,0}$ is the wavelength reflected at the beginning of the grating and F is the chirp coefficient. A generic wavelength λ within the interval $\lambda_{B,0}$ and $\lambda_{B,max} = \lambda_{B,0} + F \cdot L_g$ is reflected at the position:

$$z(\lambda) = \frac{\lambda - \lambda_{B,0}}{F}. \tag{3.2}$$

The delay difference experienced by this wavelength in relation to $\lambda_{B,0}$ is given by:

$$\tau(\lambda) = \frac{2n_g}{c} z(\lambda) = \frac{2n_g}{c} \cdot \frac{\lambda - \lambda_{B,0}}{F}. \tag{3.3}$$

From this delay, according to Eq. 1.8, it is possible to derive the dispersion generated by the grating:

$$D = \frac{\partial \tau}{\partial \lambda} = \frac{2n_g}{cF}. \tag{3.4}$$

Properly choosing the chirp factor F the chromatic dispersion introduced by the grating can be tuned in such a way to compensate the chromatic dispersion accumulated by the incoming signal.

3.2 Integrated drop-filter for dispersion compensation

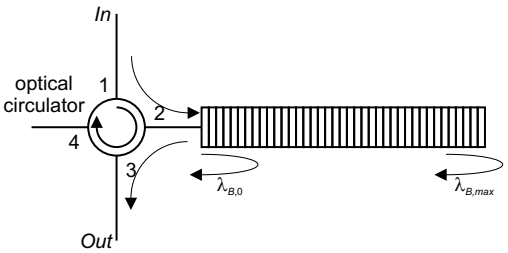

Figure 3.1: Connection of a fiber Bragg grating with an optical circulator for the extraction of the reflected signal.

Chirped Bragg gratings for dispersion compensation are widely used in fiber optics. Since they operate in reflection, it is necessary to entirely separate the compensated signal and forward it to the next fiber span or detecting device. This is normally achieved with the use of optical circulators, as sketched on Fig. 3.1, which introduce losses lower than 1 dB. The direct translation of this method in integrated waveguides is complicated. Efforts have been made to integrate an optical circulator [79–82]. The principle is based on the non-reciprocal Mach-Zehnder interferometer depicted on Fig. 3.2, where half-wave plates and Faraday rotators are placed on both interferometer arms. The slow axes of the half-wave plates HW_1 and HW_2 is set at respective angles of -22.5° and 22.5° in relation to the axis in the transverse plane.

In direction A, it is assumed that the light propagating in the upper and lower waveguide arm have the same polarization at position I, which correspond to the TM and TE modes. Then, the light propagating in the upper waveguide arm passes through HW_1 and the Faraday rotator FR_1 while

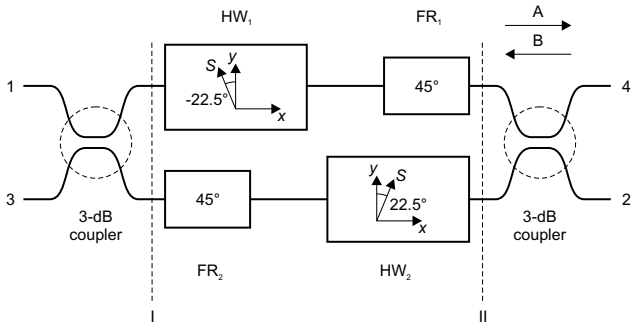

Figure 3.2: Principle of an integrated optical circulator based on a non-reciprocal Mach-Zehnder interferometer [79].

the light propagating in the lower waveguide arm passes through FR_2 and HW_2. Consequently, the light propagating in both waveguide arms still have the same polarization at position II and are in phase. In direction B, we assume that the light propagating in upper and lower waveguide arms also have the same and polarization at position II. Then, the light propagating in the upper waveguide arm passes through FR_1 and HW_1 while the light propagating in the lower waveguide arm passes through HW_2 and FR_2. However, the light propagating in the upper and lower arms have opposite polarization directions at position I as a result of nonreciprocal rotation. Consequently, the phases of the light propagating in the two arms in direction B differ by 180°. Since 3-dB couplers switch their output arm according to the phase difference between the light sources propagating in the two arms, the device acts as a circulator, i.e., a wave travels from port 1 to port 2, port 2 to port 3, port 3 to port 4, and port 4 to port 1 in Fig. 3.2.

The practical implementation of the device is not trivial and requires several additional fabrication steps and the combination of different materials. The half wave plates can be obtained with hybrid integration of polyimide or quartz plates into the substrate [79, 80] or etching a notch in the waveguide [81,82]. The Faraday rotator has to be realized with external materials like (La,Ga):YIG which react to an externally applied magnetic field. Fabricated devices showed introduced loss around 3.5 dB and an extinction about 29.8 dB.

A solution which permits to avoid the integration of the optical circu-

lator and hence further fabrication steps was theoretically proposed [83] and is considered within this work. It is based on a drop-filter architecture, which exploits an intrinsic property of 3-dB couplers. Here we consider the specific case of MMI couplers [84] without lack of generality (see Fig. 3.3), since they are easier to fabricate and more compact than directional couplers [85]. An incoming wave from port *a* is guided to a broad multimode region, where several modes with different propagation velocities are generated. Properly choosing the length of this multimode region the different mode interfere constructively on two points, corresponding to the output waveguides (ports *b* and *c*).

Referring to Fig. 3.3, the device can be described with the help of scattering matrices:

$$\begin{pmatrix} B_a \\ B_b \\ B_c \\ B_d \end{pmatrix} = \mathbf{S}_{coupler} \cdot \begin{pmatrix} A_a \\ A_b \\ A_c \\ A_d \end{pmatrix} \tag{3.5}$$

with

$$\mathbf{S}_{coupler} = \begin{pmatrix} 0 & S_{ab} & S_{ac} & 0 \\ S_{ab} & 0 & 0 & S_{ac} \\ S_{ac} & 0 & 0 & S_{ab} \\ 0 & S_{ac} & S_{ab} & 0 \end{pmatrix} = \begin{pmatrix} 0 & \frac{1}{\sqrt{2}} & j\frac{1}{\sqrt{2}} & 0 \\ \frac{1}{\sqrt{2}} & 0 & 0 & j\frac{1}{\sqrt{2}} \\ j\frac{1}{\sqrt{2}} & 0 & 0 & \frac{1}{\sqrt{2}} \\ 0 & j\frac{1}{\sqrt{2}} & \frac{1}{\sqrt{2}} & 0 \end{pmatrix} \tag{3.6}$$

Considering an input signal at port *a*, the output signals at ports *b* and *c* exhibit an amplitude which is half of the input one and a phase difference of 90° between each other. This phase difference permits to replace the optical circulator with a 3-dB coupler and a second grating.

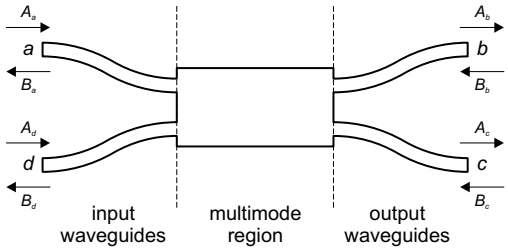

Figure 3.3: Principle of a MMI coupler.

The principle of the presented drop-filter is depicted in Fig. 3.4. It is based on two pairs of identical Bragg gratings connected by two 3-dB MMI

couplers. The input signal is coupled into waveguide *In* and is equally split to the gates *b* and *c* of the MMI coupler M_1. Between the two signal portions a phase difference of 90° occurs. They impinge on the first pair of identical Bragg gratings G_1 and are back reflected to the coupler. Because of a further phase shift, the two parts of the signal interfere constructively on gate *d* and destructively on *a*. The entire signal is therefore guided to the input *e* of the MMI coupler M_2. After being reflected by a second pair of identical Bragg gratings G_2, the signal is fully transmitted to the output waveguide Out_3. Since the gratings are wavelength selective, only one channel is reflected by the grating pairs and appears at the output Out_3. All other wavelengths will be transmitted and appear at the output ports Out_1 and Out_2.

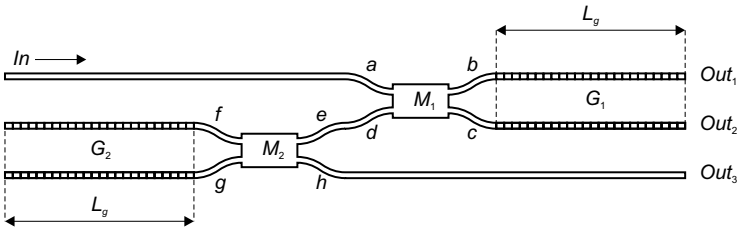

Figure 3.4: Scheme of the integrated Drop-filter for dispersion compensation.

Two basic requirements have to be fulfilled to achieve the expected behavior. First of all the MMI couplers have to exhibit a high symmetry in the power splitting, to prevent that part of the signal is back reflected to the input. Second, the alignment precision of the grating pairs has to be kept as high as possible. Every minimal misalignment would introduce a further phase difference between the two signals reflected by the grating, invalidating the full constructive interference at the output of the MMI coupler. This is warranted if the misalignment is kept far below $\lambda/4n$, i.e. one fourth of the wavelength in the material.

3.3 Grating design

3.3.1 Chirp implementation

The aim is to achieve a spatial distribution of the Bragg condition along the grating, in order to reflect different wavelengths at different positions.

This can be achieved linearly varying the grating period, as introduced in Sec. 1.3.1.

Assuming a linear dependence of the group delay on the wavelength across the grating bandwidth, the dispersion can be expressed as:

$$D = \frac{\partial \tau}{\partial \lambda} \approx \frac{\Delta \tau}{\Delta \lambda}. \tag{3.7}$$

The group delay difference $\Delta\tau$ can be approximated by the propagation time difference between the wavelength reflected in the front and the wavelength reflected and the end of the grating:

$$\Delta \tau = \frac{2 n_g L_g}{c} \tag{3.8}$$

where L_g is the grating length and n_g the group index. The compensation of a residual dispersion in the order of 100 ps/nm over a bandwidth of 1 1nm would require a grating length of 4.3 mm in silicon waveguides. The bandwidth $\Delta\lambda$ can be approximated as:

$$\Delta \lambda = \lambda_{B,L_g} - \lambda_{B,0} \tag{3.9}$$

where $\lambda_{B,0}$ and λ_{B,L_g} are the wavelengths reflected at the front and at the end of the grating respectively.

Considering a linear variation of the grating period (see Fig. 3.5(a)):

$$\Lambda(z) = \Lambda_0 + C_\Lambda \cdot z \tag{3.10}$$

where Λ_0 is the period in the front part of the grating and C_Λ is the period chirp coefficient, a period variation of $\Delta\Lambda = C_\Lambda \cdot L_g$ over L_g is achieved. Considering the expression of the Bragg condition (Eq. 2.22) the grating bandwidth can be hence rewritten as:

$$\Delta \lambda = 2 n_{\text{eff}} C_\Lambda L_g. \tag{3.11}$$

Considering as target a bandwidth of 1 nm to fit to the signal bandwidth of a 100 GHz WDM channel and the previously calculated grating length (see Eq. 3.8), a period chirp factor of C_Λ = 33.2 pm/mm is obtained. This means that a period variation of 142 pm from the beginning to the end of the grating and hence a difference of 7.5 fm between two adjacent grating lines would be necessary. This dimensions go far beyond the limits of the resolution of the DUV lithography.

As discussed in Sec. 2.4.2 the reflected wavelength depends also on the effective index of the waveguide and can be tuned varying the waveguide

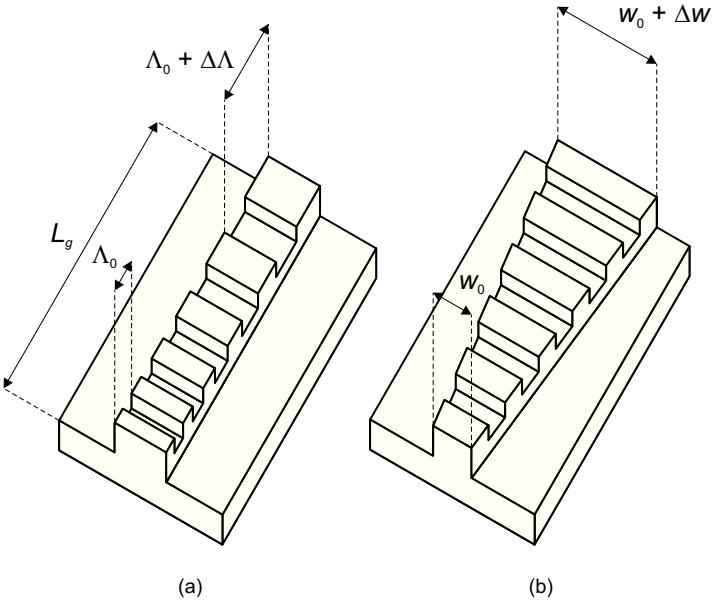

Figure 3.5: Implementation of the chirp: (a) linear variation of the period from Λ_0 to $\Lambda_0 + \Delta\Lambda$, (b) linear variation of the rib width from w_0 to $w_0 + \Delta w$.

width. The chirp can be therefore implemented keeping the grating period constant and linearly increasing the waveguide width (see Fig. 3.5(b)). The bandwidth can be hence expressed as:

$$\Delta\lambda = 2\Delta n_{eff}\Lambda \tag{3.12}$$

Considering the linear dependence of the effective index on the waveguide width extracted from Fig. 2.25 one obtains:

$$\Delta\lambda = 2\Lambda\gamma\Delta w \tag{3.13}$$

where Δw is the waveguide width variation and $\gamma = 1.2 \times 10^{-5}$ nm^{-1} is the coefficient of $n_{eff}(w)$ (see Eq. 2.45). In order to fulfill the previously given requirements, a width variation of $\Delta w = 143.6$ nm is achieved, corresponding to a taper coefficient $C_w = \Delta w / L_g = 3.34 \times 10^4$ pm/mm. This value is 1000 times larger than C_Λ and makes the implementation of the chirp via waveguide taper much easier to fabricate than varying the grating period.

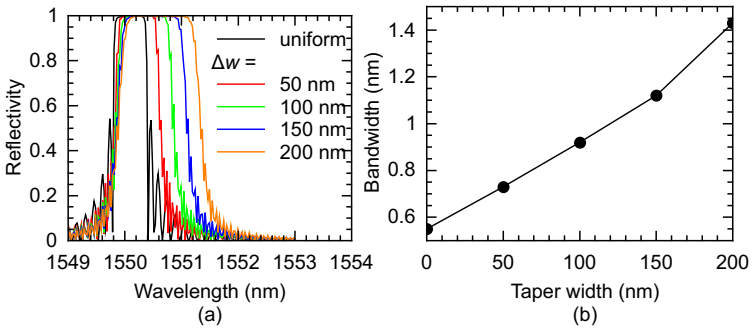

Figure 3.6: (a) Calculated reflectivity spectra of tapered gratings for different values of Δw. (b) Reflection bandwidth of tapered gratings as function of the taper width Δw.

3.3.2 Taper design

For a more precise grating design, numerical simulations of the grating structure are required. However the modelling of tapered gratings is not trivial. At every waveguide discontinuity the waveguide profile changes and a new mode set has to be calculated, and furthermore a three dimensional computation is required, which permits to take into account the rib width. On the other hand the modelling of chirped gratings with period variation does not exhibit any complication compared to the uniform ones. Since the cross section does not change, only two scattering matrices are required, and the period change is translated into the propagation matrices (see Eq. 2.38). It is hence evident that it is more convenient to numerically model two dimensional gratings with a linear variation of the period and translate the results to a tapered grating, considering the relation:

$$\Delta w = \frac{n_{eff}}{\Lambda_0 \gamma} \Delta \Lambda \tag{3.14}$$

where Λ_0 is the starting period.

In Fig. 3.6(a) the calculated reflectivity spectra of different tapered gratings are shown. Gratings with period Λ_0 = 225 nm, depth d = 50 nm, duty cycle DC = 0.5 and length L_g =5 mm have been considered. It can be observed that increasing the end width of the taper a broadening of the grating bandwidth occurs. In particular, the short wavelength limit remains constant, since it is defined by the start waveguide width (or start

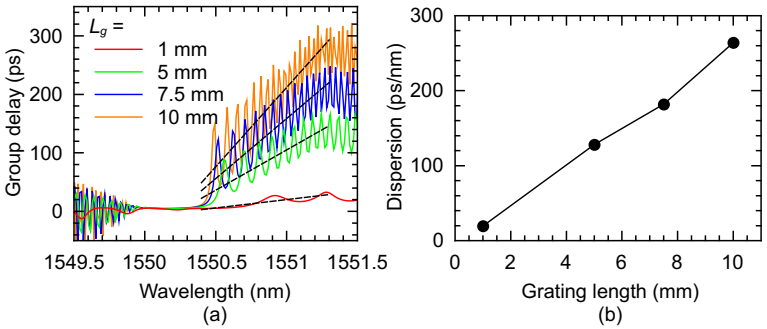

Figure 3.7: (a) Calculated group delay curves of tapered grating with for different values of the length L_g. The taper width is Δw = 140 nm. (b) Dispersion of the tapered gratings as function the grating length L_g.

grating period, in the case of this numerical simulations), while the end wavelength varies linearly increasing the taper width. Tuning the taper width is hence possible to precisely tune the grating bandwidth considering their linear dependence (see Fig. 3.6(b)); the target bandwidth of 1 nm is achieved with a width variation Δw around 120 nm, showing that the calculation of Sec. 3.3.1 is slightly overestimated.

The effect of the grating length has also been considered. The dependence of the group delay on the wavelength has been computed for different grating lengths deriving the phase $\phi(\lambda)$ of the reflected signal according to Eq. 1.7. The obtained curves are shown on Fig. 3.7(a). It is possible to observe that after flat region, corresponding to the wavelengths reflected in the front part of the grating, a linear increase of the group delay is present. A strong ripple overlaps, with an amplitude and a frequency which increase for longer gratings. This ripple will be discussed in more detail in the next section. Fitting linearly the group delay curve it is possible to determine the dispersion added by the grating. The values of the dispersion for different grating lengths are shown on Fig. 3.7(b). As already expected from the rough estimations of Sec. 3.3.1 the grating dispersion depends linearly on the grating length, reaching values of 260 ps/nm for gratings 1 cm long.

3.4 Reduction of the group delay ripple

3.4.1 Group delay ripple

In the previous section the presence of the group delay ripple has been observed (see Fig. 3.7(a)). It is necessary to understand how this ripple is generated, since its elimination is essential for a proper dispersion compensation. Each deviation from the linear dependence of the group delay on the wavelength corresponds to an incomplete regeneration of the dispersed pulse with a consequent increase of the bit error rate (BER).

To understand how this ripple is generated it is useful to assume that the grating modulation is weak and apply the coupled mode theory. Applying a chirp, the grating becomes nonuniform and the coupled equations Eq. 2.5 has to be rewritten. The variation of the period along the structure produces an additional phase shift to the spatial frequency of the grating k_g, which is $k_g = 2\pi/\Lambda$ in the uniform case. Considering the chirped case described in Eq. 3.10 the spatial frequency becomes:

$$k_g = \frac{2\pi}{\Lambda_0 + C_\Lambda z}. \tag{3.15}$$

The phase of the grating $\phi_g(z)$ can be therefore calculated integrating k_g [57]:

$$\phi_g(z) = \int_0^z k_g(z')dz' = \int_0^z \frac{2\pi}{\Lambda_0 + C_\Lambda z'} dz' = \frac{2\pi}{C_\Lambda} \ln\left(1 + \frac{C_\Lambda z}{\Lambda_0}\right). \tag{3.16}$$

Considering that $C_\Lambda z/\Lambda$ is negligible compared to 1, the obtained expression can be simplified with a Taylor series:

$$\phi_g(z) = \frac{2\pi}{\Lambda_0} z - \frac{\pi C_\Lambda}{\Lambda_0^2} z^2. \tag{3.17}$$

The first term corresponds to the phase of the uniform grating without chirp, while the second quadratic term is the phase added by the chirp. The coupled equations Eq. 2.8 can be hence rewritten as:

$$\frac{d}{dz}\begin{pmatrix} B(z) \\ A(z) \end{pmatrix} = \begin{pmatrix} -\delta(z) & \kappa(z) \\ \kappa(z)^* & j\delta(z) \end{pmatrix} \cdot \begin{pmatrix} B(z) \\ A(z) \end{pmatrix} \tag{3.18}$$

where

$$\begin{aligned} \delta(z) &= \beta(z) - \frac{\pi}{\Lambda_0} \\ \kappa(z) &= \kappa_0(z) \cdot \exp\left[j\left(\frac{2\pi}{\Lambda_0} z - \phi_g(z)\right)\right]. \end{aligned} \tag{3.19}$$

Substituting 3.17 into the previous equation, it is possible to observe that the final effect of the chirp is to add a quadratic slow variation term in the phase of the coupling coefficient:

$$\kappa(z) = \kappa_0(z) \cdot \exp\left(j\frac{\pi C_\Lambda}{\Lambda_0^2}z^2\right). \tag{3.20}$$

Assuming that the grating exhibits a constant strength (no variation of the duty cycle DC or depth d), the coupling constant $\kappa_0(z)$ is a rectangular function with basis L_g. Assuming its amplitude small, the approximation of a weak grating is fulfilled and the grating reflectivity can be calculated from the Fourier transformation of $\kappa(z)$:

$$r(\delta) \approx \int_{-\infty}^{+\infty} \kappa(z')\exp(-j\delta z')dz'. \tag{3.21}$$

In this case the the Fourier transformation of the product of two functions has to be calculated:

$$r(\delta) \approx \int_{-\infty}^{+\infty} \kappa_0(z') \cdot \exp\left(j\frac{\pi C_\Lambda}{\Lambda_0^2}z'^2\right) \cdot \exp(-j\delta z')dz' \tag{3.22}$$

Defining

$$g(z) = \exp\left(j\frac{\pi C_\Lambda}{\Lambda_0^2}z^2\right) \tag{3.23}$$

the reflection becomes

$$r(\delta) \approx \mathcal{F}\left(\kappa_0(z) \cdot g(z)\right) = \mathcal{F}\left(\kappa_0(z)\right) * \mathcal{F}\left(g(z)\right). \tag{3.24}$$

The grating reflectivity is therefore the result of the convolution between the reflectivity of the uniform grating with period Λ_0 and a function with quadratic phase.

In Fig. 3.8(a) the normalized amplitude and phase of the reflectivity of a uniform grating, obtained as Fourier transformation of $\kappa_0(z)$ are shown. It is possible to observe that the phase exhibits a saw-tooth profile, with a linear rise over the the lobes of the reflection spectrum (π phase shift at every lobe). This reflection is convolved with $g(z)$ (see Fig. 3.8(b)), which exhibits a unitary amplitude and a quadratic phase profile. The result is a spectrum with a broader bandwidth and a quadratic phase profile (see Fig. 3.8(c)). On this phase profile a fast modulation overlaps, as shown on

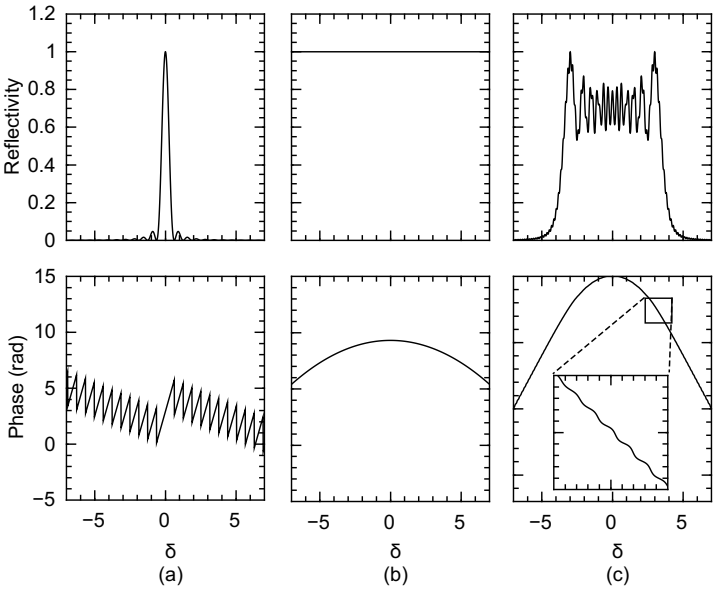

Figure 3.8: Amplitude and phase of (a) $\mathcal{F}(\kappa_0(z))$, (b) $\mathcal{F}\left(g(z)\right)$ and (c) $\mathcal{F}(\kappa_0(z))*\mathcal{F}\left(g(z)\right)$. The calculations have been performed with the assumption of a weak grating, with a length of 5 mm and a a period chirp coefficient of C_Λ 700 nm/mm.

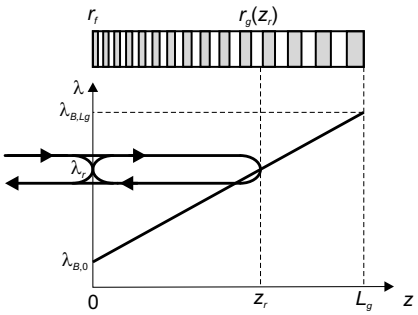

Figure 3.9: Description of the chirped grating as a Fabry-Perot resonator with varying length.

the plot inset. Differentiating this phase profile over the frequency a linear group delay with overlapping oscillation is obtained.

These oscillations can be considered as the result of interference. The chirped grating can be describes as a Fabry-Perot resonator with varying length, as depicted on Fig. 3.9. The input wave with wavelength λ_r comprised between $\lambda_{B,0}$ and λ_{B,L_g} is reflected at at position z_r with a reflection coefficient $r_g(z_r)$, ideally equal to 1. The abrupt transition between plain waveguide and surface corrugation at the beginning of the grating constitutes a discontinuity in $\kappa(z)$, which leads to a parasitic front broadband reflection r_f [86]. This leads to an asymmetric Fabry-Perot resonator, with a length which varies with the input wavelength. The reflection of the Fabry-Perot resonator is [87]:

$$r_{FP} = \frac{r_f - r_g(z_r)\exp\left(2j\beta_r z_r\right) + 2r_f r_g(z_r)\exp\left(2j\beta_r z_r\right)}{1 - r_f r_g(z_r)\exp\left(2j\beta_r z_r\right)} \tag{3.25}$$

where β_r is the propagation constant at the wavelength λ_r. Differentiating the phase of r_{FP} according to Eq. 1.7 the group delay is obtained.

In Fig. 3.10(a) the group delay for resonators with three different lengths are shown. For the calculations a grating reflectivity of $r_g(z_r) = 1$ has been considered, while the front reflectivity has been set to $r_f = 0.1$. This value has been extracted from the curves of Fig. 3.7(a). The average value of the group delay increases with the resonator length and is due to the increasing propagation path (see Eq. 3.8). The overlapping ripple due to the Fabry-Perot effect exhibits a period which is inversely proportional to the resonator length and an amplitude which is larger for longer cavities. These relations are summarized in Fig. 3.10(b). Since each wavelength within the reflection bandwidth is reflected at a different position, the group delay ripple results to be linearly chirped, with a decreasing period for wavelengths reflected in the back grating sections.

Several investigations on the effect of the group delay ripple on the data transmission have been performed in the past [88–90], showing that an input pulse $a(t)$ suffers a distortion induced by the group delay ripple which can be approximated as [90]:

$$\begin{aligned} b(t) \approx a(t) + \frac{\tau_{pp} f_p}{4} \cdot \Bigg\{ & a\left(t + \frac{1}{f_p}\right)\exp\left[j\left(\frac{\pi}{2} + \phi_0\right)\right] + \\ & + a\left(t - \frac{1}{f_p}\right)\exp\left[j\left(\frac{\pi}{2} - \phi_0\right)\right]\Bigg\} \end{aligned} \tag{3.26}$$

where τ_{pp} and f_p are the peak-to-peak and period in frequency of the group delay ripple respectively, and ϕ_0 is a phase related to the offset between the

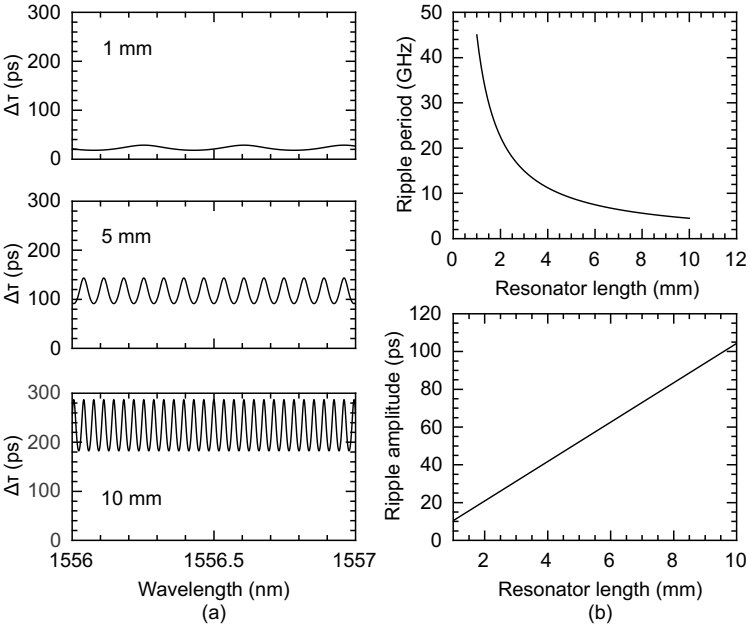

Figure 3.10: (a) Group delay curves of Fabry-Perot resonators for three different cavity lengths: 1 mm, 5 mm and 10 mm. (b) Calculated dependence of the ripple period and amplitude on the resonator length.

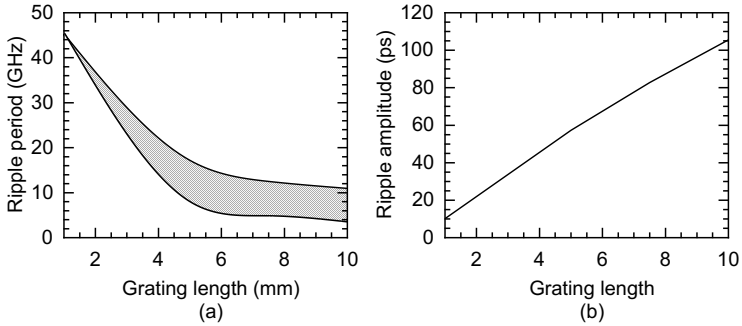

Figure 3.11: (a) Period in frequency and (b) amplitude of the group delay ripple as function of the grating length L_g.

signal frequency and the nearest ripple peak. The distorted pulse consists of the original pulse $a(t)$ and two scattered pulses with delays $\pm 1/f_p$ and amplitude $\tau_{pp} f_p/4$. If the ripple period is lower than the bit rate, the amplitude of the scattered pulses is also low, resulting in a small intersymbol interference (ISI). On the other hand, if the ripple period is larger than the bit rate, the time offset between the original pulse and the scattered pulses becomes lower than the bit period, and a low ISI results. The worst case occurs when the bit rate and the ripple period are close to each other, since the scattered pulses with non negligible amplitude are located around the center of the neighboring bits, resulting in a large ISI.

On Fig. 3.11 the period and the amplitude of the group delay ripple extracted from the computed curves of Fig. 3.7(a) are shown. The obtained curves exhibit a good agreement with the theoretical expectations of the Fabry-Perot analysis (see Fig. 3.10). Whilst the ripple amplitude remains constant over the reflection bandwidth, the period decreases from the shorter to the longer wavelengths, defining a ripple bandwidth [91]. Pulse streams with bit rate matching this bandwidth would suffer from a strong ISI as previously discussed. Considering a grating length of 1 cm, a ripple amplitude of 105 ps occurs with a frequency between 5 and 10 GHz. Considering a bit rate of 5 Gbit/s, scattered pulses with an amplitude of 30% of the input ones are generated, with a consequent strong ISI. It is evident that the reduction on the group delay ripple is inevitable.

3.4.2 Grating apodization

A cancellation of the group delay ripple is achieved removing its causes, hence suppressing the parasitic reflection r_f at the grating ends. This can be achieved by appropriately tapering the coupling constant κ along the grating length [92,93]; this procedure is called *apodization*. The rectangular shape of $\kappa(z)$ has to be replaced with a function which decreases smoothly to zero at the grating ends. This permits to reduce the effect of the reflectivity r_f in the Fabry-Perot resonator and reduce the effect of the ripple.

The idea is therefore to vary the grating strength symmetrically along the grating, avoiding the abrupt beginning and ending of the index modulation. This is achieved in fiber gratings varying the intensity of the UV light used for the grating patterning in the photosensitive fiber core [94,95]. Since this is not possible in integrated waveguides, the shape of the grating openings has to be modified, to vary the strength of the interaction between the optical field and the surface corrugation. Either the grating depth or the duty cycle have a direct influence on the grating strength, as observed on Fig. 2.15. However a variation of the grating depth would require several etching steps with selective masking, with consequent high fabrication complexity and a larger number of possible errors which could occur and sum during the realization steps. Is therefore evident that an apodization via duty cycle variation is a preferred method, since it is realized with the same process of a uniform grating, and has already been successfully applied in SiON planar gratings [96].

The effect of different apodization profiles on the reflection and dispersion properties of linearly chirped gratings has been investigated. The parameters of interest upon which the comparison is based are the mean dispersion D_m, the peak to peak group delay ripple, the ripple period and the FWHM bandwidth. The mean dispersion is given by the slope of the best-fitted straight line of $\tau(\lambda)$. The maximal reflectivity (maximal grating strength) occurs with a duty cycle of 0.42 for a grating depth of 50 nm. Hence the duty cycle has been varied with different profiles from 0 to 0.42. The different analyzed duty cycle apodization profiles are plotted of Fig. 3.12 and are [97]:

1. sine profile

$$DC(z) = 0.42 \cdot \sin\left(\frac{\pi z}{L}\right), \quad 0 \leq z \leq L$$

2. positive-tanh profile

$$DC(z) = 0.42 \cdot \tanh\left[\frac{2bz}{L}\right], \quad b = 4, \quad 0 \leq z \leq \frac{L}{2}$$
$$= 0.42 \cdot \tanh\left[\frac{2b(L-z)}{L}\right], \quad b = 4, \quad \frac{L}{2} \leq z \leq L$$

3. raised sine profile

$$DC(z) = 0.42 \cdot \sin^2\left(\frac{\pi z}{L}\right), \quad 0 \leq z \leq L$$

4. sinc profile

$$DC(z) = 0.42 \cdot \frac{\sin(x)}{x}, \quad x = \frac{2\pi\left(z - \frac{L}{2}\right)}{0}, \quad 0 \leq z \leq L.$$

For the unapodized case $DC(z) = 0.42$.

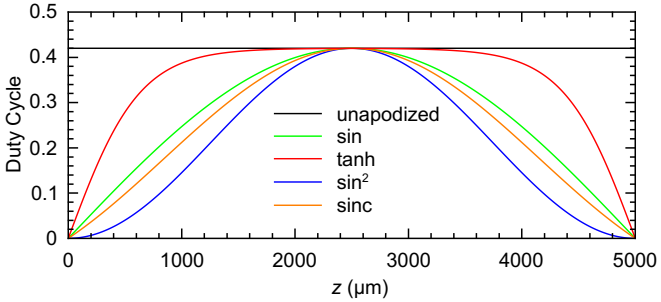

Figure 3.12: Considered apodization profiles. The overall grating length is kept L_g 5 mm.

On Fig. 3.13 the computed reflectivity spectra and group delay curves for the different apodization profiles are plotted. It is shown that profiles with a higher truncation level (tanh → sin → sinc → $\sin^2$) result in a narrower bandwidth and lower group delay ripple. This is expected, since a higher reduction of the duty cycle at the ends of the grating correspond to a suppression of the strength at the wavelengths reflected in the front and in the rear grating section.

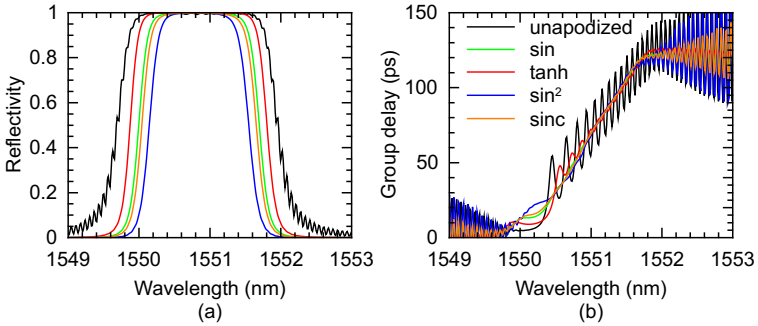

Figure 3.13: (a) Reflection spectra and (b) group delay curves of chirped gratings with different apodization profiles.

Profile	D_m (ps/nm)	$\Delta\lambda_{3dB}$ (nm)	τ_{pp} (ps)	f_p (GHz)	$\tau_{pp} \cdot f_p$
unapodized	67.3	2.3	25.4	24.9	0.61
sin	74.9	1.7	1.8	29.7	0.05
tanh	71.1	1.9	8.2	20.3	0.17
sinc	77.6	1.4	3.8	23.4	0.09
$\sin^2$	75.9	1.6	1.9	28.7	0.06

Table 3.1: Performance comparison of chirped gratings with different apodization profiles.

The values for the mean dispersion, the peak to peak group delay ripple, ripple period and bandwidth are summarized on Table 3.1. The overall group delay difference $\Delta\tau$ = 130 ps does not change for the different apodization profiles, since it depends on the overall grating length. However apodization profiles with a higher truncation level exhibit a narrower bandwidth over which this $\Delta\tau$ occurs and hence a higher mean dispersion. The group delay ripple which appears to be 25 ps for the unapodized case, can be reduced up to a value of 1.8 ps apodizing with a sine-profile. On the other side the ripple period does not change significantly for the different profiles. The critical factor for the ISI is the product $\tau_{pp} f_p$, which is lower for the grating apodized with a sine and a squared sine profile. The sine profile has been chosen for the chirp implementation.

The implementation of the designed apodized gratings with variation of the duty cycle can be achieved only using a high precision electron-beam lithography, which permits to control the width of each grating line

with the exposure doses. However this technology is not compatible with the purpose of fabrication of gratings for dispersion compensation, where a length larger than 800 μm is required. The device length is not an issue for fabrication processes based on DUV lithography, which introduces however limitations on the duty cycle, limited to a value of 0.5 (see Sec. 2.3). It is therefore intuitive to translate the variation of the length of the grating openings in a variation of their width. In this way not only the period, but also the duty cycle is kept constant, while the width of the grating is varied from a minimal value defined by the lithography resolution to the width of the rib in the middle of the taper using the chosen apodization profile, as depicted on Fig. 3.14(a).

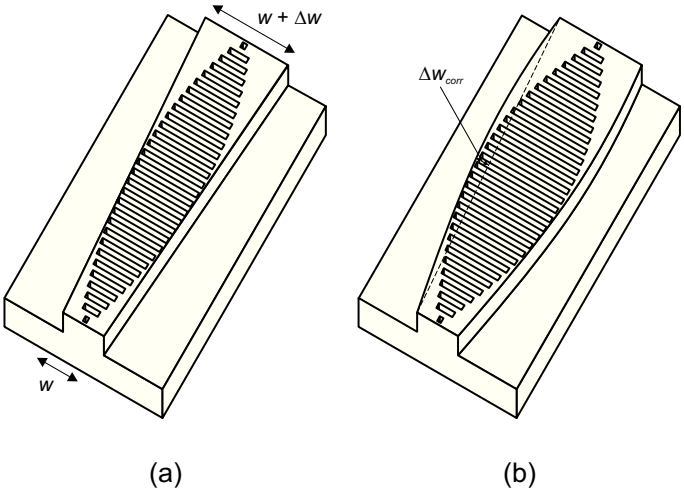

Figure 3.14: Scheme of apodization of a tapered grating with variation of the width of the trenches.

In the ideal case the effective index should increase linearly along the grating to implement the desired chirp. However the variation of width of the grating openings leads to a variation of the effective index. An additional chirp is hence produced along the grating with a profile, which is analogous to the apodization one. In the middle part of the grating, where the openings exhibit the maximal width, the effective index is lower than in the regions where the openings are narrower.

Calculations with [78] showed that the actual effective index exhibits a

deviation from the ideal case of about 2×10^{-4} in the middle of the grating. This means that the wavelength reflected in this point is 90 pm shorter than expected. A correction of the taper shape would be therefore required, with a broadening of the rib width along the structure which follows the apodization profile, as schematically shown on Fig. 3.14(b). Considering Eq. 2.45, the rib width should be increased of Δw_{corr} = 6 nm on both sides. Since the grating exhibits a length of several millimeters, a shallow taper correction in the nanometer scale cannot be reliably patterned and the error in the chirp linearity can be considered as a first approximation negligible.

3.5 Drop filter design

3.5.1 MMI couplers

As already anticipated in Sec. 3.2 the performance of the dispersion compensator is strictly related to the quality of the 3-dB MMI couplers. They have to be carefully designed and fabricated to exhibit a low imbalance. If the input signal is not perfectly split in equal parts on the ports *b* and *c* (see Fig. 3.3) the channel portions reflected by the gratings do not fully interfere constructively on port *d* and some power reaches port *a*.

MMI couplers have already been successfully realized with different waveguide geometries [98–100] and their realization can be considered nowadays state of the art. Within this work MMI couplers with a width of 12.2 μm and a length of 243 μm have been fabricated. The width determines how many modes can exist in the coupler region; the wider the coupler, the larger is the number of modes which contribute to the expansion and hence the more precise is the image at the output ports, however at the price of a narrower bandwidth [85]. A good compromise is found for widths about 10 μm. The length on the other hand has to be defined to be $3/2L_\pi$, where L_π is the beat length of the two lowest-order modes [84].

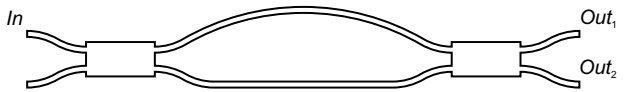

Figure 3.15: Asymmetric Mach-Zehnder interferometer used for the characterization of the MMI couplers.

In order to perform a full characterization of the MMI couplers, they have been placed in a Mach-Zehnder interferometer structure, as depicted

on Fig. 3.15. The measured transmission curves are plotted on Fig. 3.16. The comparison of the transmitted signal at the two different output ports Out_1 and Out_2 permits to determine the coupler imbalance, which results to be lower than 0.3 dB. Furthermore it can be observed that for the TE polarization a loss in the order of 1 dB is introduced. A moderate polarization dependence is also present, with a polarization dependent loss (PDL) around 0.5 dB.

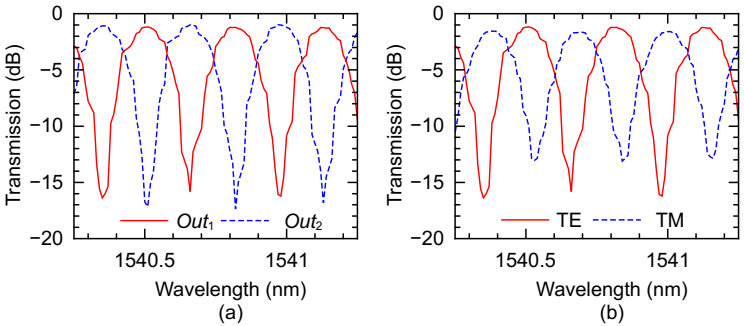

Figure 3.16: (a) Output signal spectrum at the two output ports of the MZI for the TE polarization. (b) Output signal spectrum at the output port Out_1 *for both polarizations.*

3.5.2 Waveguide coupling

Another important factor which has to be considered in the drop filter design is the grating alignment. Every small misalignment between the gratings G_1 (see Fig. 3.4) introduces a further phase shift, which would invalidate the full signal transmission at port d. To avoid such a misalignment and to minimize the effect of possible substrate inhomogeneity it is meaningful to keep the two gratings as close as possible to each other. By reducing the distance between the gratings, however, the mutual coupling increases. It is therefore necessary to find a minimal distance between two parallel waveguides without coupling.

To perform this estimation a modal analysis was performed [57] using a three dimensional mode solver [78]. In a system constituted by two parallel waveguides depicted on Fig. 3.17(a) two eigenmodes exist, a symmetric and an antisymmetric linear combination of the isolated waveguide

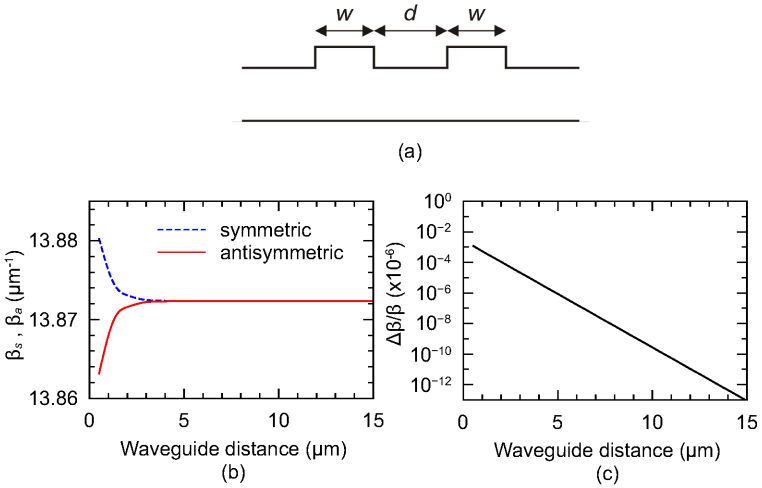

Figure 3.17: (a) Scheme of the considered coupled rib waveguides with width $w = 1.6$ μm and varying distance d. (b) Propagation constants of the symmetric (β_s) and antisymmetric (β_a) modes.

modes. The symmetric mode has a propagation constant which is slightly higher than the antisymmetric mode. The difference is related to the coupling constant μ:

$$\mu = \frac{1}{2}(\beta_s - \beta_a) = \frac{1}{2}\Delta\beta \tag{3.27}$$

where the coupling constant μ describes the spatial rate at which power transfers between the two waveguides. As the distance between the waveguides increases, the propagation constants become closer to each other and μ tends to zero, as shown on Fig. 3.17(b). As a condition for the absence of coupling between the parallel waveguides, it is useful to consider the parameter $\Delta\beta/\beta$, where β is the propagation constant in the unperturbed waveguide. The following condition is set for no coupling:

$$\frac{\Delta\beta}{\beta} \leq 10^{-6}. \tag{3.28}$$

It is fulfilled for distances between waveguides larger than 5 μm in the case of the rib waveguide geometry considered within this work (see Fig. 3.17(c)). A distance of 10 μm can be therefore considered safe, since no coupling

occurs but is still small enough to avoid that possible substrate inhomogeneity could affect the two gratings differently.

3.6 Characterization

3.6.1 Dispersion measurement

The experimental investigation of the dispersive properties of integrated gratings requires to modify the measurement setup shown on Fig. 2.20. Different methods have been proposed for the measurement of the chromatic dispersion of optical devices and within this work the modulation phase shift method has been applied [101,102], implemented by AGILENT in a Photonic Dispersion and Loss Analyzer (PDLA) tool. The signal of a tunable laser source with wavelength resolution in the order of 1 pm is modulated by an external RF modulator at frequencies between 5 MHz and 2.5 GHz and detected at the output by an amplified optical receiver. The modulation envelope of the measured data experiences a phase variation proportional to the wavelength dependence of the group delay. This phase variation is detected comparing the output signal with a reference RF path and from it the change of the group delay over a wavelength increment $\Delta\lambda$ is calculated:

$$\Delta\tau = \frac{\Delta\phi}{360^\circ} \cdot \frac{1}{f_m} \tag{3.29}$$

where f_m is the modulation frequency and $\Delta\phi$ is expressed in degrees.

3.6.2 Experimental results

In order to verify the proper alignment of the grating pairs and hence the proper functioning of the drop-filter, the transmission spectra at the output ports $Out_{1,2,3}$ (see Fig. 3.4) have been measured. They are obtained as ratio between the signal measured at the output ports and the signal measured from a plain waveguide and are shown on Fig. 3.18. The presence of a drop in the transmission spectra at Out_1 and Out_2 at λ = 1549.4 nm corresponding to a narrow band transmission peak at Out_3 proves the correct alignment of the grating pairs. At the output ports Out_1 and Out_2 a loss of 5 dB compared to a plain waveguide can be observed. The negligible difference between the two signals suggests a high symmetry of the MMI couplers. At the wavelength λ = 1549.4 nm the first pair of gratings reflects the signal over a bandwidth of about 1 nm, which is then guided through the second MMI coupler and the second grating pair to the output

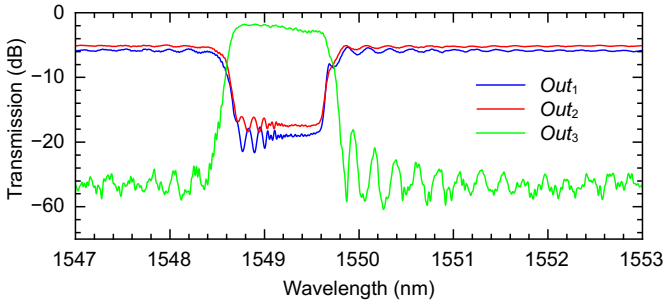

Figure 3.18: Measured transmission spectra at the three output ports of the integrated dispersion compensator. TE polarization is considered.

Out_3. This out-coupled signal is affected with a loss of 1.8 dB, which can be mostly attributed to the MMI couplers, coherently with the results presented in Sec. 3.5.1. Assuming hence a loss of about 1 dB for the couplers and the 3-dB power splitting, from the signal measured at port Out_1 and Out_2 a propagation loss of about 1 dB due to the tapered gratings can be extracted.

Using the modulation shift method described in Sec. 3.6.1, the dispersive behavior of the device has been measured. In Fig. 3.19 the transmissivity of a dispersion compensator with unapodized gratings and the corresponding group delay for both polarizations are shown. It can be observed for the TE polarization that the filter exhibits a linear increase of the group delay up to 500 ps, 250 ps from each grating pair G_1 and G_2. In the case of the TM polarization the transmission level decreases to -10 dB due to the weaker interaction between the TM optical field and the grating etched on the top of the waveguide rib. Furthermore the center wavelength for the TM mode is shifted by 3 nm towards shorter wavelengths with respect to the TE reflection peak, due to waveguide birefringence (see Fig. 2.4.2). A visible ripple about 100 ps and a frequency varying between 3.79 and 14.3 GHz is present on the group delay curves for both polarizations, with a good agreement with the theoretical predictions (see Fig. 3.11).

The reduction of this ripple has been carried out implementing the apodization with a sine profile (see Sec. 3.4.2). The width of the grating openings has been varied between 300 nm at the grating ends and 1.675 μm, i.e. from the minimal achievable opening with deep-UV lithography and the width of the rib waveguide in the middle position of the

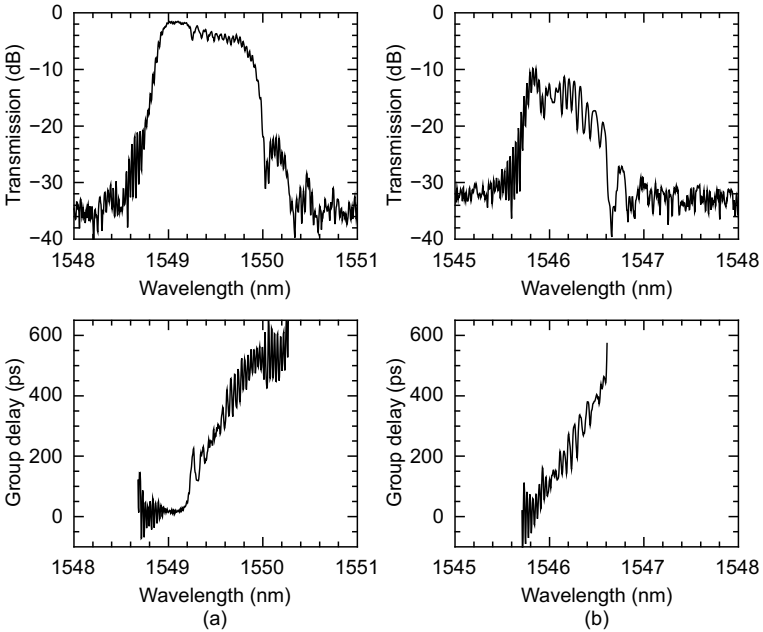

Figure 3.19: Transmission spectra and group delay profile of the output signal at port Out_3 for (a) TE and (b) TM polarizations. The grating parameters are: $\Lambda = 226$ nm, $d = 50$ nm, $DC = 0.5$, $L_g = 1$ cm and $\Delta w = 150$ nm. No apodization has been applied.

grating taper (see Fig. 3.20). The transmission spectra for Out_3 of a dispersion compensator with apodized gratings and the corresponding group delay are shown on Fig. 3.21, compared with the curves measured with the unapodized case. The apodization produces an increase of the inserted loss of the dispersion compensator of 4 dB, hence 2 dB for each grating pair, and reduces the reflection bandwidth by 200 pm. This is due to the reduced coupling coefficient in the front and in the rear part of the grating. The group delay exhibits a smoother profile with a noticeably reduced ripple. Excluding a restricted wavelength range with a pronounced ripple, the oscillation has an amplitude of about 20 ps and a period varying between 5.6 and 6.6 GHz.

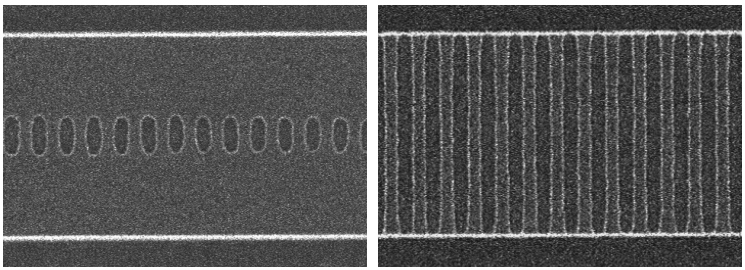

Figure 3.20: SEM micrograph of an apodized grating (a) in the front part and (b) in the central region.

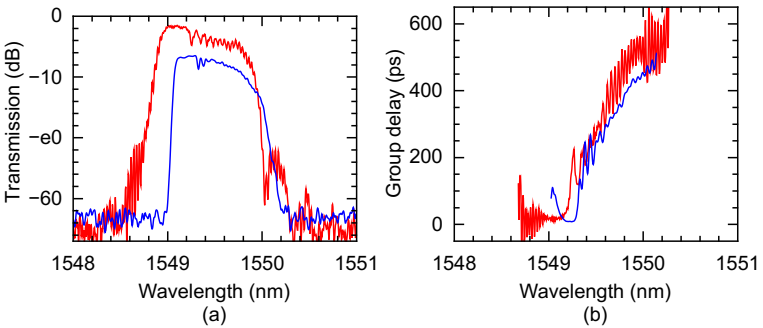

Figure 3.21: (a) Transmission spectra and (b) group delay profile at Out_3 of dispersion compensators based on unapodized (red curves) and apodized gratings (blue curves).

3.7 System emulation

The measured curve of the group delay in Fig.

On Fig. 3.23(a) the constellation diagram of a 20 Gbaud QPSK signal for a sequence of 2^{14} bits after transmission through the SSMF without compensation of residual chromatic dispersion is shown. Fig. 3.23(b) shows the constellation after compensation with the device based on unapodized gratings, and Fig. 3.23(c) the constellation after compensation with the de-

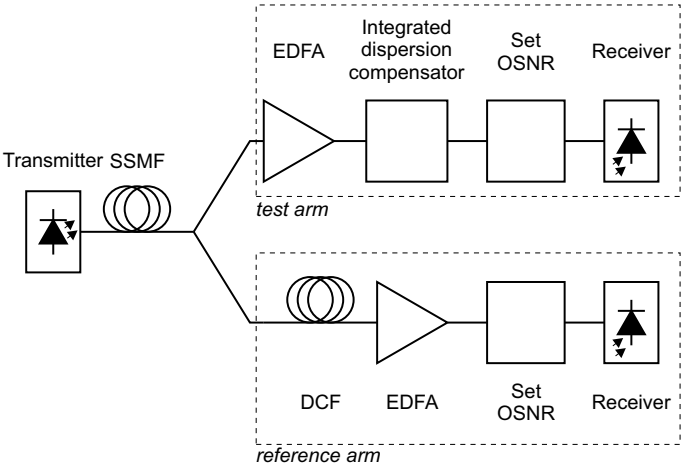

Figure 3.22: Emulation setup used for the evaluation of the system performance of the integrated dispersion compensator.

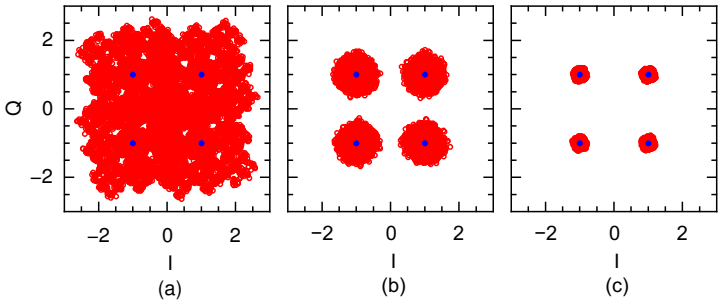

Figure 3.23: Constellation diagram at the receiver for the (a) uncompensated case, (b) compensation with unapodized gratings and (c) compensation with apodized gratings.

vice based on apodized gratings. A dispersion of -480 ps/nm is far beyond the dispersion limit at the considered data rate and modulation format, and it can be observed that without compensation the constellation is completely destroyed and no reliable detection is possible. A signal re-

generation is partly possible with the dispersion compensator based on unapodized gratings, however, with relatively high margins of error. In this case a standard deviation $\sigma = 0.22$ from the ideal constellation point under the assumption of a Gaussian distribution can be observed. From it the symbol error probability can be calculated [103]:

$$SER = 2Q\left(\frac{1}{\sigma}\right)\left[1 - \frac{1}{2}Q\left(\frac{1}{\sigma}\right)\right] \tag{3.30}$$

where the function $Q(x)$ is defined as:

$$Q(x) = \frac{1}{\sqrt{2\pi}}\int_{x}^{+\infty}\exp\left(-\frac{t^2}{2}\right)dt = \frac{1}{2}\mathrm{erfc}\left(\frac{x}{\sqrt{2}}\right), \quad x \geq 0. \tag{3.31}$$

A value of $SER = 5 \times 10^{-6}$ is achieved for the unapodized case, which decreases to almost 0 for the apodized case ($\sigma = 0.07$).

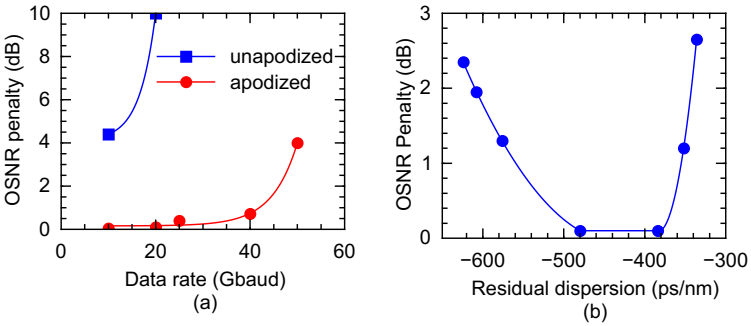

Figure 3.24: (a) OSNR penalty for different data rates for both unapodized and apodized gratings. (b) Variation of the OSNR penalty for different residual dispersion values at a data rate of 20 Gbaud using a dispersion compensator based on apodized gratings.

The effect on the OSNR penalty has been considered for different data rates and the results are summarized on Fig. 3.24(a). The OSNR penalty is given by the difference between the set OSNR values on the two arms of the emulation setup of Fig. 3.22 to achieve an error rate of 10^{-5}. It can be seen that the penalty values increase rapidly for higher data rates in the unapodized case reaching values beyond 10 dB, while they remain below

1 dB for the apodized case. They become larger only for data streams over 50 Gbaud because of bandwidth limitations.

At a data rate of 20 Gbaud the device degrades the OSNR by 0.1 dB, and this penalty increases if the accumulated dispersion deviates from the value of -480 ps/nm. The penalty is kept below 1 dB for dispersion values between -558 and -354 ps/nm. For smaller or larger values it increases rapidly, requiring the possibility to tune the dispersion of the gratings.

4
Dispersion tuning

4.1 Thermal tuning of Bragg grating

In Sec. 1.2 it has been shown that the residual dispersion is a varying quantity. It is straightforward that an efficient dispersion compensator has to be tunable, in order exhibit always a dispersion which is opposite to the actual residual dispersion. A simple method to tune the response of integrated devices is varying their temperature, since it alters the material properties. Two separate effects have to be considered in case of a temperature increase: the thermal expansion and the thermo-optic effect. The first one produces a linear volume expansion and hence a variation of the grating period:

$$\Lambda(\Delta T) = \Lambda_0(1 + k_T \Delta T) \tag{4.1}$$

where Λ_0 is the period at the starting temperature, ΔT the temperature variation and k_T the thermal expansion coefficient. The second effect produces a thermally induced change of the refractive index:

$$n(\Delta T) = n_0 + \frac{dn}{dT}\Delta T \tag{4.2}$$

where dn/dT is the thermo-optic coefficient.

The expansion of the grating period and the variation of the effective index would produce a shift of the reflected wavelength in a heated Bragg grating. This shift can be calculated substituting the two previous equations into the Bragg condition (see Eq. 2.22) and differentiating:

$$\frac{\partial \lambda_B}{\partial T} = 2n_0 k_T \Lambda_0 + 2\Lambda_0 \frac{dn}{dT}. \tag{4.3}$$

Considering silicon as guiding material, the thermal expansion coefficient is $k_T = 2.5 \times 10^{-6}$ K^{-1} [104] and the thermo-optic coefficient around

the room temperature is $dn/dT = 1.8 \times 10^{-4}\,\mathrm{K}^{-1}$ [105]. Hence the expected thermally-induced variation of the reflected wavelength of the grating is 80 pm/K. The major contribution in Eq. 4.3 is given by the thermo-optic effect.

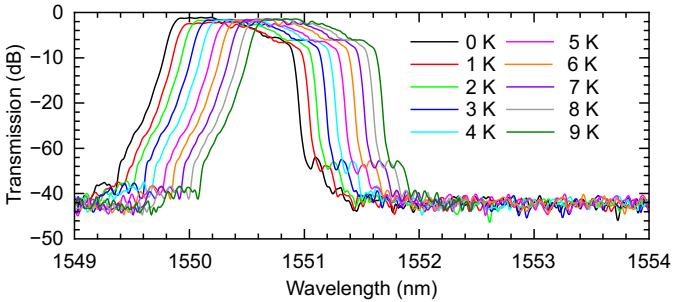

Figure 4.1: Transmission spectra at Out_3 of the dispersion compensator for different values of temperature increase. The starting temperature is 305 K.

The transmission spectra of the fabricated dispersion compensator have been measured at different temperatures, mounting it on a Péltier element and the results are shown on Fig. 4.1. Increasing the operation temperature, the period expands and the refractive index of the waveguide rises, producing a red shift of the Bragg wavelengths of 80 pm/K, in good agreement to the previous calculation and what has been presented in [61].

4.2 Thermal tuning of the dispersion

The observed shift of the reflected wavelength due to temperature variations can be employed to tune the dispersion in chirped gratings. In Fig. 4.2 the tuning principle is schematically explained. While a constant temperature increase produces an overall shift of the reflectivity spectrum to longer wavelengths (Fig. 4.2(a)), a temperature gradient along the grating produces a thermally induced chirp, with a consequent broadening of the bandwidth on the long wavelength side (Fig. 4.2(b)). Considering the thermal expansion of the overall grating length to be negligible, the group delay difference between the wavelength reflected at the front and the one reflected at the end of the device does not change with the temperature. However the variation of the bandwidth leads to a variation of the dispersion, as stated by Eq. 1.8. The center wavelength results also shifted

towards longer wavelengths. Since it is necessary to have the reflectivity bandwidth always centered at the channel wavelength, it is straightforward to center the temperature gradient ΔT at the middle point of the grating. This means that the grating temperature is first increased homogeneously and then differentially increased on one end and decreased at the other end (Fig. 4.2(c)). In this way the power consumption remains constant for every desired dispersion value.

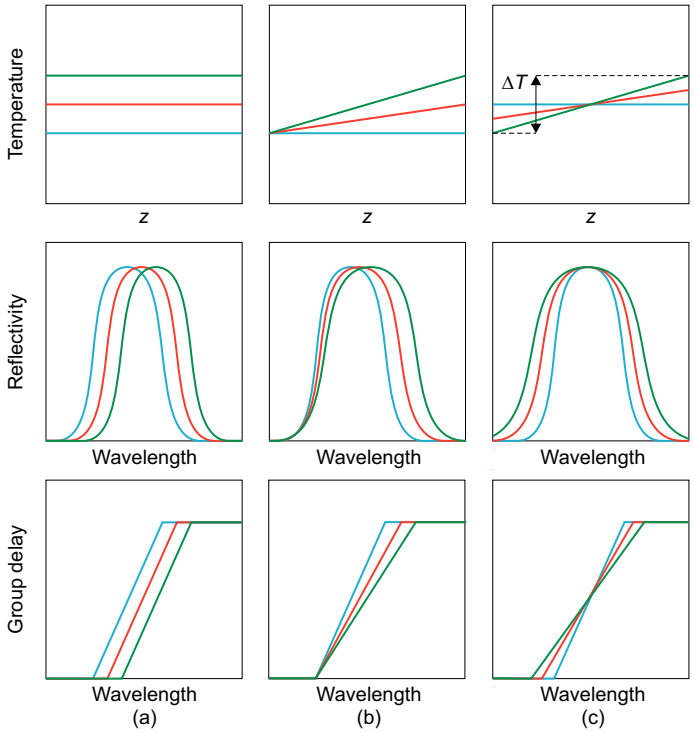

Figure 4.2: Effect of the temperature on the reflection spectrum and group delay curve of a chirped gratings. (a) Uniform temperature, (b) linear gradient along the grating length and (c) differential linear gradient centered on a mean value.

Numerical calculations are required to quantify the effect of the temperature gradient on the grating dispersion. In order to include the thermal effects into the grating simulation, it is useful to translate the period

expansion and the variation of the refractive index in an additional chirp. An effective grating is thus generated, with the effective index of the case for $\Delta T = 0$ and a new chirp. This is obtained from the Bragg condition:

$$\lambda_B(z) = 2n_{\text{eff}}\Lambda_{\text{eff}}(z) = 2\left(n_{\text{eff}} + \frac{\partial n}{\partial T}\Delta T(z)\right)\Lambda(z)(1 + k_T\Delta T(z)) \tag{4.4}$$

and hence

$$\Lambda_{\text{eff}}(z) = \frac{\left(n_{\text{eff}} + \frac{\partial n}{\partial T}\Delta T(z)\right)\Lambda(z)(1 + k_T\Delta T(z))}{n_{\text{eff}}}. \tag{4.5}$$

Now all the informations about the temperature effects are condensed in the new effective chirped grating with period $\Lambda_{\text{eff}}(z)$, keeping the calculation complexity unchanged, compared to the cases considered so far.

If the slope of the applied thermal gradient induces a chirp which is concordant with the intrinsic one, the effect is an increase of the chirp and hence a bandwidth broadening (reduced dispersion). On the other hand, if the sign of the thermal gradient is reversed, this acts against the original chirp, with a narrowing of the bandwidth. For small temperature variations this means that the dispersion increases. Over a certain value of temperature, the original chirp is cancelled and the grating becomes uniform, with zero dispersion. Increasing the gradient amplitude further, the thermal chirp predominated and the slope of the group delay profile is reversed. In the following thermal gradients with a slope concordant with the intrinsic chirp are defined as positive, while gradients with opposite slopes are defined as negative.

On Fig. 4.3(a) the reflectivity spectra and the group delay curve of an apodized chirped grating for different positive temperature gradients are shown. As expected the overall group delay difference of 130 ps remains constant, since the grating length of 5 mm is altered only infinitesimally. However the reflection bandwidth broadens for large gradients, with a variation of 1.8 nm for a thermal gradient of 30 K. This bandwidth broadening causes a reduction of the group delay slope, and hence of the grating dispersion.

The effect of reversing the sign of the thermal gradient is shown on Fig. 4.3(b). For small gradients the bandwidth is slightly narrowed and the dispersion increases. However at a temperature gradient of -10 K the chirp is canceled and the grating acts as uniform. For larger gradient amplitudes the thermal chirp predominates and a negative group delay slope can be observed, meaning a negative dispersion. The group delay ripple results to be more pronounced than in the case of positive gradients. The achieved

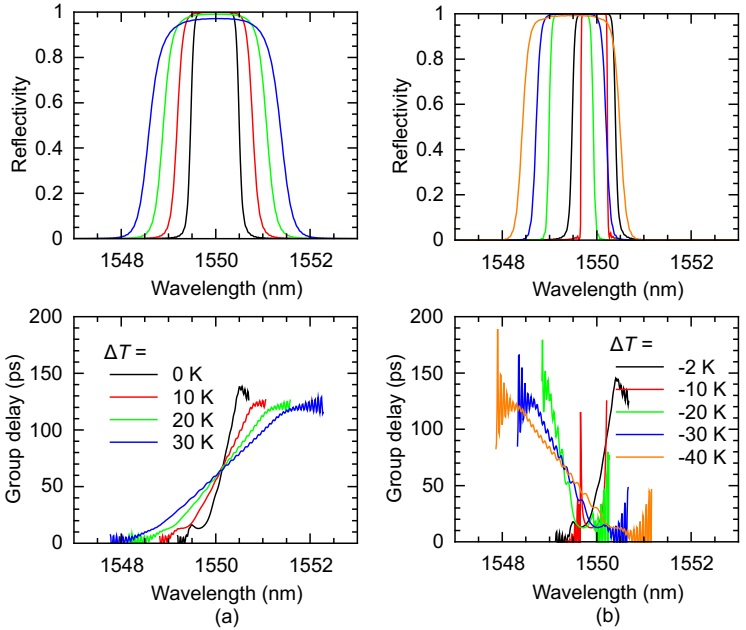

Figure 4.3: Computed reflection spectra and group delay profile of a chirped grating with (a) positive and (b) negative temperature gradients. A sine profile apodization has been considered. The grating parameters are: Λ_0 = 225 nm, $\Delta\Lambda$ = 0.146 nm (corresponding to Δw = 150 nm), d = 50 nm and L_g = 5 mm.

dispersion values for different temperature gradients are summarized on Fig. 4.4. The relation can be described with a hyperbola, with the center shifted to a gradient amplitude of -10 K. A temperature increase of 10 K is sufficient to reduce the dispersion of a factor 2, therefore only small temperature variations are required for a fine tuning of the dispersion. A large negative gradient is required to reverse the sign of the dispersion, however at the price of a stronger group delay ripple.

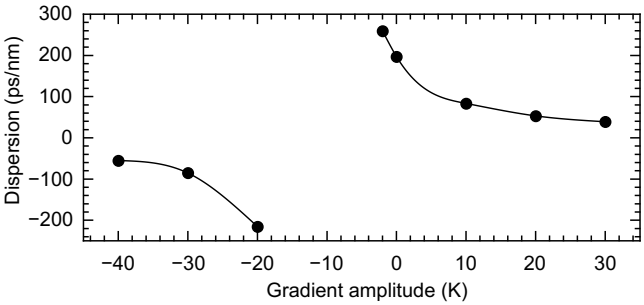

Figure 4.4: Computed dispersion values for different applied temperature profiles.

4.3 Heater design

A straightforward manner to heat the gratings for the dispersion tuning is to place metallic heaters in their neighborhood. They consist simply of metallic wires, whose dimensions are chosen to exhibit a non negligible resistance. When current flows into the wire electrical power is translated into heat. To achieve a variable temperature gradient along the grating, it is necessary to heat the structure punctually. This can be obtained discretizing the desired temperature profile placing an array of heaters driven separately with different currents. Since the heat spreads in every direction, the development of specific concepts is required to confine the heat in the area of interest, reducing the electrical power consumption and avoiding or at least reducing the crosstalk with other heaters.

The array of heaters placed along the grating permits to generate an arbitrary thermal profile and hence manipulate the dispersion in a flexible way. The more heater segments are present, the more accurate is the reconstruction of the desired profile. However a large number of heaters

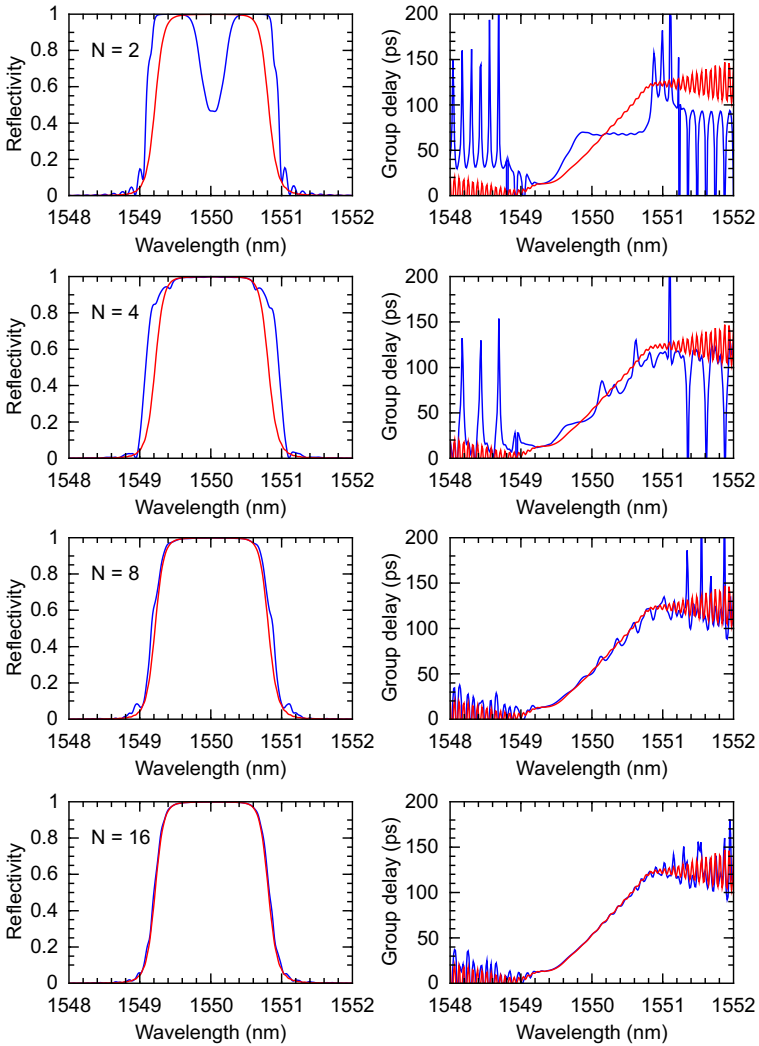

Figure 4.5: Simulated reflected spectra and group delay profiles of a chirped grating with an applied temperature gradient of $\Delta T = 10$ K realized with N heaters. The red curve indicates the ideal case of a linear gradient for comparison.

translates into a large number of current or voltage values which have to be determined and set independently. Thus a compromise between high precision and low complexity has to be determined. Numerical calculations have been performed and in Fig. 4.5 the obtained reflectivity spectra and group delay profiles are shown. An apodized chirped grating with an applied linear gradient of ΔT =10 K has been considered. The number of heaters used to reproduce this gradient has been varied and compared with the ideal case. Already with four heaters it is possible to achieve an almost linear group delay profile, however affected by a strong and irregular ripple. An almost perfect reproduction of the ideal case is obtained with 16 heaters. This would mean that for the tuning of the complete dispersion compensator 64 different heaters have to be controlled, assuming a heater array per grating, with 32 different currents. This complexity can be reduced by a factor 2 considering arrays of 8 heaters. In this case the approximation of the ideal case is still good, at the price of an added group delay ripple with an amplitude of 10 ps.

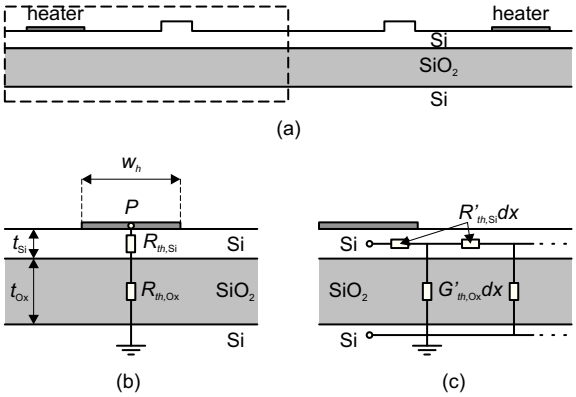

Figure 4.6: (a) Considered geometry for the calculation of the required power. (b) Thermal equivalent circuit of the slab region close to the rib with a heater. (c) Equivalent thermal circuit for the analysis of the lateral heat diffusion [106].

The heat generated by the heaters has to be effectively transferred to the grating. The released thermal energy spreads in every direction in the SOI substrate. However the thermal conductivity of silicon exhibits a value of $\sigma_{th,\mathrm{Si}}$ = 148 W/(K·m) which is much larger than the one of silica ($\sigma_{th,Ox}$ = 1.38 W/(K·m)). Therefore most of the heat remains in the guiding

silicon layer and spreads laterally, while only a small fraction of it passes the silica barrier of 2 μm and reaches the substrate.

To have an idea about the heat diffusion in the SOI material it is useful to model the structure with an equivalent thermal circuit. Assuming as a first approximation that the two parallel gratings are tuned separately and are thermally decoupled, it is possible to reduce the analysis to only one grating and the corresponding heater (see Fig. 4.6(a)). Only one heater is considered, and the power consumption of the whole heating array is obtained multiplying by 8 the obtained results. Each material sections can be described with a thermal resistance, which permits to determine the relation between the temperature increase and the applied heating power [106]:

$$\Delta T = R_{th} P. \tag{4.6}$$

The thermal resistance depends, like the electrical one, on the conducting properties of the material and the sizes of the considered section:

$$R_{th} = \frac{l_h}{A_h \cdot \sigma_{th}} \tag{4.7}$$

where l_h and A_h are the length and the cross-section of the heated section respectively and σ_{th} the thermal conductivity of the material.

Considering the scheme depicted on Fig. 4.6(b), the heating power P generated from the resistor flows from the top through the top silicon layer and the oxide barrier to the silicon substrate, which acts as thermal ground. Once the values for the thermal resistances for the top silicon and oxide layers are known ($R_{th,\mathrm{Si}}$ and $R_{th,Ox}$ respectively), the required power to achieve the desired temperature increase can be calculated from Eq. 4.6.

The calculation of the heated cross-section A_h is necessary for determining the thermal resistance. The lateral heat diffusion has to be analyzed, using the equivalent circuit of Fig. 4.6(c) [106]. Here R'_{th} indicates the thermal resistance per unit length along the silicon guiding layer and G'_{th} the thermal conductivity per unit length to ground through the silica barrier:

$$\begin{aligned} R'_{th} &= \frac{1}{\sigma_{th,\mathrm{Si}}} \frac{1}{t_{\mathrm{Si}} L_h} \\ G'_{th} &= \sigma_{th,Ox} \frac{L_h}{t_{Ox}} \end{aligned} \tag{4.8}$$

where L_h is the length of the heater. The depicted circuit is similar to the equivalent circuit of an electrical conductor and a thermal diffusion length

can be calculated:

$$L_{th} = \frac{1}{\sqrt{G'_{th} R'_{th}}}. \tag{4.9}$$

Substituting Eq. 4.8 into Eq. 4.9 one obtains:

$$L_{th} = \sqrt{\frac{\sigma_{th,Si}}{\sigma_{th,Ox}} t_{Si} \cdot t_{Ox}} \approx 10\sqrt{t_{Si} \cdot t_{Ox}}. \tag{4.10}$$

With t_{Si} = 1 μm (thickness of the slab region at the side of the rib) and t_{Ox} = 2 μm, a decay constant of 13.4 μm is obtained.

It is possible to consider as a heated cross section

$$A_h = L_h \cdot (w_h + 2L_{th}) \tag{4.11}$$

where w_h is the heater width. A heater length of L_h = 1.2 mm has been chosen, considering an array of 8 heaters along a grating with a length of L_g = 1 cm. This permits to calculate the thermal resistance:

$$R_{th} = \frac{t_{Ox}}{\sigma_{th,Ox} A_h} = 41.82 \ \frac{\mathrm{K}}{\mathrm{W}} \tag{4.12}$$

Considering this resistance, a power of 239 mW is required to achieve a temperature increase of 10 K in the silicon layer.

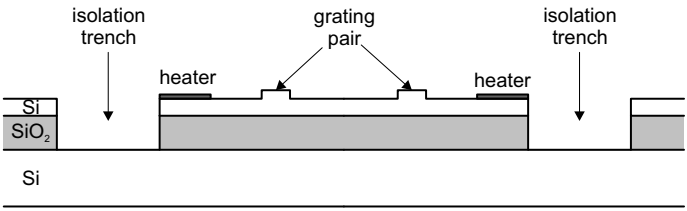

Figure 4.7: Scheme of an isolation trench at the side of the heater through the top silicon layer and the oxide barrier.

Since it is mandatory to reduce the power consumption and avoid to heat up undesired neighboring structures, a lateral heat confinement has to be implemented. This can be achieved etching broad trenches at the side of the couple heater-grating until the substrate (see Fig. 4.7). This reduces the heated cross section and increases the thermal resistance:

$$\begin{aligned} A_h &= L_h \, (w_h + L_{th}) \\ R_{th} &= \frac{t_{Ox}}{\sigma_{th,Ox} A_h} = 75.5 \ \frac{\mathrm{K}}{\mathrm{W}}. \end{aligned} \tag{4.13}$$

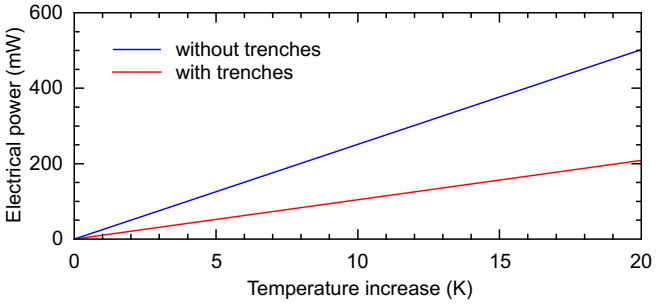

Figure 4.8: Calculated relation between the required electrical power to be applied and the temperature of the waveguide core for three geometrical configurations.

With such a thermal resistance the temperature increase of 10 K is achieved with a power of P = 132 mW.

In order to quantitatively verify these analytical estimations, numerical simulations with the finite-element software Ansys have been performed. For this, heaters made of aluminum have been considered, with a length of L_h = 1.2 mm, a width of w_h = 3 μm and a height of t_h = 200 nm. They are separated from the silicon by a thin silica layer of 200 nm, which has the function to electrically isolate the metal wires from the substrate, avoiding an undesired electrical crosstalk between heaters. The aluminum stripe is placed at a distance of d_h = 4 μm from the waveguide. This distance is smaller than the calculated thermal diffusion length (see Eq. 4.9) and permits therefore to transfer heat to the grating. At the same time it is large enough to avoid interaction with the optical field (see Fig. 3.17(b)).

The necessary electrical power to achieve a specific temperature increase in the waveguide has been computed and the results are plotted on Fig. 4.8. In the considered temperature range a linear dependence can be observed, and from the curve slope the thermal resistance of the structure has been extracted. A clear reduction of the required power occurs for the configurations with isolation trenches. An increase of 10 K of the rib core temperature is achieved applying a power of 251 mW (R_{th} = 39.8 K/W), reduced to 104 mW (R_{th} = 96.1 K/W) for the deep trenches. This means that the tuning of the whole dispersion compensator requires the activation of 32 heaters, with a total power consumption of 8 W without trenches or 3.3 W with deep trenches. This latter solution is therefore strongly preferred.

The grating pairs of the dispersion compensator require to be equally tuned , in order to warrant the full signal transmission at the output port. Thus the assembly has to be kept symmetric, with the grating pair in the middle, the heaters on the external sides, and everything isolated with trenches (50 μm $\times$ 1 mm). On Fig. 4.9 the structure of one segment of the tuning array is shown. Each end of the heater is covered with a thicker aluminum pad (500 nm) for the external contact.

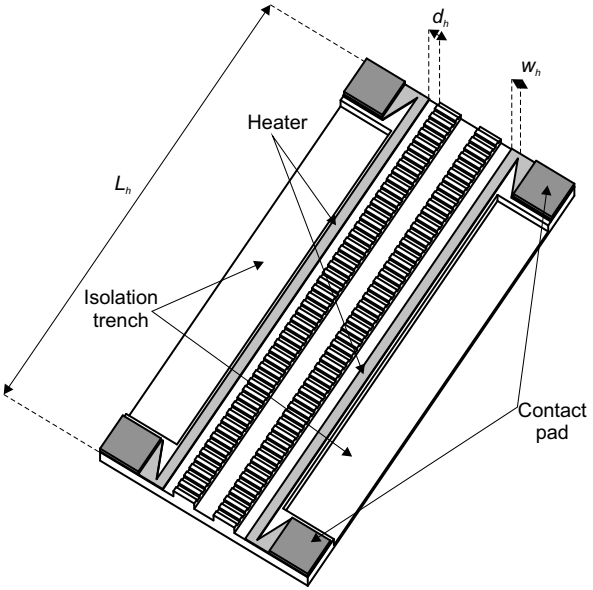

Figure 4.9: Sketch of a section of the heating array. The heaters exhibit a length of L_h = 1.2 mm, a width of w_h =3 μm and a distance from the rib of d_h = 4 μm.

4.4 Characterization

Contrarily to what has been described in the previous chapters, the experimental characterization of the tunable dispersion compensator requires not only the in and out coupling of the lightwave signal, but also the electrical connections to drive the 32 heaters. Since every heater should be driven separately to have the full tuning freedom, 64 electrical connec-

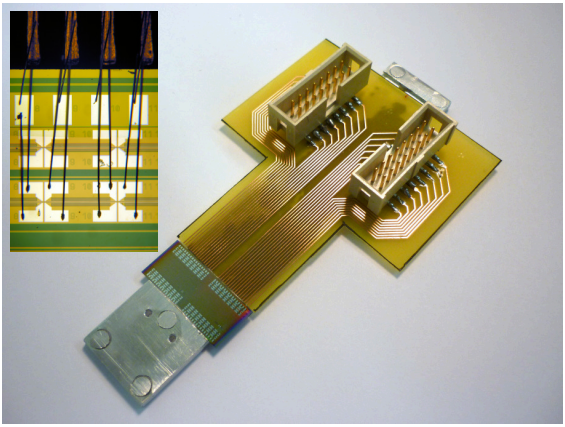

Figure 4.10: Mounted chip with the PCB for electrical contacts. In the inset picture the wire bonds from the wires on the PCB to the contact pads of the heaters are shown.

tions are required. The polished dice with the fabricated devices has been fixed on an aluminum plate using a thermal conducting adhesive paste to ensure the thermal grounding (see Fig. 4.10). Close to it a printed circuit board (PCB) with soldered connectors has been placed and wired bonded with the connection pads of the dispersion compensator. This permits the electrical connection of the integrated heaters with an external multi-channel power supply (WIENER MPOD Mini Crate). For each channel a voltage up to 60 V with a maximum power of 50 W and a voltage ripple smaller than 30 mV can be applied.

The dependence between the grating temperature and the electrical power has been determined applying an equal voltage to all heaters. The structure is hence heated uniformly and the known effect on the Bragg wavelength (see Sec. 4.1) permits to extract the temperature. On Fig. 4.12(a) the transmission spectra measured at port Out_1 (see Fig. 3.4) for different applied voltages are shown. A shift to longer wavelengths for higher voltages can be clearly observed. Since the two heater arrays across each grating pair are connected in parallel (see Fig. 4.11), the measured resistance of 51 Ω corresponds to a resistance value of R_h = 102 Ω for each heater. With this value it is possible to determine the electrical power transferred

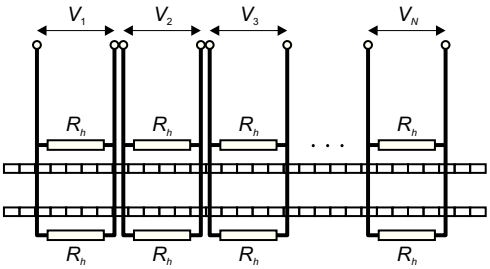

Figure 4.11: Scheme of the electrical connections of the heater arrays across a grating pair. Since both gratings have to be heated symmetrically, the same voltage V_n is applied to each pair of resistances R_h connected in parallel.

to each heater:

$$P_n = \frac{2V_n^2}{R_h} \tag{4.14}$$

where V_n is the voltage applied to the n-th pair of heaters (see Fig. 4.11). On Fig. 4.12(b) the relation between the electrical power and the temperature increase calculated from the wavelength shift is plotted. A linear dependence can be observed, corresponding to a thermal resistance of about 100 K/W. This value is in good agreement to the theoretical expectations for deep isolation trenches (see Fig. 4.8).

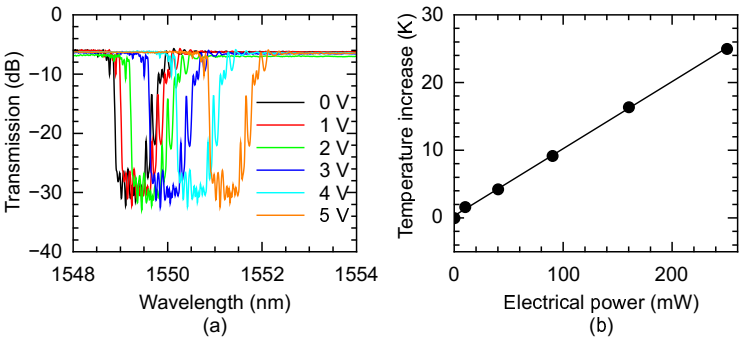

Figure 4.12: Transmission spectra at port Out_2 for different applied voltages. (b) Relation between the temperature increase in the grating and the applied electrical power per heater.

Knowing the thermal resistance of the system it is possible to determine the required power for each desired temperature profile. As described in Sec. 4.2 the gratings have to be first heated up to a mean value, on which a differential gradient is superimposed. In this way the power consumption remains constant. The larger the desired gradients, the higher should be the average level, with a consequent higher required power.

Simulations showed that only temperature gradients with amplitudes lower than 30 K can produce significative variations of the dispersion (see Fig. 4.4). An average value of 148 mW electrical power per heater (corresponding to a voltage of 3.8 V) has been chosen, providing a average temperature increase of 15 K. In Fig. 4.13 the different values of absorbed electrical power for each heater along the gratings for different temperature gradients are shown. For small gradients of 5 K the power deviates by 25 mW from the average value. The deviation increases up to 148 mW to produce a gradient of 30 K. Considering the 32 heaters, the overall power consumption of 4.74 W for the whole dispersion compensator remains constant for each configuration.

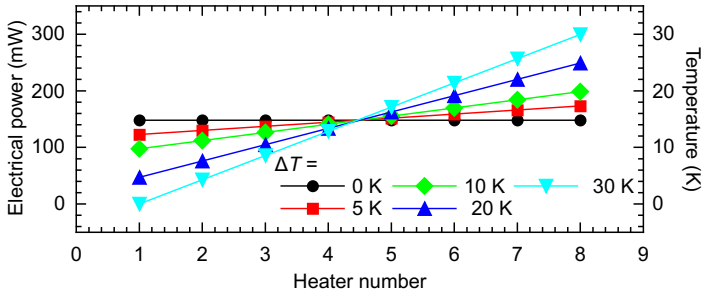

Figure 4.13: Applied power to the different heaters along each grating pair to achieve the desired temperature profiles.

Positive temperature gradients have been applied to the dispersion compensator, i.e. gradients which induce an chirp concordant with the one already present in the grating. The signal transmitted to the port Out_3 (see Fig. 3.4) has been measured and the corresponding power and group delay curves are plotted in Fig. 4.14 for different temperature gradients. The reflection spectrum of the gratings (and hence transmission of the device) broadens for larger gradients, due to the induced variation of the refractive index and expansion of the grating period. This variation of

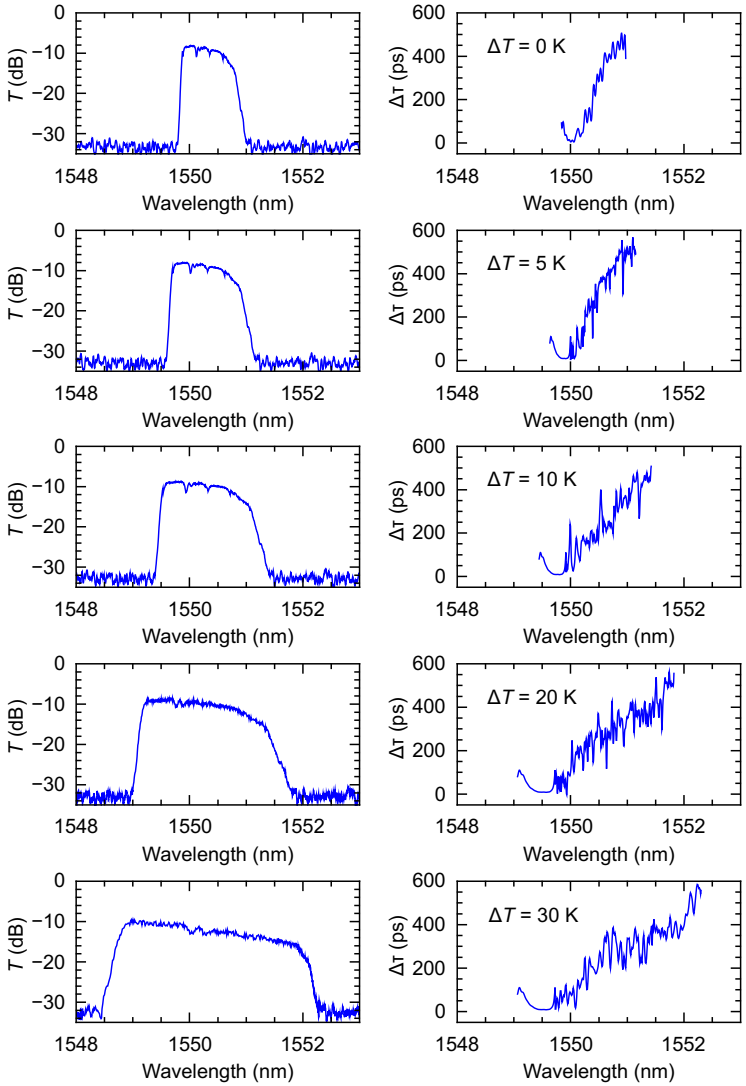

Figure 4.14: Measured transmission spectra and group delay curves at port $\mathbf{Out}_3$ *of the dispersion compensator for different positive temperature gradients. Apodized gratings have been considered. TE polarization.*

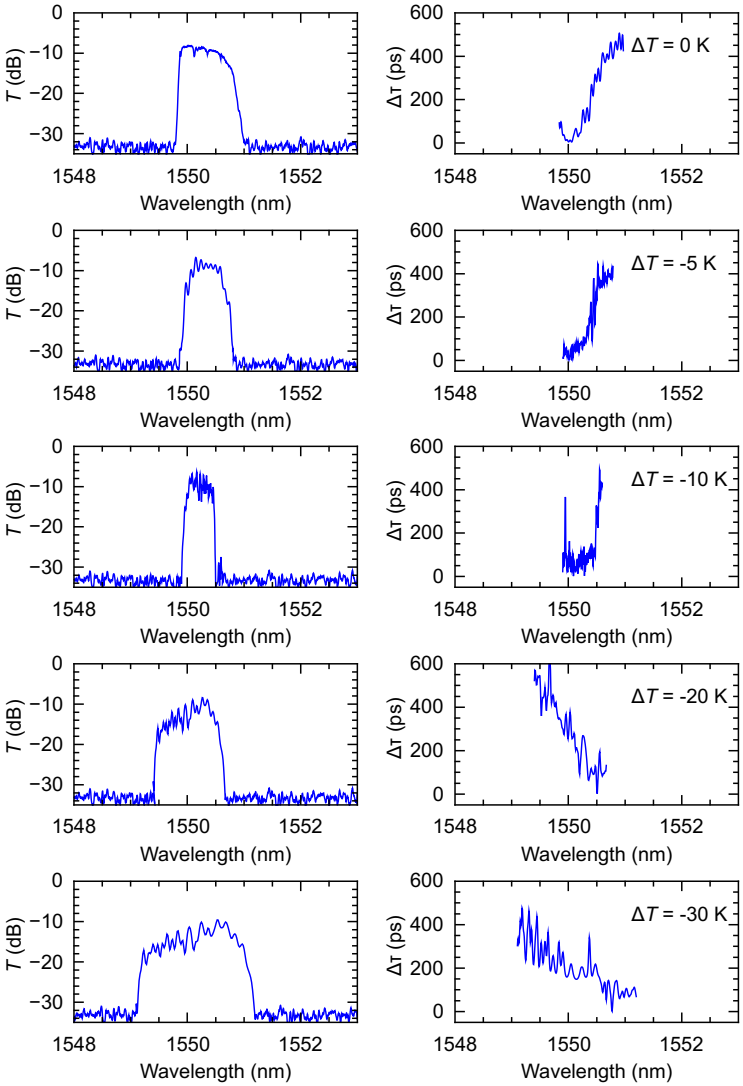

Figure 4.15: Measured transmission spectra and group delay curves at port Out_3 *of the dispersion compensator for different negative temperature gradients. Apodized gratings have been considered. TE polarization.*

the bandwidth translates into a reduction of the slope of the group delay curve. As theoretically expected, larger temperature gradients produce a reduction of the grating dispersion. Due to discretization of the temperature profile using eight heaters, gradients with a larger amplitudes can be resolved in a less smooth way. Sudden temperature steps along the gratings occur and can be considered as an explanation of the increase of the group delay ripple, which reaches an amplitude of 130 ps with in the case of a temperature gradient of ΔT = 30 K.

In Fig. 4.15 the effect of negative temperature profiles can be observed. In this case the induced chirp acts against the intrinsic one, with the possibility to reverse the sign of the group delay slope. It can be observed that small temperature variations produce simply a slight narrowing of the bandwidth, making the group delay curve steeper. This increase of the chromatic dispersion occurs until the thermally induced chirp equals the opposite of the intrinsic one. In this situation, which can be observed for gradient amplitudes of about -10 K, the grating behaves uniform and no dispersion is introduced or compensated. Further increases of the gradient amplitude allow the thermal chirp to predominate and lead to negative slopes of the group delay curve. As observed in the case of positive gradients, an increase of the group delay ripple occurs. This will limit the data rate of the input signal.

The dispersion values obtained fitting linearly the measured group delay curves for the different temperature profiles are summarized in Fig. 4.16. The intrinsic dispersion of 480 ps/nm (ΔT = 0 K) can be varied applying a temperature gradient along the gratings. A gradient amplitude of 10 K is sufficient to halve the dispersion. By reversing the sign of the gradient it is possible to slightly increase the dispersion, or even reverse its sign.

The variation of the amplitude of the gradient also produces a variation of the group delay ripple, with a consequent limitation of the data rate of the incoming signal. As discussed in Sec. 3.4.1 the product of the ripple amplitude and ripple frequency $\tau_{pp} \cdot f_p$ can be considered as a figure of merit for the effect of the ripple. This product has been calculated for the different gradient configurations shown in Fig. 4.14-4.15 and the results are plotted in Fig. 4.17. It can be observed that each temperature profile with an amplitude larger than zero produce an increase of the effect of the group delay ripple. The larger the amplitude of the gradient, the stronger is the ripple. This can be explained considering that the deviation of the generated stepped thermal profile from the ideal linear one increases for larger amplitudes, with a consequent worse performance. Nevertheless, gradient amplitudes up to 20 K are sufficient to reduce the dispersion of a

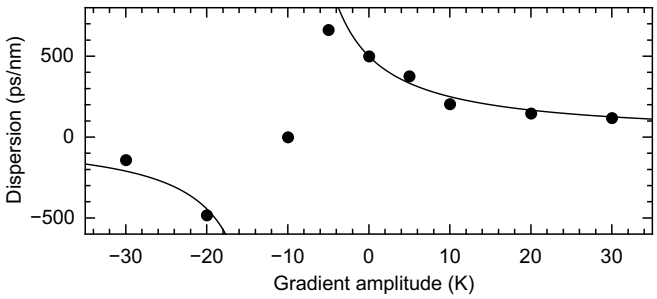

Figure 4.16: Measured dispersion values for the different gradient amplitudes. The points are fitted with a hyperbola.

factor 3, and larger ones do not lead to a significant variation. Therefore limiting the operation to such values permit to keep the effect of the group delay ripple moderate.

The implementation of a temperature gradient with an array of equal heaters allows not only to achieve linear profiles, but also arbitrary ones. In Fig. 4.18 an example of different linear and parabolic profiles and the corresponding group delay curves is shown. This latter one can be tailored in an arbitrary way, according to the requirements of the dispersion profile of the incoming signal. In this case a gradient with an amplitude of 5 K has been applied. The achieved group delay profile can be fitted with a polynomial expression corresponding to the thermal profile. The group delay ripple behavior remains in general unchanged, however in the case of the root profile a strong suppression of the ripple in the region of shorter wavelengths occurs. This can be understood considering that in this region the thermally induced chirp raises faster than linear, reducing the effect of the front part of the grating. This effect opens the opportunity to reduce the effect of the group delay discussed previously in this section. Increasing the number of heaters and superposing steeper profiles in the front and rear part of the grating could help to achieve a smoother group delay curve.

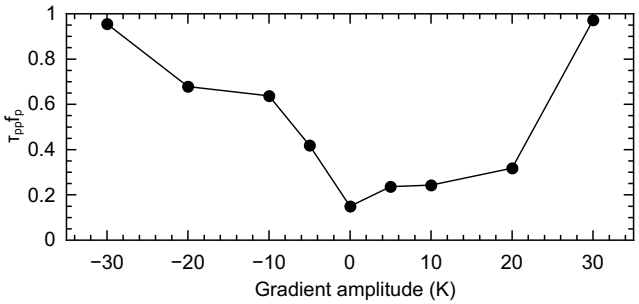

Figure 4.17: Amplitude-Frequency product of the measured group delay ripple for different temperature gradient amplitudes.

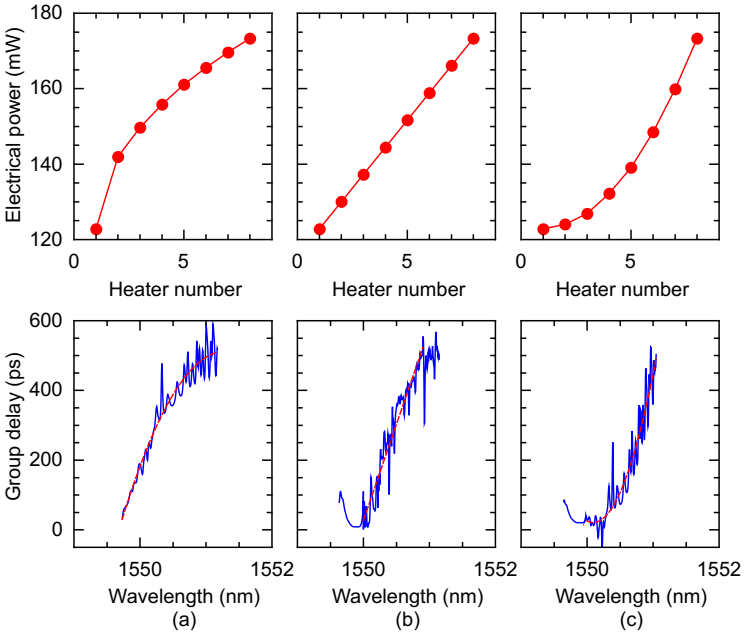

Figure 4.18: Applied electrical power profile and corresponding measured group delay curve. (a) Squared root profile, (b) linear profile and (c) parabolic profile. The gradient amplitude is all three cases 5 K.

5 Conclusion

The realization of an integrated device for the compensation of the residual chromatic dispersion is mandatory for the implementation of monolithic receiver modules, with combination of optics and electronics. Different solutions based on FIR and IIR filters have been proposed, as discussed in the first chapter. They are obtained cascading specific filter structures like ring resonators, Mach-Zehnder interferometers or arrayed waveguide gratings. Bragg gratings offer the opportunity to implement an IIR lattice filter in a very compact way and permit a simple dispersion compensation. Simply adjusting the chirp (linear for first order dispersion) all the filter coefficient are automatically defined; if the chirp can be manipulated, the dispersion can be externally tuned according to the necessity.

Silicon is an optimal material for the realization of optical components, since it is transparent in the wavelength range used for optical communications and the standard fabrication processes of microelectronics can be also applied. The realization of Bragg gratings in silicon waveguides has already been demonstrated [60, 62, 73, 75, 77], however only uniform, and without providing a deep theoretical analysis.

Within this work the realization of integrated Bragg gratings on silicon for dispersion compensation has been demonstrated. First of all the theoretical background has been analyzed. It has been shown that the coupled mode theory, widely used for grating modelling, provides reliable results only if strict conditions of shallow index modulations are hold, since it is considers only one forward and one backward propagating mode. The full description of Bragg gratings require more precise calculation methods, which are able to take into account the coupling between all waveguide modes for all possible grating strength. The bidirectional eigenmode propagation method proved to provide reliable results also for strong gratings with a moderate calculation complexity and has been therefore applied for

the design of Bragg gratings. The influence of the different geometry parameters has been systematically considered to achieve gratings reflecting at λ = 1550 nm over a bandwidth narrower than 1 nm and losses lower than 0.2 dB for other wavelengths.

The fabrication of the gratings has been performed with standard bi-CMOS processes based on deep-UV lithography, and it was demonstrated that this procedure permits to achieve results comparable with the state-of-the-art fabrication techniques with electron beam lithography. The new approach has the advantage of a higher throughput and the possibility to pattern stitching-free gratings without length limitation.

In the third chapter a robust implementation of the chirp tapering the waveguide width has been presented, showing that a grating patterned on a waveguide with a taper width of 150 nm and a length of 5 mm exhibits a dispersion of about 100 ps/nm over a bandwidth of 1 nm. Gratings on a tapered waveguide exhibit a specific dispersion but cannot be applied for compensation purposes because of the strong group delay ripple. This is generated by the reflections at the ends of the grating due to the abrupt beginning end ending of the grating index modulation. The suppression of these reflections and hence of the group delay ripple is mandatory, since each deviation from a linear group delay profile corresponds to a signal distortion and intersymbolic interference.

It has been shown that apodizing the grating with a half sine profile, i.e. varying the width of the grating openings, the group delay ripple can be successfully suppressed. The gratings permit therefore to compensate a dispersion of about 250 ps/nm with a length of 1 cm and allow a correct signal detection (OSNR penalty below 1 dB for SER = 10^{-5}) up to a data rate of 40 Gbaud.

The tapered gratings have been inserted into a drop-filter structure which cascades two grating pairs. It permits to double the achievable dispersion and to separate the compensated channel without the use of a circulator. The whole device exhibits a length of 2.5 cm and a width of a few tens of micrometers, permitting hence a high integration level.

Due to the thermo-optic effect and the thermal expansion, a temperature variation of the grating produces a shift of the reflected wavelength of about 80 pm/K. This property has been used to tune the dispersion applying a thermal gradient along the grating. The gradient induces an extra chirp, with a consequent variation of the slope of the group delay curve. The thermal gradient has been realized applying arrays of heating elements along the gratings and driving them with external currents. It has been shown that this methods permits to tune the dispersion between

100 ps/nm and 600 ps/nm with a gradient amplitude 30 K. If the gradient amplitude is reversed, it is possible to reverse the sign of the grating dispersion.

For each configuration a power consumption of 4.74 W for the entire dispersion compensator has been measured. This value can be first reduced limiting the dispersion tuning range. For small dispersion deviations, smaller gradients are required and the average grating temperature can be lowered, with a smaller power consumption. Furthermore the thermal isolation could be improved, for example etching isotropically broader and deeper trenches limiting the heat leakage in the lateral direction. A thinner isolation oxide layer between the metallic heater and the silicon guiding layer would also permit to increase the heat transfer and hence reduce the required electrical power.

An increase of the group delay ripple applying thermal gradients has been measured, most probably due to the discretization of the gradient itself with a finite number of heating elements. An improved design of their shape and their number is required to reduce the group delay ripple, and hence broaden the applicability range.

The proposed device permits the compensation of the residual dispersion of one 100 GHz WDM channel between -500 and 600 ps/nm. This values can be increased implementing longer grating and are comparable to what achieved with FIR serial filters on silica or with AWGs. However the gratings offer a more compact solution and an easier control. A chirped grating is already intrinsically dispersive, without needing the tune of several phase shifters and couplers. Furthermore the dispersion tuning is performed simply applying linear gradients. The only drawback of the proposed solution is the single-channel operation.

The compensation of several channels would require the cascading of several dispersion compensators. This leads to a relative large required area and complexity. A solution is offered by the sampled gratings, where the grating index modulation is periodically sampled with a period P. This sampling produces a comb of reflection peaks in the grating spectrum, with spacing:

$$\Delta\lambda = \frac{\lambda_{Bragg}^2}{2nP}. \tag{5.1}$$

This concept has already been shown in semiconductor lasers and optical fibers [107, 108]. The implementation of uniform sampled gratings has been demonstrated also in silicon rib waveguides [109], showing that the simultaneous reflection of 20 channels with a spacing of 0.78 nm is possible. The extension of this principle with the combination with chirp and

apodization is strongly required to obtain a device for the multi-channel dispersion compensation.

Bibliography

[1] M. Marciniak, "100/1000 gbit/s ethernet and beyond," *J. Telecom. Inform. Technol.*, vol. 1, pp. 14–19, 2009.

[2] R.-J. Essiambre, G. Kramer, P. J. Winzer, and B. Foschini, G. J. Goebel, "Capacity limits of optical fiber networks," *J. Lightw. Technol.*, vol. 28, pp. 662–701, 2010.

[3] T. Liu and I. B. Djordjevic, "On the optimum signal constellation design for high-speed optical transport networks," *Opt. Express*, vol. 20, pp. 20 396–20 406, 2012.

[4] S. J. Savory, G. Gavioli, R. I. Killey, and P. Bayvel, "Electronic compensation of chromatic dispersion using a digital coherent receiver," *Opt. Express*, vol. 15, pp. 2120–2126, 2007.

[5] M. S. Ab-Rahman and M. Moghaddasi, "The role of electrical pulse shapes in electrical and optical chromatic dispersion compensation," *J. Computer Sci.*, vol. 7, pp. 1921–1927, 2011.

[6] S. J. Savory, "Digital signal processing for coherent systems," in *Optical Fiber Communication Conference (OFC)*, 2012, p. OTh3C.7.

[7] J. Baliga, R. Ayre, K. Hinton, W. Sorin, and R. Tucker, "Energy consumption in optical IP networks," *J. Lightw. Technol.*, vol. 27, pp. 2391–2403, 2009.

[8] R. S. Tucker, "Green optical communications – Part II: Energy limitations in networks," *IEEE J. Sel. Top. Quantum Electron.*, vol. 17, pp. 261–274, 2011.

[9] M. Lipson, "Guiding, modulating, and emitting light on silicon – challenges and opportunities," *J. Lightw. Technol.*, vol. 23, pp. 4222–4238, 2005.

[10] B. Jalali, M. Paniccia, and G. T. Reed, "Silicon photonics," *IEEE Microwave Mag.*, vol. 6, pp. 58–68, 2006.

[11] K. Bücher, J. Bruns, and H. G. Wagemann, "Absorption coefficient of silicon: An assessment and the simulation of temperature variation of measurements," *J. Appl. Phys.*, vol. 75, pp. 1127–1132, 1994.

[12] L. Zimmermann, K. Voigt, G. Winzer, D. Wolansky, S. Geisler, H. Richter, and B. Tillack, "Silicon photonics front-end integration in high-speed 0.25 μm SiGe BiCMOS," in *IEEE/LEOS Group IV Photonics Conf.*, 2008, pp. 374–376.

[13] N. Sherwood-Droz and M. Lipson, "Scalable 3D dense integration of photonics on bulk silicon," *Opt. Express*, vol. 19, pp. 17 758–17 765, 2011.

[14] F. Y. Gardes, D. J. Thomson, N. G. Emerson, and G. T. Reed, "40 Gb/s silicon photonics modulator for TE and TM polarisations," *Opt. Express*, vol. 19, pp. 11 804–11 814, 2011.

[15] C. Stamatiadis, L. Stampoulidis, K. Vyrsokinos, I. Lazarou, D. Kalavrouziotis, L. Zimmermann, K. Voigt, G. Preve, L. Moerl, J. Kreissl, and H. Avramopoulos, "A hybrid photonic integrated wavelength converter on a silicon-on-insulator substrate," in *Optical Fiber Communication Conference (OFC)*, 2012.

[16] B. Jalali, V. Raghunathan, D. Dimitropoulos, and O. Boyraz, "Raman-based silicon photonics," *IEEE J. Sel. Top. Quantum Electron.*, vol. 12, pp. 412–421, 2006.

[17] M. Krause, H. Renner, and E. Brinkmeyer, "Efficient raman lasing in tapered silicon waveguides," *Spectroscopy*, vol. 21, pp. 26–32, 2006.

[18] G. P. Agrawal, *Nonlinear Fiber Optics*, 4th ed. Academic Press, 2007.

[19] I. P. Kaminow and T. L. Koch, Eds., *Optical Fiber Telecommunications IIIA*. Academic Press, 1997.

[20] E. Desurvire, J. R. Simpson, and P. C. Becker, "High-gain erbium-doped traveling-wave fiber amplifier," *Opt. Lett.*, vol. 12, pp. 888–890, 1987.

[21] M. Tachibana, R. I. Laming, P. R. Morkel, and D. N. Payne, "Erbium-doped fiber amplifier with flattened gain spectrum," *IEEE Phot. Technol. Lett.*, vol. 3, pp. 118–120, 1991.

[22] M. Jinno, T. Sakamoto, J. Kani, S. Aisawa, K. Oda, M. Fukui, H. Ono, M. Yamada, and K. Oguchi, "1580-nm band, equally spaced 8x10 Gb/s WDM channel transmission over 360 km (3x120 km) of dispersion-shifted fiber avoiding FWM impairment," *IEEE Phot. Technol. Lett.*, vol. 10, pp. 454–456, 1998.

[23] Y. Namihira and T. Ajchareeyasoontorn, "Large effective area dispersion shifted fibers with depressed cladding for WDM transmission," in *APCC/OECC '99*, 1999, pp. 1577–1580.

[24] T. Otani, M. Hayashi, M. Daikoku, K. Ogaki, Y. Nagao, K. Nishijima, and M. Suzuki, "Investigation of system upgradability over installed fiber-optic cable using 40-Gb/s WDM signals toward multiterabit optical networks," *J. Lightw. Technol.*, vol. 21, pp. 947–952, 2003.

[25] A. J. Antos and D. K. Smith, "Design and characterization of dispersion compensating fiber basd on the lp_{01} mode," *J. Lightw. Technol.*, vol. 12, pp. 1739–1745, 1994.

[26] T. Yokokawa, T. Kato, T. Fujii, Y. Yamamoto, N. Honma, A. Kataoka, M. Onishi, E. Sasaoka, and K. Okamoto, "Dispersion compensating fiber with large negative dispersion around -300 ps/km/nm and its application to compact module for dispersion adjustment," in *Optical Fiber Communication Conference (OFC)*, 2003, pp. 717–718.

[27] G. Ghosh, M. Endo, and T. Iwasaki, "Temperature-dependent Sellmeier coefficients and chromatic dispersions for some optical fiber glasses," *J. Lightw. Technol.*, vol. 12, pp. 1338–1341, 1994.

[28] T. Kato, Y. Koyano, and M. Nishimura, "Temperature dependence of chromatic dispersion in various types of optical fiber," *Opt. Lett.*, vol. 25, pp. 1156–1158, 2000.

[29] M. J. Hamp, J. Wright, M. Hubbard, and B. Brimacombe, "Investigation into the temperature dependence of chromatic dispersion in optical fiber," *IEEE Phot. Technol. Lett.*, vol. 14, pp. 1524–1526, 2002.

[30] A. Walter and G. Schaefer, "Chromatic dispersion variations in ultra-long-haul transmission systems arising from seasonal soil temperature variations," in *Optical Fiber Communication Conference (OFC)*, 2002, p. WU4.

[31] P. Pecci, S. Lanne, Y. Frignac, J.-L. C. Antona, G. Charlet, and S. Bigo, "Tolerance to dispersion compensation parameters of six modulation formats in systems operating at 43 Gbit/s," *Electron. Lett.*, vol. 39, pp. 1844–1845, 2003.

[32] F. Ouellette, "Dispersion cancellation using linearly chirped Bragg grating filters in optical waveguides," *Opt. Lett.*, vol. 12, pp. 847–849, 1987.

[33] K. O. Hill, F. Bilodeau, B. Malo, S. Thériault, D. C. Johnson, J. Albert, and K. Takiguchi, "Chirped in-fiber Bragg gratings for compensation of optical-fiber dispersion," *Opt. Lett.*, vol. 19, pp. 1314–1316, 1994.

[34] F. Ouellette, J.-F. Cliche, and S. Gagnon, "All-fiber devices for chromatic dispersion compensation based on chirped distributed resonant coupling," *J. Lightw. Technol.*, vol. 12, pp. 1728–1738, 1994.

[35] W. H. Loh, R. I. Laming, X. Gu, M. N. Zervas, M. J. Cole, T. Widdowson, and A. D. Ellis, "10 cm chirped fibre Bragg grating for dispersion compensation at 10 Gbit/sover 400 km of non-dispersionshifted fibre," *Electron. Lett.*, vol. 31, pp. 2203–2204, 1995.

[36] Y. W. Song, D. Starodubov, Z. Pan, Y. Xie, A. E. Willner, and J. Feinberg, "Tunable WDM dispersion compensation with fixed bandwidth and fixed passband center wavelength using a uniform FBG," *IEEE Phot. Technol. Lett.*, vol. 14, pp. 1193–1195, 2002.

[37] J. Lauzon, S. Thibault, J. Martin, and F. Ouellette, "Implementation and characterization of fiber Bragg gratings linearly chirped by a temperature gradient," *Opt. Lett.*, vol. 19, pp. 2027–2029, 1994.

[38] P. I. Reyes, N. Litchinitser, M. Sumetsky, and P. S. Westbrook, "160-Gb/s tunable dispersion slope compensator using a chirped fiber Bragg grating and a quadratic heater," *IEEE Phot. Technol. Lett.*, vol. 17, pp. 831–833, 2005.

[39] M. Bohn, W. Rosenkranz, and P. M. Krummrich, "Adaptive distortion compensation with integrated optical finite impulse response filters in high bitrate optical communication systems," *IEEE J. Sel. Top. Quantum Electron.*, vol. 10, pp. 273–280, 2004.

[40] K. Takiguchi, K. Jinguji, K. Okamoto, and Y. Ohmori, "Variable group-delay dispersion equalizer using lattice-form programmable optical filter on planar lightwave circuit," *IEEE J. Sel. Top. Quantum Electron.*, vol. 2, pp. 270–276, 1996.

[41] F. Horst, R. Germann, U. Bapst, D. Wiesmann, B. J. Offrein, and G. L. Bona, "Compact tunable FIR dispersion compensator in SiON technology," *IEEE Phot. Technol. Lett.*, vol. 15, pp. 1570–1572, 2003.

[42] C. K. Madsen, G. Lenz, A. J. Bruce, M. A. Cappuzzo, L. T. Gomez, and R. E. Scotti, "Integrated all-pass filter for tunable dispersion and dispersion slope compensation," *IEEE Phot. Technol. Lett.*, vol. 11, pp. 1623–1625, 1999.

[43] D. Teufer, S. Pachnicke, and P. M. Krummrich, "Modellierung und Simulation optischer IIR-Filterstrukturen zur adaptiven Kompensation chromatischer Dispersion in ultrahochbitratigen optischen Übertragungssystemen," in *ITG-Fachtagung "Photonische Netze"*, 2009.

[44] M. Shirasaki, "Large angular dispersion by a virtually imaged phased array and its application as a wavelength demultiplexer," *Opt. Lett.*, vol. 21, pp. 366–368, 1996.

[45] ——, "Chromatic-dispersion compensator using virtually imaged phased array," *IEEE Phot. Technol. Lett.*, vol. 9, pp. 1598–1600, 1997.

[46] T. Sano, T. Iwashima, M. Katayama, T. Kanie, M. Harumoto, M. Shigeara, H. Suganuma, and M. Nishimura, "Novel multichannel tunable chromatic dispersion compensator based on MEMS and diffraction grating," *IEEE Phot. Technol. Lett.*, vol. 15, pp. 1109–1110, 2003.

[47] F. Kerbstadt and K. Petermann, "Analysis of adaptive dispersion compensators with double-AWG structures," *J. Lightw. Technol.*, vol. 23, pp. 1468–1477, 2005.

[48] C. R. Doerr, L. W. Stulz, S. Chandrasekhar, and R. Pafchek, "Colorless tunable dispersion compensator with 400-ps/nm ranfe integrated with a tunable noise filter," *IEEE Phot. Technol. Lett.*, vol. 15, pp. 1258–1260, 2003.

[49] C. R. Doerr, D. M. Marom, M. A. Cappuzzo, E. Y. Chen, A. Wong-Foy, L. T. Gomez, and S. Chandrasekhar, "40-Gb/scolorless tunable dispersion compensator with 1000-ps/nm tuning ranfge employing a planar lightwave circuit and a deformable mirror," in *Optical Fiber Communication Conference (OFC)*, 2005, p. PDP5.

[50] D. M. Marom, C. R. Doerr, M. A. Capuzzo, E. Y. Chen, A. Wong-Foy, L. T. Gomez, and S. Chandrasekhar, "Compact colorless tunable dispersion compensator with 1000-ps/nm tuning range for 40-Gb/s data rates," *J. Lightw. Technol.*, vol. 24, pp. 237–241, 2006.

[51] C. R. Doerr, S. Chandrasekhar, M. A. Cappuzzo, A. Wong-Foy, E. Y. Chen, and L. T. Gomez, "Four-stage Mach-Zehnder-type tunable optical dispersion compensator with single-knob control," *IEEE Phot. Technol. Lett.*, vol. 17, pp. 2637–2639, 2005.

[52] A. Rahim, S. Schwarz, J. Bruns, K. Voigt, D. I. Kroushkov, M. T. Arnous, C. G. Schäffer, and K. Petermann, "Finite impulse response filter using 4-port MMI couplers for residual dispersion compensation," *J. Lightw. Technol.*, vol. 30, pp. 990–996, 2012.

[53] F. Kerbstadt, "Transmissionsphasengitter zur adaptiven Dispersionskompensation in hochbitratigen optischen Übertragungssystemen," Ph.D. dissertation, Technische Universität Berlin, 2006.

[54] H. Stoll and A. Yariv, "Coupled-mode analysis of periodic dielectric waveguides," *Opt. Comm.*, vol. 8, pp. 5–8, 1973.

[55] A. Yariv, *Quantum electronics*, 2nd ed. John Wiley & Sons, 1975.

[56] A. Yariv and M. Nakamura, "Periodic structures for integrated optics," *IEEE J. Quantum Electron.*, vol. 13, pp. 233–253, 1977.

[57] T. E. Murphy, "Design, fabrication and measurement of integrated Bragg grating optical filters," Ph.D. dissertation, Massachussets Institute of Technology, 2001.

[58] ——, "Integrated optical grating-based matched filters for fiber-optic communications," Master's thesis, Massachussets Institute of Technology, 1996.

[59] M. J. Kahn, "Integrated optical filters using Bragg gratings and resonators," Ph.D. dissertation, Massachussets Institute of Technology, 2002.

[60] M. P. Bulk, A. P. Knights, P. E. Jessop, P. Waugh, R. Loiacono, G. Z. Mashanovich, G. T. Reed, and R. M. Gwilliam, "Optical filters utilizing ion implanted Bragg gratings in SOI waveguides," *Adv. Opt. Technol.*, p. 276165, 2008.

[61] S. Homampour, M. P. Bulk, P. E. Jessop, and A. P. Knights, "Thermal tuning of planar Bragg gratings in silicon-on-insulator rib waveguides," *Phys. Status Solidi C*, vol. 6, pp. S240–S243, 2009.

[62] D. J. Moss, V. G. Ta'eed, B. J. Eggleton, D. Freeman, S. Madden, M. Samoc, B. Luther-Davies, S. Janz, and D.-X. Xu, "Bragg gratings in silicon-on-insulator waveguides by focused ion-beam milling," *Appl. Phys. Lett.*, vol. 85, pp. 4860–4862, 2004.

[63] K. S. Yee, "Numerical solution of initial boundary value problems involving Maxwell's equations in isotropic media," *IEEE Trans. Antennas Propagat.*, vol. 14, pp. 302–307, 1966.

[64] R. Scarmozzino, A. Gopinath, R. Pregla, and S. Helfert, "Numerical techniques for modeling guided-wave photonic devices," *IEEE J. Sel. Top. Quantum Electron.*, vol. 6, pp. 150–162, 2000.

[65] J. B. Schneider. (2010) Understanding the finite-difference time-domain method. [Online]. Available: www.eecs.wsu.edu/~schneidj/ufdtd

[66] J. Goeckeritz and S. Blair, "One-dimensional photonic crystal rib waveguides," *J. Lightw. Technol.*, vol. 25, pp. 2435–2439, 2007.

[67] G. Sztefka and H. P. Nolting, "Bidirectional eigenmode propagation for large refractive index steps," *IEEE Phot. Technol. Lett.*, vol. 5, pp. 554–557, 1993.

[68] J. Čtyroký, "A simple bi-directional mode expansion propagation algorithm based on modes of a parallel-plate waveguide," *Opt. Quantum Electron.*, vol. 38, pp. 45–62, 2006.

[69] J. Čtyroký, I. Richter, and P. Kwiecien, "Critical comparison of three modal methods: bidirectional eigenmode expansion propagation method, aperiodic rigorous coupled mode analysis and harmonic expansion method," in *Proc. of SPIE*, vol. 7099, 2008, p. 70991K.

[70] J. Čtyroký, S. Helfert, R. Pregla, P. Bienstman, R. Baets, R. D. Ridder, R. Stoffer, G. Klaasse, J. Petráček, P. Lalanne, J.-P. Hugonin, and R. M. D. L. Rue, "Bragg waveguide gratings as a 1D photonic band gap structure: COST 268 modelling task," *Opt. Quantum Electron.*, vol. 34, pp. 455–470, 2002.

[71] H. Wenzel, R. Güther, A. M. Shams-Zadeh-Amiri, and P. Bienstman, "A comparative study of higher order Bragg gratings: Coupled-mode theory versus mode expansion modeling," *IEEE J. Quantum Electron.*, vol. 42, pp. 64–70, 2006.

[72] R. A. Soref, J. Schmidtchen, and K. Petermann, "Large single-mode rib waveguides in GeSi-Si and Si-on-SiO_2," *IEEE J. Quantum Electron.*, vol. 27, pp. 1971–1974, 1991.

[73] P. Heimala, T. Aalto, S. Yliniemi, J. Simonen, M. Kuittinen, J. Turunen, and M. Leppihalme, "Fabrication of Bragg grating structures in silicon," *Physica Scripta*, vol. T101, pp. 92–95, 2002.

[74] Z. Wu, S. Honda, J. Matsui, K. Utaka, T. Edura, M. Tokuda, K. Tsutsui, and Y. Wada, "Tunable wavelength-band switch using large coupling-coefficient Bragg grating on SOI rib waveguide," in *Photonics in Switching Conference (PS 2006)*, 2006.

[75] S. Honda, Z. Wu, J. Matsui, K. Utaka, T. Edura, M. Tokuda, K. Tsutsui, and Y. Wada, "Largely-tunable wideband Bragg gratings fabricated on SOI rib waveguides employed by deep-RIE," *Electron. Lett.*, vol. 43, pp. 630–631, 2007.

[76] M. H. Lim, T. E. Murphy, J. Ferrera, J. N. Damask, and H. I. Smith, "Fabrication techniques for grating-based optical devices," *J. Vac. Sci. Technol. B*, vol. 17, pp. 3208–3211, 1999.

[77] T. E. Murphy, J. T. Hastings, and H. I. Smith, "Fabrication and characterization of narrow-band Bragg-reflection filters in silicon-on-insulator ridge waveguides," *J. Lightw. Technol.*, vol. 19, pp. 1938–1942, 2001.

[78] M. Krause, "Finite-difference mode solver for curved waveguides with angled and curved dielectric interfaces," *J. Lightw. Technol.*, vol. 29, pp. 691–699, 2011.

[79] N. Sugimoto, T. Shintaku, A. Tate, H. Terui, M. Shimokozono, E. Kubota, M. Ishii, and Y. Inoue, "Waveguide polarization-independent optical circulator," *IEEE Phot. Technol. Lett.*, vol. 11, pp. 355–357, 1999.

[80] N. Hanashima, K. Hata, R. Mochida, T. Oikawa, T. Kineri, Y. Satoh, and S. Iwatsuka, "Hybrid optical circulator using garnet–quartz composite embedded in planar waveguides," *IEEE Phot. Technol. Lett.*, vol. 16, pp. 2269–2271, 2004.

[81] T. Zaman, X. Guo, and R. J. Ram, "Integrated optical circulator in InP," in *Conference on Lasers & Electro-Optics (CLEO)*, 2005, pp. 1321–1323.

[82] T. R. Zaman, X. Guo, and R. J. Ram, "Proposal for a polarization-independent integrated optical circulator," *IEEE Phot. Technol. Lett.*, vol. 18, pp. 1359–1361, 2006.

[83] K. Petermann and F. Kerbstadt, "Planar optical apparatus for setting the chromatic dispersion in an optical system." US Patent US 2005/0 089 274 A1, April 28, 2005.

[84] L. B. Soldano and E. C. M. Pennings, "Optical multi-mode interference devices based on self-imaging: Principles and applications," *J. Lightw. Technol.*, vol. 13, pp. 615–627, 1995.

[85] P. A. Besse, M. Bachmann, H. Melchior, L. B. Soldano, and M. K. Smit, "Optical bandwidth and fabrication tolerances of multimode interference couplers," *J. Lightw. Technol.*, vol. 12, pp. 1004–1009, 1994.

[86] L. Poladian, "Understanding profile-induced group-delay ripple in Bragg gratings," *Appl. Opt.*, vol. 39, pp. 1920–1923, 2000.

[87] Z. Tan, Y. Liu, T. Ning, and S. Jian, "The generation of group delay ripple in chirped fiber gratings," *Ch. Opt. Lett.*, vol. 2, pp. 18–20, 2004.

[88] K. Ennser, M. Ibsen, M. Durkin, M. N. Zervas, and R. I. Laming, "Influence of nonideal chirped fiber grating characteristics on dispersion cancellation," *IEEE Phot. Technol. Lett.*, vol. 10, pp. 1476–1478, 1998.

[89] S. Jamal and J. C. Cartledge, "Variation in the performance of multispan 10-Gb/s systems due to the group delay ripple of dispersion compensating fiber Bragg gratings," *J. Lightw. Technol.*, vol. 20, pp. 28–35, 2002.

[90] X. Liu, L. F. Mollenaue, and X. Wei, "Impact of group-delay ripple in transmission systems including phase-modulated formats," *IEEE Phot. Technol. Lett.*, vol. 16, pp. 305–307, 2004.

[91] R. Kashyap and M. Rocha, "On the group delay characteristics of chirped fibre Bragg gratings," *Opt. Comm.*, vol. 153, pp. 19–22, 1998.

[92] H. Kogelnik, "Filter response of nonuniform almost-periodic structures," *Bell Syst. Tech. J.*, vol. 55, pp. 109–126, 1976.

[93] P. S. Cross and H. Kogelnik, "Sidelobe suppression in corrugated-waveguides filters," *Opt. Lett.*, vol. 1, pp. 43–45, 1977.

[94] J. Albert, K. O. Hill, B. Malo, S. Theriault, F. Bilodeau, D. C. Johnson, and L. E. Erickson, "Apodisation of the spectral response of fibre Bragg gratings using a phase mask with variable diffraction efficiency," *Electron. Lett.*, vol. 31, pp. 222–223, 1995.

[95] B. Malo, S. Theriault, D. C. Johnson, F. Bilodeau, J. Albert, and K. O. Hill, "Apodised in-fibre Bragg grating reflectors photoimprinted using a phase mask," *Electron. Lett.*, vol. 31, pp. 223–225, 1995.

[96] D. Wiesmann, C. David, R. Germann, D. Erni, and G. L. Bona, "Apodized surface-corrugated gratings with varying duty cycles," *IEEE Phot. Technol. Lett.*, vol. 12, pp. 639–641, 2000.

[97] K. Ennser, M. N. Zervas, and R. I. Laming, "Optimization of apodized lineraly chirped fiber gratings for optical communications," *IEEE J. Quantum Electron.*, vol. 34, pp. 770–778, 1998.

[98] K. Voigt, L. Zimmermann, G. Winzer, M. Schnarrenberger, T. Mitze, J. Bruns, and K. Petermann, "Silicon-on-insulator (SOI) delay-line interferometer with low polarization-dependent wavelength shift," in *European Conference on Integrated Optics (ECIO)*, 2007, p. ThC2.

[99] K. Voigt, L. Zimmermann, G. Winzer, T. Mitze, J. Bruns, K. Petermann, B. Hüttl, and C. Schubert, "Performance of 40-Gb/s DPSK demodulator in SOI-technology," *IEEE Phot. Technol. Lett.*, vol. 20, pp. 614–616, 2008.

[100] K. Voigt, L. Zimmermann, G. Winzer, H. Tian, B. Tillack, and K. Petermann, "C-band optical 90° hybrids in silicon nanowaveguide technology," *IEEE Phot. Technol. Lett.*, vol. 23, pp. 1769–1771, 2011.

[101] B. Costa, D. Mazzoni, M. Puleo, and E. Vizzoni, "Phase shift technique for the measurement of chromatic dispersion in optical fibers using LED's," *IEEE J. Quantum Electron.*, vol. QE-18, pp. 1509–1515, 1982.

[102] R. Fortenberry, W. V. Sorin, and P. Hernday, "Improvement of group delay measurement accuracy using a two-frequency modulation phase-shift method," *IEEE Phot. Technol. Lett.*, vol. 15, pp. 736–738, 2003.

[103] J. G. Proakis, *Digital communications*, 4th ed. McGraw-Hill, 2001.

[104] Y. Okada and Y. Tokumaru, "Precise determination of lattice parameter and thermal expansion coefficient of silicon between 300 and 1500 K," *J. Appl. Phys.*, vol. 56, pp. 314–320, 1984.

[105] G. Cocorullo, F. G. Della Corte, and I. Rendina, "Temperature dependence of the thermo-optic coefficient in crystalline silicon between room temperature and 500 K at the wavelength of 1523 nm," *Appl. Phys. Lett.*, vol. 74, pp. 3338–3340, 1999.

[106] U. Fischer, "Entwicklung und Optimierung eines integriert-optischen Schaltmoduls in Silizium," Ph.D. dissertation, Technische Universität Berlin, 1995.

[107] V. Jayaraman, Z. Chuang, and L. A. Coldren, "Theory, design, and performance of extended tuning range semiconductor lasers with sampled gratings," *IEEE J. Quantum Electron.*, vol. 23, pp. 1824–1834, 1993.

[108] L. Lin, F. Zujie, C. Haiwen, and C. Gaoting, "Sampled FBG based optical interleaver," in *Conference on Lasers & Electro-Optics (CLEO)*, 2001, pp. I–404–405.

[109] I. Giuntoni, P. Balladares, R. Steingrüber, J. Bruns, and K. Petermann, "WDM multi-channel filter based on sampled gratings in silicon-on-insulator," in *Optical Fiber Communication Conference (OFC)*, 2011, p. OMH5.

List of Figures

1.1 (a) Refractive index and group index as function of the wavelength for fused silica. (b) Chromatic dispersion coefficients of a SMF-28 step fiber. 8
1.2 Scheme of a transmission link with a standard fiber with length L and a dispersion compensating fiber with length L_{DCF}. The dispersion profile is considered for two different temperatures T_1 and T_2. 9
1.3 Scheme of a chirped Bragg grating of length L, with a linearly varying period $\Lambda(z)$. 11
1.4 (a) Principle of a FIR lattice filter. (b) Implementation of the FIR lattice filter cascading symmetrical and asymmetrical Mach-Zehnder interferometers [39]. 12
1.5 (a) Principle of a IIR lattice filter. (b) Implementation of the IIR lattice filter cascading ring resonators with radius R and phase shifters ϕ_n along a bus with tunable couplers κ_n. (c) Implementation of the tunable coupler with a symmetrical MZI and a phase shifter ϕ_κ [42]. 14
1.6 Schematic structure of a dispersion compensating system based on VIPA. 16
1.7 Principle of a dispersion compensator based on two AWGs connected by a free propagation region (FPR) [47]. 17
1.8 General structure of a serial-parallel filter for dispersion compensation. 19
2.1 Scheme of Bragg grating produced with a periodic index modulation in the waveguide core of thickness t. The overall grating length is L_g. The refractive indices of the cladding, core and substrate are n_1, n_2 and n_3 respectively. 22
2.2 Spatial evolution of the mode amplitude of the forward and backward travelling modes in the grating. 26
2.3 Reflectivity spectra of a Bragg grating with variation of the parameter κL_g. Left column: variation of κ and grating length L_g = 10 cm. Right column: variation of L_g with coupling factor constant $\kappa = 0.05\ \text{cm}^{-1}$. 28
2.4 Scheme of a Yee-cell of dimension Δx, Δy and Δz. The H field is computed at points shifted one half grid spacing from the E field grid points. 30
2.5 Schematic drawing of a generic waveguide with several discontinuities at the positions $z^{(s)}$. 32
2.6 Scattering matrix of a generic two-port component. 33

2.7 Scheme of the simulation model for the computation of the scattering matrix of a grating period. 35
2.8 Scheme of the considered grating benchmark structure: corrugated Si_3N_4 waveguide of thickness t =500 nm on SiO_2 substrate with periodic trenches with period Λ = 430 nm and different etching depths d: (a) 125 nm, (b) 375 nm and (c) 625 nm. 36
2.9 Computed reflection (continuous red lines) and transmission (dashed blue lines) spectra for the benchmark grating structure for three different etching depths: (a) 125 nm, (b) 375 nm and (c) 625 nm. 38
2.10 Geometrical parameters of a silicon-on-insulator rib waveguide Bragg grating: L_g overall length, d grating depth, u grating trench, Λ grating period, w waveguide width, t rib height. 40
2.11 (a) Calculated reflectivity spectra of a SOI planar Bragg grating for different numbers of modes in the BEP expansion. (b) Calculated peak reflectivity as function of the number of modes of the expansion. 41
2.12 Examples of integrated waveguides. (a) Rib waveguides with a guiding layer of t = 4 μm, (b) rib waveguide with a guiding layer of 1.5 μm and (c) photonic wire with a guiding layer of 220 nm. 42
2.13 Mode profiles of the fundamental TE mode for (a) rib waveguides with a guiding layer of 4 μm, rib width 4 μm and rib height 2 μm, (b) rib waveguide with a guiding layer of 1.5 μm, rib width 1.6 μm and rib height 0.5 μm, (c) photonic wire with a guiding layer of 220 nm and width 400 nm. . . . 43
2.14 Coupling between the forward propagating fundamental mode and the higher order backward propagating modes for the three waveguide geometries. In each case the grating period is adapted to fulfill the Bragg condition for the fundamental mode at λ = 1550 nm. 45
2.15 (a) Peak reflectivity, (b) reflected wavelength in nm, (c) loss in dB and (d) bandwidth in nm of a Bragg grating with period Λ = 225 nm and length L_g = 800 μm as functions of the grating depth d and the duty cycle DC. 47
2.16 (a) Peak reflectivity, (b) loss in dB and (c) bandwidth in nm of a Bragg grating with period Λ = 225 nm and duty cycle DC = 0.3 as functions of the grating depth d and length L_g. 49

2.17 Schematic description of the fabrication steps with a double lithographic process. (a) Grating patterning on the plane substrate, (b) grating etching, (c) patterning of the waveguide rib and (d) rib etching. 50
2.18 Schematic representation of three different possible implementations of Bragg gratings on rib waveguides: (a) corrugation of the side slab, (b) corrugation on the top of the rib and (c) corrugation on both rib top and side slab. 51
2.19 SEM micrograph of a Bragg grating patterned with (a) EB lithography and (b) DUV lithography. 52
2.20 Scheme of the measurement setup used for the characterization of the fabricated Bragg gratings. 54
2.21 Measured reflectivity and transmissivity spectra for Bragg gratings patterned with (a) EB and (b) DUV lithography. TE polarization is considered. In the inset plot the reflection peak of the DUV patterned grating is shown. 55
2.22 Comparison between computed and experimentally measured (a) transmission and (b) reflection spectra. The experimental data refer to a grating patterned with DUV lithography, with a period of $\Lambda = 226$ nm, a grating depth of $d = 50$ nm, a duty cycle $DC = 0.5$ and an overall length of $L_g = 800$ μm. The parameters of the simulated gratings are $\Lambda = 225$ nm, $d = 50$ nm, $DC = 0.5$ and $L_g = 800$ μm. TE polarization is considered. All spectra are in linear scale. 56
2.23 Reflectivity and transmissivity spectra for the TE (red continuous line) and the TM (dashed blue line) polarization. A grating patterned with EB lithography is considered, comparable results were measured on the DUV patterned ones. 57
2.24 Dependence of the introduced loss and of the reflectivity peak on the grating length L_g. A grating patterned with DUV lithography is considered. TE polarization. 58
2.25 Measured transmission spectra of gratings with variation of (a) grating period and (b) waveguide width. A grating patterned with DUV lithography is considered. TE polarization. 58
2.26 Comparison between the experimental and simulated dependence of the effective index on the waveguide width. A rib heigth of t =1.5 μm and an etching depth h = 0.5 μm have been considered. 59
3.1 Connection of a fiber Bragg grating with an optical circulator for the extraction of the reflected signal. 62

3.2 Principle of an integrated optical circulator based on a non-reciprocal Mach-Zehnder interferometer [79]. 63
3.3 Principle of a MMI coupler. 64
3.4 Scheme of the integrated Drop-filter for dispersion compensation. 65
3.5 Implementation of the chirp: (a) linear variation of the period from Λ_0 to $\Lambda_0 + \Delta\Lambda$, (b) linear variation of the rib width from w_0 to $w_0 + \Delta w$. 67
3.6 (a) Calculated reflectivity spectra of tapered gratings for different values of Δw. (b) Reflection bandwidth of tapered gratings as function of the taper width Δw. 68
3.7 (a) Calculated group delay curves of tapered grating with for different values of the length L_g. The taper width is Δw = 140 nm. (b) Dispersion of the tapered gratings as function the grating length L_g. 69
3.8 Amplitude and phase of (a) $\mathcal{F}(\kappa_0(z))$, (b) $\mathcal{F}\left(g(z)\right)$ and (c) $\mathcal{F}(\kappa_0(z)) * \mathcal{F}\left(g(z)\right)$. The calculations have been performed with the assumption of a weak grating, with a length of 5 mm and a a period chirp coefficient of C_Λ 700 nm/mm. . . 72
3.9 Description of the chirped grating as a Fabry-Perot resonator with varying length. 72
3.10 (a) Group delay curves of Fabry-Perot resonators for three different cavity lengths: 1 mm, 5 mm and 10 mm. (b) Calculated dependence of the ripple period and amplitude on the resonator length. 74
3.11 (a) Period in frequency and (b) amplitude of the group delay ripple as function of the grating length L_g. 75
3.12 Considered apodization profiles. The overall grating length is kept L_g 5 mm. 77
3.13 (a) Reflection spectra and (b) group delay curves of chirped gratings with different apodization profiles. 78
3.14 Scheme of apodization of a tapered grating with variation of the width of the trenches. 79
3.15 Asymmetric Mach-Zehnder interferometer used for the characterization of the MMI couplers. 80
3.16 (a) Output signal spectrum at the two output ports of the MZI for the TE polarization. (b) Output signal spectrum at the output port Out_1 for both polarizations. 81

3.17 (a) Scheme of the considered coupled rib waveguides with width w = 1.6 μm and varying distance d. (b) Propagation constants of the symmetric (β_s) and antisymmetric (β_a) modes. 82
3.18 Measured transmission spectra at the three output ports of the integrated dispersion compensator. TE polarization is considered. 84
3.19 Transmission spectra and group delay profile of the output signal at port Out_3 for (a) TE and (b) TM polarizations. The grating parameters are: Λ = 226 nm, d = 50 nm, DC = 0.5, L_g = 1 cm and Δw = 150 nm. No apodization has been applied. 85
3.20 SEM micrograph of an apodized grating (a) in the front part and (b) in the central region. 86
3.21 (a) Transmission spectra and (b) group delay profile at Out_3 of dispersion compensators based on unapodized (red curves) and apodized gratings (blue curves). 86
3.22 Emulation setup used for the evaluation of the system performance of the integrated dispersion compensator. 87
3.23 Constellation diagram at the receiver for the (a) uncompensated case, (b) compensation with unapodized gratings and (c) compensation with apodized gratings. 87
3.24 (a) OSNR penalty for different data rates for both unapodized and apodized gratings. (b) Variation of the OSNR penalty for different residual dispersion values at a data rate of 20 Gbaud using a dispersion compensator based on apodized gratings. 88
4.1 Transmission spectra at Out_3 of the dispersion compensator for different values of temperature increase. The starting temperature is 305 K. 92
4.2 Effect of the temperature on the reflection spectrum and group delay curve of a chirped gratings. (a) Uniform temperature, (b) linear gradient along the grating length and (c) differential linear gradient centered on a mean value. 93
4.3 Computed reflection spectra and group delay profile of a chirped grating with (a) positive and (b) negative temperature gradients. A sine profile apodization has been considered. The grating parameters are: Λ_0 = 225 nm, $\Delta\Lambda$ = 0.146 nm (corresponding to Δw = 150 nm), d = 50 nm and L_g = 5 mm. 95
4.4 Computed dispersion values for different applied temperature profiles. 96

4.5 Simulated reflected spectra and group delay profiles of a chirped grating with an applied temperature gradient of ΔT = 10 K realized with N heaters. The red curve indicates the ideal case of a linear gradient for comparison. 97
4.6 (a) Considered geometry for the calculation of the required power. (b) Thermal equivalent circuit of the slab region close to the rib with a heater. (c) Equivalent thermal circuit for the analysis of the lateral heat diffusion [106]. 98
4.7 Scheme of an isolation trench at the side of the heater through the top silicon layer and the oxide barrier. 100
4.8 Calculated relation between the required electrical power to be applied and the temperature of the waveguide core for three geometrical configurations. 101
4.9 Sketch of a section of the heating array. The heaters exhibit a length of L_h = 1.2 mm, a width of w_h =3 μm and a distance from the rib of d_h = 4 μm. 102
4.10 Mounted chip with the PCB for electrical contacts. In the inset picture the wire bonds from the wires on the PCB to the contact pads of the heaters are shown. 103
4.11 Scheme of the electrical connections of the heater arrays across a grating pair. Since both gratings have to be heated symmetrically, the same voltage V_n is applied to each pair of resistances R_h connected in parallel. 104
4.12 Transmission spectra at port Out_2 for different applied voltages. (b) Relation between the temperature increase in the grating and the applied electrical power per heater. 104
4.13 Applied power to the different heaters along each grating pair to achieve the desired temperature profiles. 105
4.14 Measured transmission spectra and group delay curves at port Out_3 of the dispersion compensator for different positive temperature gradients. Apodized gratings have been considered. TE polarization. 106
4.15 Measured transmission spectra and group delay curves at port Out_3 of the dispersion compensator for different negative temperature gradients. Apodized gratings have been considered. TE polarization. 107
4.16 Measured dispersion values for the different gradient amplitudes. The points are fitted with a hyperbola. 109
4.17 Amplitude-Frequency product of the measured group delay ripple for different temperature gradient amplitudes. . . 110

4.18 Applied electrical power profile and corresponding measured group delay curve. (a) Squared root profile, (b) linear profile and (c) parabolic profile. The gradient amplitude is all three cases 5 K. 111

List of Publications

Journals & Letters

- I. Giuntoni, A. Gajda, M. Krause, R. Steingrüber, J. Bruns and K. Petermann, "Tunable Bragg reflectors on silicon-on-insulator rib waveguides," *Opt. Express*, vol. 17, pp. 18518–18524, 2009.

- I. Giuntoni, D. Stolarek, H. Richter, S. Marschmeyer, J. Bauer, A. Gajda, J. Bruns, B. Tillack, K. Petermann and L. Zimmermann, "Deep-UV technology for the fabrication of Bragg gratings on SOI rib waveguides," *IEEE Phot. Technol. Lett.*, Vol. 21 , pp. 1894–1896, 2009.

- I. Giuntoni, D. Stolarek, D. I. Kroushkov, J. Bruns, L. Zimmermann, B. Tillack and K. Petermann, "Continuously tunable delay line based on SOI tapered Bragg gratings," *Opt. Express*, Vol. 20, pp.11241–11246, 2011.

- I. Giuntoni, D. Stolarek, J. Bruns, L. Zimmermann, B. Tillack and K. Petermann, "Integrated dispersion compensator based on apodized SOI Bragg gratings, " *IEEE Phot. Technol. Lett.*, Vol. 25 , pp. 1313–1316, 2013.

Conferences & Workshops

- I. Giuntoni, M. Krause, J. Bruns and K. Petermann, "Integration of Bragg Gratings on silicon on insulator (SOI) rib waveguides," in *ePIXnet Spring School on Technology for Photonics Integration*, 2008.

- I. Giuntoni, M. Krause, H. Renner, J. Bruns, A. Gajda, E. Brinkmeyer and K. Petermann, "Numerical survey on Bragg reflectors in silicon-on-insulator waveguides", in *IEEE/LEOS Group IV Photonics Conf.*, 2008, p. ThP14.

- I. Giuntoni, "Bragg gratings on small SOI rib waveguides", in *1st International Workshop on Tunable and Active Silicon Photonics*, 2008, p. Mo9.

- J. Bauer, D. Stolarek, L. Zimmermann, I. Giuntoni, U. Haak, H. Richter, S. Marschmeyer, A. Gajda, J. Bruns, K. Petermann and B. Tillack, "Deep-UV KrF lithography for the fabrication of Bragg gratings on SOI rib waveguides," in *Proc. of SPIE*, vol. 7545, 2010, p. 75450L.

- I. Giuntoni, D. Stolarek, A. Gajda, G. Winzer, J. Bruns, B. Tillack, K. Petermann and L. Zimmermann, "Integrated drop-filter for dispersion compensation based on SOI rib waveguides," in *Optical Fiber Communication Conference (OFC)*, 2010, p. OThJ5.

- I. Giuntoni, D. Stolarek, A. Gajda, G. Winzer, J. Bruns, B. Tillack, K. Petermann and L. Zimmermann, "Chirped gratings on tapered SOI rib waveguides for dispersion compensation," in *Bragg Gratings, Photosensitivity, and Poling in Glass Waveguides (BGPP)*, 2010, p. BMB4.

- I. Giuntoni, P. Balladares, R. Steingrüber , J. Bruns and K. Petermann, "WDM multi-channel filter based on sampled gratings in silicon-on-insulator," in *Optical Fiber Communication Conference (OFC)*, 2011, p. OThV3.

- I. Giuntoni, A. Gajda, M. Krause, D. Stolarek, R. Steingrüber, J. Bruns, L. Zimmermann, B. Tillack, E. Brinkmeyer and K. Petermann, "Integrated Bragg gratings on SOI rib waveguides for dispersion compensation," in *IX. ITG-Workshop Fachgruppe 5.3.2 Photonische Komponenten und Mikrosysteme*, 2011.

- I. Giuntoni, D. Stolarek, A. Gajda, J. Bruns, B. Tillack, K. Petermann and L. Zimmermann, "Integrated dispersion compensator based on SOI tapered gratings ," in *European Conference on Optical Communications (ECOC)*, 2011,
p. Th.12.LeSaleve.4.

- I. Giuntoni, B. Arar, J. Bruns and K. Petermann, "Dispersion compensation with tapered Bragg gratings on SOI nano-rib waveguides," in *2nd International Workshop on Tunable and Active Silicon Photonics*, 2011, Paper Su2.

Chromatic dispersion constitutes a strong limitation for the high speed transmission on long distances in optical communication systems and a realization of devices to mitigate its effect is mandatory. Optical components for the dispersion compensation do not require any optical-to-electrical signal conversion and exhibit a lower power consumption compared to electronic solutions. Furthermore their integration with demodulators and detectors would permit to obtain compact and low cost receiver modules on a silicon chip.
Within this work the design and the fabrication of a dispersion compensating device based on Bragg gratings on si licon waveguides has been considered. It is shown that this approach allows a tunable dispersion compensation between -500 ps/nm and 600 ps/nm for one 100 GHz WDM channel with a moderate power consumption is possible.

Universitätsverlag der TU Berlin
ISBN 978-3-7983-2576-0 (print)
ISBN 978-3-7983-2577-7 (online)